University of Nottingham
UK | CHINA | MALAYSIA

Computational Design of Electrostatically Stable Endohedral Fullerene Superlattices

Abigail Miller

Student Number: 4341939

Thesis submitted to the University of Nottingham
for the degree of Doctor of Philosophy

Supervised by Prof. Elena Besley &
Prof. Anthony J. Stace

School of Chemistry
University of Nottingham

25th March 2022

Abstract

Fullerenes and their clusters exhibit a diverse range of interesting electronic, magnetic, structural and chemical properties. This work looks at using an analytical model to give a sound physiochemical description of multiply charged fullerene clusters. Using the model introduced by Lindgren *et al.* in 2018, based upon the solution proposed by Bichoutskaia *et al.* in 2010, with added considerations of the dispersion effects, we can better understand the mechanisms of fullerene aggregate behaviour in a less computationally expensive manner. We provide an insight into the aggregation and fragmentation processes occurring in experiment and reproduce the results for minimum stable cluster sizes that have been seen experimentally. Finally, we draw predictions on clusters with charges not yet modelled computationally.

Alongside fullerene clusters, the assembly of nanoparticles of two different materials into Binary Nanoparticle Superlattices (BNSL) has been proven to be a cheap and effective route to producing a wide variety of materials with properties desirable for use in novel applications. Experiments have shown that the presence of charge is integral to the formation of ordered arrays. However, analysis of the forces responsible have been limited to pairwise interactions. To control the structure and morphology of novel BNSL structures, an in depth understanding of the forces responsible for long-range order are required. Here, our many-body electrostatic solution has been applied to seven frequently observed superlattice structures and has shown that multipolar interactions contribute significantly to lattice energy and thus stability. Additionally, a combination of AB and AB_2 BNSL structures, which have not been observed experimentally, are modelled in order to investigate whether many-body electrostatic interactions are sufficient to stabilise such structures. Coulombic and multipolar contributions to the interaction energy are inves-

tigated as a function of component ratio, allowing a comparison between the value of the minimum electrostatic energy to that found at the maximum packing fraction in hard-sphere theory.

Ultimately, nanoparticle lattices and endohedral fullerenes have both been identified as potential building blocks for future electronic, magnetic and optical devices. Here it is proposed that it could be possible to combine those concepts and design stable nanoparticle lattices composed of binary collections of endohedral fullerenes. The inclusion of an atom, for example Ca or F, within a fullerene cage is known to be accompanied by a redistribution of surface charge, whereby the cage can acquire either a negative (Ca) or positive (F) charge. It is predicted that certain binary combinations could result in the formation of stable nanoparticle lattices with the familiar AB and AB_2 stoichiometries. Much of the stability is due to Coulomb interactions, however, charge-induced and van der Waals interactions, which always enhance stability, are found to extend the range of charge on a cage over which lattices are stable. An extension of the calculations to the fabrication of structures involving endohedral C_{84} is also discussed.

Acknowledgements

Without a doubt, my first thanks must go my supervisors Professor Elena Besley and Professor Anthony J. Stace. They had a lot of faith taking on a CompChem rookie and I would like to thank them for their genuine, continuing care as well as their guidance and support. A mini supervisor himself, I'd like to thank Dr Joshua Baptiste. The road to Abi understanding MATLAB was not short nor smooth but I was never met with anything but a friend, no matter what time of day or how stupid my question inevitably ended up being. Thank you Josh for your patience. Thank you to Steve Oatley, a natural teacher who genuinely taught me how to use a computer. I feel very lucky to have found CompChem at Nottingham and my extended thanks go to everybody past and present who I've met in A46, A47 or A48 over the last three and a half years. The friendly and supportive atmosphere from CompChem, and those adopted, is invaluable. Specifically, I'd like to thank my CompChem girls Alexe, Ellen, Grace and Izzy for their support with science as well as day-to-day life. It's great to be able to work with your best friends everyday. A special shout-out goes to Ben and Connor - go us for managing to live, work and socialise together without getting sick of each other somehow. A big thanks to my lab buddy Ross who made the hours flyby and took on more than his fair share of 'why is my computer not working' questions from the freshers in order to save my sanity. I feel very thankful to those in the Women in Chemistry Group for all their help in organising the conference with me, especially Kat for being my soundboard and a great friend. We managed to organise an amazing event two weeks before my thesis deadline and so a heartfelt thanks goes to Kat for all the work she took on to help me out. Final honorary mentions go to some of my favourite places over the years - Sue's and the JA. My time in Nottingham wouldn't have been the same without them.

List of Publications

1. **A. Miller**, M. Halstead, E. Besley and A.J. Stace, Designing stable binary endohedral fullerene lattices. Phys. Chem. Chem. Phys., 24:10044–10052, 2022. doi: 10.1039/D2CP00196A.

2. **A. Miller**, A.J. Stace and E. Besley, Computational Predictions of the Fragmentation Pathways for Multiply Charged Fullerene Clusters, **2022**, *in preparation.*

3. E. B Lindgren, **A. Miller**, E. Besley and A.J. Stace, The Significance of Induced Electrostatic Interactions for the Controlled Fabrication and Stability of Binary Nanoparticle Superlattices, **2022**, *in preparation.*

4. E. B Lindgren, **A. Miller**, H. Avis, A.J. Stace and E. Besley, The Stabilisation of Binary Nanoparticle Superlattices by Addition of Excess Charge, **2022**, *in preparation.*

Nomenclature

Abbreviations/Acronyms

TOF	Time of Flight
BNSL	Binary Nanoparticle Superlattice
FMM	Fast Multipole Method
PPR	Pacheco and Prates-Ramalho
vdW	van der Waal
FCC	Face Centred Cubic
BCC	Body Centred Cubic
eV	Electron Volts
KE	Kinetic Energy

Symbols

ϕ	Electrostatic Potential
U	Interaction Energy
γ	Size Ratio
q	Charge
k	Dielectric Constant
a	Radius
s	Surface-to-Surface Separation
h	Centre-to-Centre Separation
ε	Absolute Permittivity
ε_0	Vacuum Permittivity
σ	Total Surface Charge Density
σ_b	Surface Bound (Polarisation) Charge Density
σ_f	Surface Free Charge Density (Total)
Γ	Denomination of a Particle's Surface in the Many-Body Formalism
E	Electric Field
χe	Electric Susceptibility
p	Electric Dipole Moment
α	Polarisability
P	Polarisation

Contents

List of Tables

List of Figures

Chapter 1

Introduction

From huge flashes of lightning that illuminate the sky around them, to the crackling sound that takes you by surprise when you take off your jumper, and your TV screen which collects dust a little quicker than other items —these are all phenomena caused by electrostatics, one of the four fundamental forces in our, sometimes discretely, electromagnetic world. The other three are gravitational, weak and strong. The latter two are especially short-range due to being restricted to the nuclei of atoms and thus only become centre stage in the study of nuclear physics. The gravitational force is familiar to us all from a young age. We witness it constantly - from apples falling from trees onto heads, the governing of our planets, stars and galaxies and the fact we aren't floating around but instead bound to the ground. Although it may become blindingly obvious when we see lightning bolts emerge from the clouds, the extent of phenomena that we can thank electromagnetism for may not be known to the uninformed person right away.

1.1 The History of Electrostatics

The electromagnetic force is the physical interaction between electrically charged particles and is known to be significant even when only small quantities of charge are involved. Of all fundamental forces, the electromagnetic is the only one which is fully understood at present, being fully described by the branch of physics named electromagnetism[10]. The electromagnetic theory was gradually developed through the work of iconic scientists, including Coulomb, Ampère, Faraday and Ørsted. It was Maxwell, in the 19th century, that presented a unified form of the theory. Although nowadays many of us have a very unconsciously reliant relationship with electricity, unconsciously that is until there is a power cut, electric phenomena have been the cause of wonder for millennia. A classic example is the vast build-up of charge in clouds leading to thunder and lightning, which was interpreted by many as being caused by the weapons of angry gods such as Zeus's sending down his thunderbolt to punish the ancient Greeks.

It all started with amber. The word electricity comes from the Latin term *electrum*, which is derived from the Ancient Greek word for amber, *elecktron*. The first electrical experiments in 600 B.C were based on amber, where Thales of Miletus noticed that amber which had been rubbed with wool, attracted lighter objects. This is because amber gained electric charge by rubbing and this was the first documentation of the effects of static electricity[11, 12]. For a long time after this, the Greeks thought that this phenomenon was unique to amber but, as we now know, when one object is rubbed with another, they both become charged. In a normal state, all atoms in an object contain an equal number of electrons and protons but, when one object is rubbed with another, electrons from one object will move to the other causing it to have more electrons than protons and thus become negatively charged. Similarly, the object that donates electrons will now be positively charged. The interac-

tion between these electrically charged particles, alongside gravity, governs a broad number of the interactions of everyday life. Although electrostatically induced forces may seem weak - the electrostatic force between an electron and proton in a hydrogen atom is over 40 times stronger than the gravitational force between them.

Fast forward to 1600 AD and Englishman William Gilbert, the court physician to James VI, I and Elizabeth I, is looking into these electric phenomena. Although there is no evidence that he was able to describe electricity, he was able to prove that there are differences between electricity and magnetism[13]. Until this point, it was commonly thought that magnetism and electricity were variations of the same thing but Gilbert was the first to indicate that they were separate things. He stated, for example, that a magnet always behaved like a magnet and didn't require rubbing. Amber, however, didn't show any electric effect without rubbing.

After this began the Franklin era. Most notably, he conducted an experiment to prove that lightning was electrical. He decided to fly a kite during a thunderstorm in order to collect electrical charge in Leyden jars[14]. Franklin developed what he called a 'single fluid' model of electric charge which states that an object with an excess of fluid would have one charge, whereas a deficit would lead to the opposite charge. The other proposed model at the time involved two fluids, one positive and one negative. The debate eventually was settled to agree with Franklin just over a century later[15]. We can also thank Franklin for a range of electrical terms still in use today such as charge, conductor, battery, positively and negatively. Additionally, his model led to what we now know as the Law of Conservation of Charge where the net amount of electric charge produced in any process is zero. In other words, the understanding that we can move charges around but cannot create nor destroy them.

When we charge an object by rubbing we notice that the charge only lasts a while. But if it can't be destroyed, where does it go? Most of the charge will disappear off into thin air. Well, kind of. It will dissipate into water molecules in the air. The polarity of water means that it has a side that is more negative and another which is more positive and this positive end can temporarily grab electrons. This is why we tend to see more static electricity in the colder months as the air is drier and so electrons aren't picked up as frequently.

Scientists created sensitive devices for detecting "electrification", also known as electrostatic charge imbalance, in the late eighteenth century. The phenomena of contact electrification, often known as contact tension, was quickly discovered. When two objects were touched together, the objects sometimes became charged spontaneously. One object developed a net negative charge, whereas the other developed a positive charge of equal magnitude. Scientists sought to explain how electricity is generated in an electric battery, or the Voltaic pile as it was then known, based on the observation of contact electrification. This idea was subsequently superseded by the present electrochemistry theory, which states that electricity is generated by chemistry and the exchange of electrons between the atoms that make up the battery. The finding that corrosion, or chemical degradation of the battery, seemed unavoidable with its usage, and that the more electricity was pulled from the battery, the faster the corrosion progressed, led to the rejection of the idea of contact tension.

The Volta effect corresponds to a weak electric potential that is created by the interaction of various metals. Alessandro Volta was the first to discover this effect, which may be measured with a capacitance electroscope made up of several metals. The actual effect, however, is insufficient to account for the operation of electric batteries. Between the early 1800s and the 1830s, a number of high voltage dry piles were developed in an attempt to explain static electricity, specifically to support Volta's contact tension hypothesis. One example

is the Oxford Electric Bell. Physicists assumed static electricity was different from other types of electricity until 1832. It was then that Michael Faraday reported the findings of an experiment demonstrating that magnet-induced electricity, voltaic electricity produced by a battery, and static electricity were all the same. The history of static electricity has since fused with the study of electricity in general since Faraday's result.

The principles of electrostatics play a leading role in a vast number of technologies, namely batteries, fuel cells, thermocouples, electroplating, photocells and light-emitting diodes (LEDs). However, if not managed, electrostatic interactions can lead to an undesirable accumulation of charge, which can damage some electronic components during manufacture.

1.2 Basics of Electrostatic Theory and Polarisation of Matter

The study of electrostatics begins with Coulomb's law. It has now been 236 years since Coulomb published his famous law which states that the force exerted by a point charge on another is directly proportional to the product of their magnitudes and inversely proportional to the square of the distance separating them[10]:

$$|\mathbf{F}| = K\frac{|q_1 q_2|}{r^2}, \tag{1.1}$$

K is the constant of proportionality in Coulomb's law, known as Coulomb's constant and is equal to $1/(4\pi\varepsilon_0)$, where ε_0 is the electric permittivity of free space and $K \approx 8.987\ 551\ 792 \times 10^9$ N m^2 C^{-2}[10]. While this gives only the magnitude of the interaction, taking the sign of the product $q_1 q_2$ reveals whether the interaction is attractive ($q_1 q_2 < 0$) or repulsive ($q_1 q_2 > 0$). In

vector form, a system with 2 point charges ($i = 1, 2$) in a vacuum, each with their own charge q_i and position $\mathbf{r}_i$, experiences an electrostatic force $\mathbf{F}_1$ on point charge 1 equal to

$$\mathbf{F}_1 = \frac{q_1 q_2}{4\pi\varepsilon_0} \frac{\mathbf{r}_1 - \mathbf{r}_2}{|\mathbf{r}_1 - \mathbf{r}_2|^3} = \frac{q_1 q_2}{4\pi\varepsilon_0} \frac{\hat{\mathbf{r}}_{12}}{|\mathbf{r}_{12}|^2} \tag{1.2}$$

where $\mathbf{r}_{12} = \mathbf{r}_1 - \mathbf{r}_2$ and $\hat{\mathbf{r}}_{12} = \frac{\mathbf{r}_{12}}{|\mathbf{r}_{12}|}$, a unit vector from point charge 2 to point charge 1. The force between two charges acts along the vector between the two and, obeying Newton's third law of motion, is equal in magnitude and in opposite directions on each charge ($\mathbf{F}_2 = -\mathbf{F}_1$).

The Coulomb force $\mathbf{F}$ on any charged particle can also be seen as being equal to the product of the electric field $\mathbf{E}$ and the charge of the particle q, and is given as

$$\mathbf{F} = q\mathbf{E}. \tag{1.3}$$

The electric field $\mathbf{E}_i$ generated at an arbitrary position $\mathbf{r}_0$ by point charge q_i at position $\mathbf{r}_i$ is given by

$$\mathbf{E}_i(\mathbf{r}_0) = K \frac{q_i}{|\mathbf{r}_0 - \mathbf{r}_i|^2} \hat{\mathbf{r}}_{0i}. \tag{1.4}$$

Coulomb's law, however, cannot generally describe interactions involving a charged particle of finite-size such as a system with unbalanced negative and positive charges. This is because in the presence of an electric field generated by an external source, charges in a finite sized particle might be redistributed before they assume a static, equilibrium position. It is only when, and if, the static charge positioning is known that Coulomb's law can be effectively applied. The response of a material to an external electric field, $\mathbf{E}$, such as that created by a point charge(s) in a charged object, depends on the nature of the specific material. Most matter in nature can be classified as either a

conductor or a dielectric - each category with its own set of distinct properties. A material is considered an electrical conductor when there are charge carriers within the material that are free to move in one or more directions through the bulk of the material when exposed to an electric field. An example of this would be a metal. When placed in an electric field electrons, which are only loosely bound to the atoms, will move until the whole material is an equipotential with no value of **E** in its interior. Dielectrics have a much more dilute reaction to an electric field. Dielectrics have their charges bound to the atoms within the material, meaning that they are electrically insulating and poor conductors of electric charge. In a dielectric material, the charge is split into two types of charges, "free" and "bound". Free charge is the charge that is present in excess and can move into electrostatic equilibrium but remains immobile during interaction; the latter assumption is justified by the zero mobility of free charge carriers. This condition also implies an absence of free charge inside the particle, so that only charge on the surface needs to be considered. Bound charge, on the other hand, is due to the polarisation of atoms or the reorientation of polar molecules to create a series of dipoles aligned within a field, as shown in Figure 1.1.

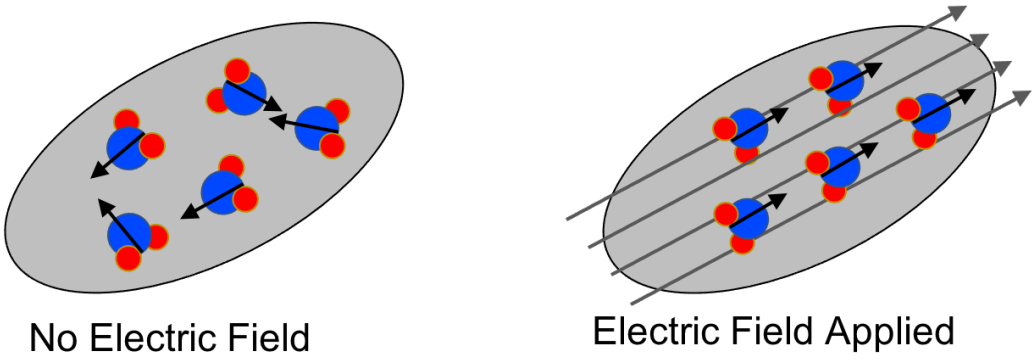

Figure 1.1: *An exaggerated visualisation of a particle composed of a polar molecule in the absence of an electric field (left) and exposed to an electric field (right).*

The polarisabilty, α, of an atom or molecule is the tendency of the charge density of the atom to be distorted from its natural shape due to influence

from an electric field, and is defined by the strength of the electric dipole moment, $\mathbf{p}$, induced by an external electric field, $\mathbf{E}$, as defined by:

$$\mathbf{p} = \alpha \mathbf{E} \tag{1.5}$$

In polar molecules there are additional contributions to polarisability including their intrinsic dipole from the arrangement and electronegativity differences in the constituent atoms. When a dielectric material is placed under the influence of an external electric field, each atom is polarised in this way. Every corresponding small induced dipole created across the bulk and extending to the material's surface accumulates so that the object in its entirety becomes polarised, resulting in the production of bound charges at the surface as shown in Figure 1.2.

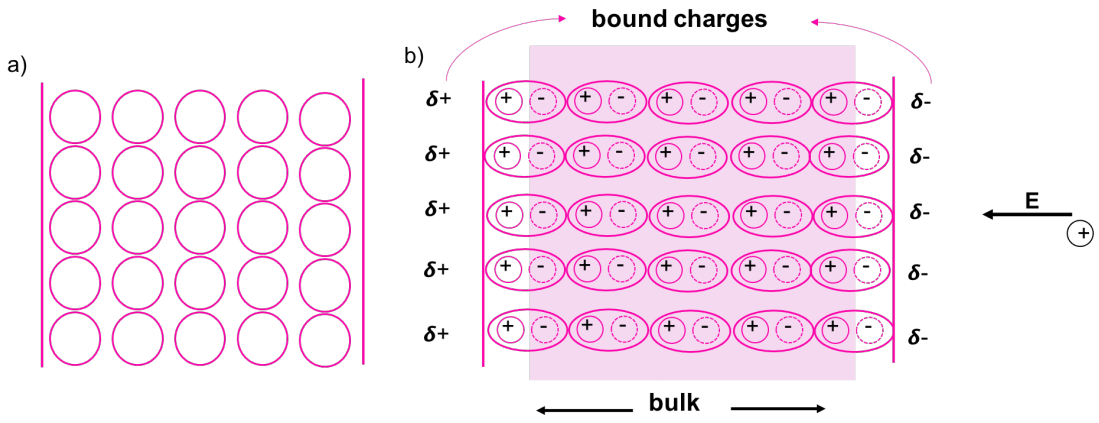

Figure 1.2: *a) Illustration of a neutral, unperturbed dielectric material. b) The same object, polarised by an external electric field* ***E****. Note that although in the bulk (shaded in a lighter colour) the charges of opposite sign due to adjacent dipoles cancel, this does not occur at the surfaces. This leads to the accumulation of bound charges.*

This effect can be described in terms of the polarisation, $\mathbf{P}$, defined as dipole moment per unit volume, related to a moderate applied field, $\mathbf{E}$, as defined as:

$$\mathbf{P} = \varepsilon_0 \chi_e \mathbf{E}, \tag{1.6}$$

where χ_e is the electric susceptibility which is a dimensionless constant of proportionality that implies the degree of polarisation in a material under the

influence of an electric field, **E**. The electric susceptibility is more commonly expressed in terms of the relative permittivity, also known as the dielectric constant, k, of the material as such:

$$k = \chi_e + 1, \tag{1.7}$$

where k is the ratio of the absolute permittivity of the material (ε) and the permittivity of free space (ε_0) as defined as:

$$k = \frac{\varepsilon}{\varepsilon_0}, \tag{1.8}$$

By substituting $k = 1$ in Equations 1.7 and 1.6, respectively, we can note that a material with a dielectric constant of 1 will not become polarised by an external electric field. If a non-polarisable material is neutral, and so has an equal number of negative and positive charges, it will be completely unresponsive to an applied electric field - an example of this would be air. This is because in a neutral non-polarisable material, no bound charges can be induced meaning that the electric field can pass through the material completely unperturbed. Many common materials with low dielectric constants are also non-polar, such as wood, oils and plastic and when placed in an electric field, we would see that these materials become weakly polarised. Water has a significantly higher dielectric constant, as well as some ceramics and some nitrogen-substituted compounds such as ammonia. Whilst under the influence of an electric field, the dipoles in the material are enhanced and align with the field, polarising the material. The material is then able to better counterbalance the magnitude of the field strength through the extent of the material itself.

The dielectric constant value is a bulk property. This means that when we use it out of this context, it loses its integrity. In the description of a small particle, it is more appropriate to use a parameter, as given by the Clausis-Mossotti relation in

$$\alpha = \left(\frac{k-1}{k+2}\right) 4\pi\varepsilon_0 a^3 \tag{1.9}$$

Equation 1.9[16]. This parameter, α, reflects the total polarisability of the particle by treating it as a sphere of dielectric constant k and radius a.

1.2.1 Method of Image Charges

A solution to the complex problem of how charged dielectric particles interact with each other has been the focus of discussion for many years. Early models created to describe the interaction between charged particles used relatively simple boundary conditions and were mainly aimed towards conducting spheres, stemming from the studies by Thomson (a.k.a Lord Kelvin)[17, 18]. It wasn't until 1964 when Davis published a bispherical coordinate system to derive an expression for the electrostatic force[19] that a complete solution for the the interaction between two conducting spheres was established. Such a model is still in use today in areas such as cloud physics, where it is highly effective due to the high polarisability of water. However, many situations such as dust particles in space, [20] suspensions of colloidal spheres,[21] the behaviour of volcanic ash[22] and charge scavenging in coal-fired power stations[23] all involve non-conducting particles and so cannot be modelled by Davis' model, highlighting the significant benefits to research that would be presented by finding a general, convergent solution to the problem of interacting dielectric particles.

A number of novel and more sophisticated approaches to computing the electrostatic interactions between charged particles, whether dielectric or conducting, have recently been published in the literature. Many of the proposed solu-

tions for the dielectric particle interaction problem, in particular, have relied on the early conducting sphere solution and utilised Lord Kelvin's image charge approach[17, 18]. The image charges technique is a mathematical methodology for solving differential equations that gets its name from the domain of the sought function (Φ) being extended by adding its mirror image across the interface[10]. The image theory states that a given charge configuration above an infinite grounded perfect conducting plane may be replaced by the charge configuration itself, its image, and an equipotential surface in the place of the conducting plane as seen in Figure 1.3.

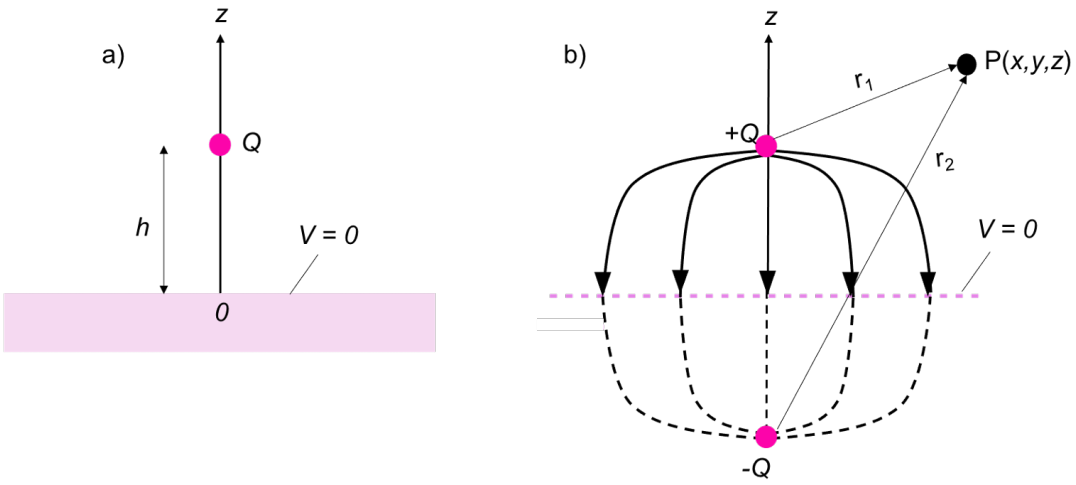

Figure 1.3: *a) Point charge and grounded conducting plane. b) Image configuration and field lines. Q is a point charge and the electric field at arbitrary point P can now be calculated using Coulomb's law.*

This results in the problem being solvable by Coulomb's law instead of having to solve Poission or Laplaces's equations. In applying the image method, two conditions must always be satisfied. The first is that the image charges must be located in the conducting region. Secondly, the image charges must be located such that the electric field on the surface of the conductor is zero or constant.

When the plane is dielectric rather than conducting, it can be treated nearly identically with minor changes. In this scenario, the charge of the image *q'*

formed by a point charge Q is no longer -Q, but is instead governed by the permittivity of both the plane k_1 and the medium that includes the point charge k_0, as given by the relationship:

$$q' = \frac{k_0 - k_1}{k_0 + k_1} Q. \tag{1.10}$$

We may determine that there are three possible interactions based on this relationship. An attractive interaction occurs when the plate is more polarisable than the medium ($k_1 > k_0$), resulting in an opposite-charge interaction. If the medium is more polarisable than the plate ($k_0 > k_1$), the image charge q' takes on the same sign as the source charge q, and the interaction with the plate is repulsive. When the medium's and plate's polarisabilities are equal ($k_0 = k_1$), q' becomes 0 and there is no interaction with the plate.

For basic systems with one polarisable boundary, the approach of image charges works exceedingly well, but when the complexity is increased to even two polarisable boundaries, an unlimited number of image charges are required to compute. This means that escalating the complexity to many-body interactions becomes progressively more computationally costly.

Chapter 2

Theory

2.1 Electrostatic Interactions between Two Charged Particles of Dielectric Materials

In 2010, Bichoutskaia *et al.*[24] introduced a general solution to the problem of two interacting spherical particles of arbitrary size, dielectric constant and electrical charge, covering a full range of separation distances including the point of contact. The particles are assumed to be electrically non-conducting, where the definition of electrical conductivity is defined as the product of carrier mobility and charge density[10]. This said, a non-conducting case carries the implication of the absence of free charge carriers in the system or if free charge is present that there is no mobility for the carriers.

The model is a general solution for calculating the electrostatic force between charged spheres composed from a dielectric material. The model in its simplest form, shown in Figure 2.1 presents the electrostatic interaction between a pair of suspended dielectric particles ($i = 1, 2$), with arbitrary net charge of q_i, radii a_i, dielectric constant k_i, in a surrounding dielectric medium with constant k_m. The spheres are separated by a surface-to-surface separation of s and a centre-to-centre separation of h.

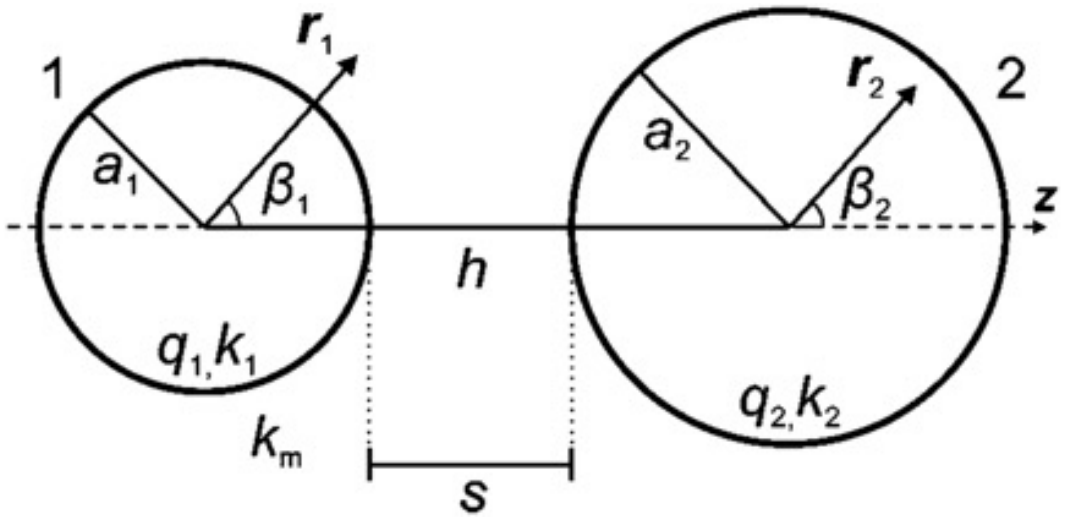

Figure 2.1: *A geometric description of two suspended, dissimilar dielectric spheres interacting in vacuum. Sphere 1 and sphere 2 each have their own radii (a), dielectric constants (k) and charges (q) and are separated by a surface-to-surface separation of s. r denotes the vector for a physical position relative to particles 1 and 2, β is the angle that vector r makes with the vector from 1 and 2, vector z.*

It is assumed that the free charge is uniformly distributed on the surface of a charged dielectric particle, which corresponds to the lowest-energy configuration, and remains immobile during interaction; the latter assumption is justified by the zero mobility of free charge carriers. This condition also implies an absence of free charge inside the particle, so that only charge on the surface needs to be considered:

$$\sigma_f = \frac{q}{4\pi a^2} \tag{2.1}$$

where there is no charge present in the volume of the sphere. The total surface charge density (σ) on a particle can then be written as a sum of the contributions from the bound charge density (σ_b) and the free surface charge density (σ_f) as such:

$$\sigma = \sigma_b + \sigma_f \tag{2.2}$$

where the bound surface charge density is a dynamic quantity that varies with the separation between the interacting particles.

In addition to the condition that the electric potential (Φ) vanishes at infinity, there are three additional boundary conditions applied in the model. The electric potential (Φ) created by the free charge residing on the surface of each particle satisfies the standard boundary conditions in electrostatics:

i. The continuity of the electric potential on the surface of each sphere due to the continuity of the tangential component of the electric field.

$$\hat{n} \times (\mathbf{E}_B - \mathbf{E}_A) = 0 \tag{2.3}$$

ii. The discontinuity of the normal component of the electric field due to the presence of the permanent charge on the surface of each sphere.

$$\hat{n} \cdot (\mathbf{E}_B - \mathbf{E}_A) = \frac{\sigma}{\varepsilon_0} \tag{2.4}$$

iii. The discontinuity of the normal component of the dielectric displacement field due to the presence of a free charge on the surface of each sphere.

$$\hat{n} \cdot (\mathbf{D}_B - \mathbf{D}_A) = \sigma_f \tag{2.5}$$

Where $\hat{n}$ is a unit vector perpendicular to a point of interest on the surface of each sphere, the subscripts 'A' and 'B' denote radial positions just below and above the sphere's surface, respectively, and ε_0 is the permittivity of free space. The electric displacement field $\mathbf{D}$ is by definition related to the electric field $\mathbf{E}$ as:

$$\mathbf{D} = k_i \varepsilon_0 \mathbf{E}. \tag{2.6}$$

The electrostatic force between two spheres $\mathbf{F}_{12}$ with the presence of surface charge on each is calculated from a generalisation of Equation (1.2) and is

given by

$$\mathbf{F}_{12} = K \int dq_1(\mathbf{r}_1) \int dq_2(\mathbf{r}_2) \frac{\hat{\mathbf{r}}_{12}}{|\mathbf{r}_1 - \mathbf{r}_2|^2}, \tag{2.7}$$

where $\mathbf{r}_1$ and $\mathbf{r}_2$ are position vectors at the surface of spheres 1 and 2 respectively, K is Coulomb's constant, and $\mathrm{d}q_1(\mathbf{r}_1)$ and $\mathrm{d}q_2(\mathbf{r}_2)$ are the corresponding charge elements. The first term $\int dq_1(\mathbf{r}_1)$ accounts for the charge on sphere 1, whereas the rest of the equation accounts for the electric field generated by the charge on sphere 2, similar to Equation (1.4). From this, the electrostatic force $\mathbf{F}_{12}$ is evaluated using a Legendre polynomial expansion of the electric potential (Φ) generated by each sphere as they interact. The total surface charge distribution is evaluated as a function of h. Integrating the charge over the surface leads to an analytical expression for the force in the form:

$$\mathbf{F}_{12} = -\frac{1}{K} \sum_{l=0}^{\infty} A_{1,l} A_{1,l+1} \frac{(k_1+1)(l+1)+1}{(k_1-1)a_1^{2l+3}}, \tag{2.8}$$

where a negative value for $\mathbf{F}_{12}$ indicates attraction, and repulsion for positive values. The multipole moment coefficients $A_{1,l}$ account for the dependence of $\mathbf{F}_{12}$ on h, and also describe the mutual polarisation of interacting spheres as a function of their charges (q_1/q_2), dielectric constants (k_1/k_2) and radii (a_1/a_2), with the equations describing $A_{1,l}$ deduced in Bichoutskaia *et al.*[24], and leading to the force being expressed as:

$$\begin{aligned} \mathbf{F}_{12} = K\frac{q_1 q_2}{h^2} - q_1 \sum_{m=1}^{\infty} \sum_{l=0}^{\infty} A_{1,l} \frac{(k_2-1)m(m+1)}{(k_2+1)m+1} \\ \times \frac{(l+m)!}{l!\,m!} \frac{a_2^{2m+1}}{h^{2m+l+3}} - \frac{1}{K} \sum_{l=1}^{\infty} A_{1,l} A_{1,l+1} \frac{(k_1+1)(l+1)+1}{(k_1-1)a_1^{2l+3}}. \end{aligned} \tag{2.9}$$

The first term in Equation (2.9) accounts for the monopole-monopole interaction, which is functionally equivalent to Coulomb's law with the interaction between point charges at the centre of each particle. The second and third terms account for the mutual polarisation of the charge densities of the particles, and

is always attractive in vacuum, with the magnitude of the interaction being a function of the dielectric constant, k. In the case of like-charged particles, particular combinations of q, a, and k can cause attractive polarisation interactions that overcome the repulsion of the coulombic interactions sufficiently enough that the overall force is attractive between like-charged particles.

2.2 Many-Body Electrostatic Interactions

A two-body electrostatic interaction can provide an adequate description of many underlying physical phenomena in the theoretical study of charged particles. The behaviour of volcanic ash[25], the stability of colloidal particles in dilute solutions[26] and parts of the cloud formation process[22] are just some of the systems accurately characterised by models that give electrostatic solutions for charged materials and can be applied to the interpretation of experimental findings. That being said, there are numerous cases that involve interactions between more than two charged particles and a description of two-body interactions is not sufficient for a quantitative description of the processes. Under these circumstances, a solution to model more complex systems where multiple particles are interacting would be required. Examples include but are not limited to: fullerene clusters[27], Coulombic crystals[28], concentrated colloidal systems[29], electrostatic self-assembly[30] and as of recently, superlattices[31].

Generally, a two-body interaction arises when the presence of electric energy in one of the particles creates an electric field, which induces a redistribution of surface charge and/or the polarisation of bound charge on a second particle that, in turn, generates its own electric field, thus prompting the same effect back on the first particle. This iterative process results in an equilibrium state where both of the particles acquire a static configuration that can either be attractive or repulsive. If a third particle is introduced into a two-body sys-

tem, the aforementioned iterative process is now taking place between all three particles, altering the equilibrium state of the system.

A number of solutions to calculate the electrostatic interactions in many-body systems can be found in the literature[32, 33], with most being dependent on image-charge methods. Describing the electrostatic interactions in many-body systems is an intrinsically more complicated problem, with an accurate description of problems by such methods becoming limited in regard to computational time. This is particularly the case when the system being considered requires a large number of corresponding "images" or multipole terms[34]. Additional complications to be considered for the many-body problem are that simplifications based on symmetry assumptions can no longer be allowed if three or more particles are involved, and the induction of bound charges due to polarisation effects in a particle, coupled with the same process in all particles, means that pairwise interactions can no longer be resolved independently.

In this work, a general solution based on an integral equation approach to the problem of calculating electrostatic interactions between many dielectric spherical particles by Lindgren *et al.*[34] is presented. The solution can provide an accurate, quantitative description of the physical characteristics of the electrostatic problem, with an important feature of being very computationally efficient. The theory has been published[34] and proven to produce an effective generalisation of Bichoutskaia's[24] two-body solution, showing agreement of numerical results for any calculated physical quantity and converging up to the point where the particles touch. Therefore, it can be utilised as a force field for particle dynamics simulations, as presented elsewhere[35].

The solution is able to treat a number, M, of particles with arbitrary size, charge, dielectric constant and position in three-dimensional space, embedded

in a homogeneous medium of an arbitrary dielectric constant.

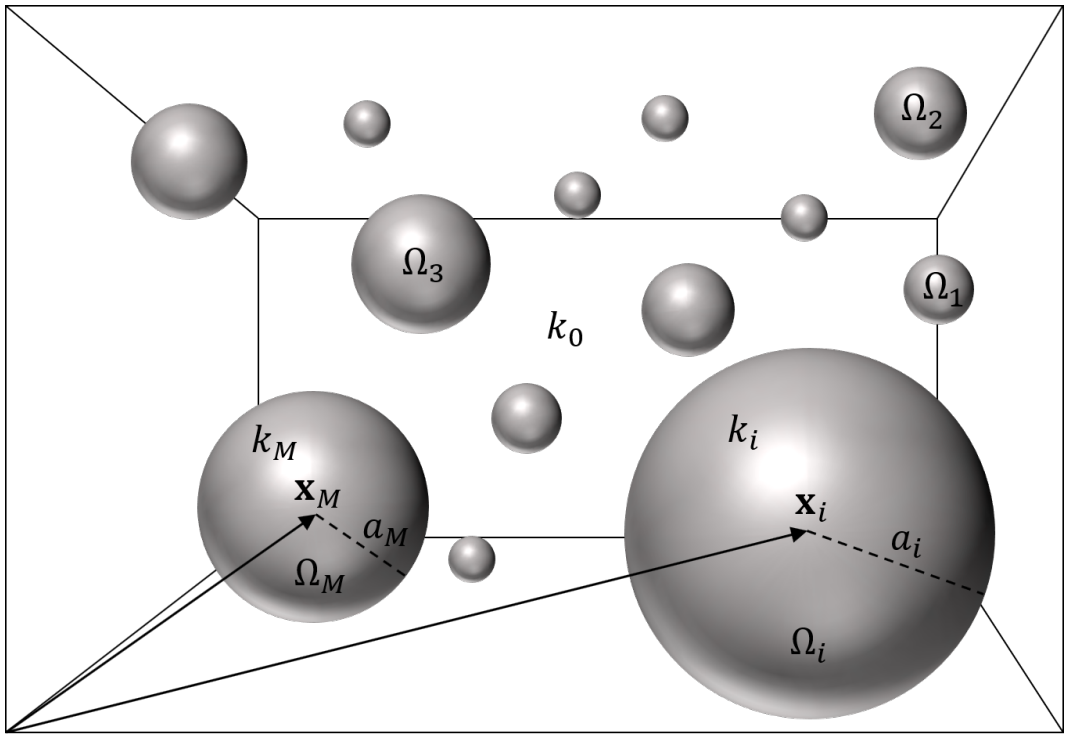

Figure 2.2: *Geometric representation of the system comprised of M non-overlapping spherical particles $\Omega_1, \ldots, \Omega_M$ with radius a_i, dielectric constant k_i, and centred at x_i, surrounded by a homogeneous medium of dielectric constant k_0.*

The considered system, illustrated in Figure 2.2, can be described in terms of the collection of M non-overlapping spherical particles $\Omega_1, \ldots, \Omega_M$ in a three-dimensional space, whereby each $\Omega_i (i = 1, 2, \ldots, M)$ has a radius, a_i, and position $r_i = (r_{i,x}, r_{i,y}, r_{i,z})$. The dielectric constant within each particle Ω_i is denoted by $k_i \geq 1$. For the purpose of this work, we will look at the system at a particular snapshot in time so that, in effect, the physical system is considered to be at rest. Particles are often described as hollow spheres ($\{\Omega_i\}_{i=1}^M$) with surfaces $\{\Gamma_i\}_{i=1}^M$. The surfaces of the dielectric particles represent the boundary Γ between the interior Ω^- and the exterior Ω^+ of the particles. Note that the global values for both the boundaries are defined as:

$$\begin{aligned} \Gamma_0 &= \Gamma_1 \cup \ldots \cup \Gamma_M, \\ \Omega_0 &= \Omega_1 \cup \ldots \cup \Omega_M. \end{aligned} \tag{2.10}$$

Each particle carries a free charge, q_i uniformly distributed over its surface and represented by a surface charge density $\sigma_{f,i} = q_i/(4\pi r_i^2)$ that is completely supported at its boundary, Γ_i such that a global function can be defined:

$$\sigma_f(\mathbf{x}) = \begin{cases} \sigma_{f,i} & \text{at all boundaries} \\ 0 & \text{otherwise.} \end{cases} \tag{2.11}$$

The electrostatic force due to the presence of a total charge on the surface of each particle is calculated from a generalisation of Coulomb's law for point charges and is given by:

$$\mathbf{F}_{12} = K \int dq_1(\mathbf{r}_1) \int dq_2(\mathbf{r}_2) \frac{\hat{\mathbf{r}}_{12}}{|\mathbf{r}_1 - \mathbf{r}_2|^2}, \tag{2.12}$$

where $\mathbf{r}_1$ and $\mathbf{r}_2$ are position vectors at the surface of spheres 1 and 2 respectively, K is Coulomb's constant, and $\mathrm{d}q_1(\mathbf{r}_1)$ and $\mathrm{d}q_2(\mathbf{r}_2)$ are the corresponding charge elements. If the electric potential (Φ) created by a free charge ($\sigma_{f,i}$), residing on each particle can be determined, then the electrostatic energy U follows directly from[10, 36].

$$U(\Phi, \sigma_f) = \frac{1}{2} \int_{\Gamma 0} \sigma_f(s)\Phi(s) ds. \tag{2.13}$$

where exclusively for this use, s denotes a point on the surface of a particle and not the surface-to-surface separation. Equation 2.13 gives the total electrostatic energy of the system, and the net electrostatic force on each particle, Ω_i, is obtained as the gradient of the energy with respect to changes in $\mathbf{x}$.

More information on the enhancement of the electrostatic solution and the formation of the many-body problem is included in Section A.1. Since the original publication of the two-body electrostatic solution, the theory has had

continuous development to the point where now there is a huge and versatile range of applications - some of which are highlighted in Table 2.1.

2.2.1 Fast Multipole Method

The model benefits from the implementation of a modified Fast Multipole Method (FMM), which renders an algorithm into linear complexity with respect to the number of particles in the calculation. FMM reduces the number of calculations needed for each particle by creating a grid where the electrostatic potential for particles within an individual cell in the grid is averaged to a single point. This means that any particle outside the cell only has to to interact with the single averaged point charge instead of every particle inside each grid. This drastically reduces the number of calculations required and makes the computation of large lattice structures more computationally efficient. If no FMM is used, the complexity of a general three-dimensional particle configuration scales with the fourth power of the degree of spherical harmonics utilised in the underlying expansions, and it scales with the third power with the more efficient FMM-embedding. Further details on the FMM implementation can be found in [34, 37].

Table 2.1: Applications of the electrostatic solution.

Application	**Description**	**Reference**
Highly Charged Fullerene Clusters	Computational predictions of the fragmentation pathways for multiply charged fullerene clusters using many-body theory and PPR dispersion considerations.	Miller *et al.*(in prep.)[5]
Binary Nanoparticle Superlattices	Modelling seven frequently experimentally observed superlattice structures. Calculations show us that the induced multipole interactions can contribute up to $\sim 90\%$ of the lattice energy.	Lindgren *et al.*[38]
Endohedral Fullerene Superlattice Stability	A series of studies looking at the many-body polarisation effects in endohedral fullerene superlattices. The first investigates the electrostatic interaction energy for varying particle charge combinations for a range of structures of AB-type to AB_2-type.	Miller *et al.* [31]
Excess Charge in BNSL Structures	In BNSLs, growth accompanied by an accumulation of non-compensated charge has always been considered as self-limiting and it will ultimately lead to instability, thus hindering the formation of extended lattices. This work shows how adding small amounts of excess charge can increase electrostatic stability in multiple lattice types.	Lindgren *et al.*(in prep.)
Polyoxometalate (POM) Adsorption	A study into the effect of the solvent on the interaction between a neutral POM and a charged plane. Solvents with high polarisability lead to repulsive polarisation interactions between charged and neutral species.	Lindgren *et al.*[39]
Aerosol Aggregation on Titan	The aggregation of negatively-charged particles in the atmosphere of Titan, one of Saturn's moons. The energy barriers for polar molecules are determined to be kT for asymmetric systems, and the aggregation of polar and non-polar materials is compared.	Lindgren *et al.*[40]
Cloud Microphysics	The coalescence of like-charged dust and ice particles in the upper mesosphere and lower thermosphere of the atmosphere has been studied.	Baptiste *et al.*[41]

2.3 The Addition of van der Waals Interactions

In an attempt to explain why real gases didn't obey the ideal gas law (PV = nRT, where P is pressure, V is volume, n is the number of moles, R is the gas constant and T is the temperature), physicist J.D. van der Waals investigated the effect of attractive interactions between molecules. At this time, 1873, he arrived at the famous equation of state for gases and liquids[16],

$$\Big(P + \frac{a}{V^2}\Big)\Big(V - b\Big) = RT, \tag{2.14}$$

in which he subtracted the term b from the volume in order to account for the finite size of the molecules. The addition of term $\frac{a}{V^2}$ to the pressure was to account for the attractive intermolecular force we now know as van der Waals. This simple equation gave a remarkably good account of the condensation of gases into liquids, with the values of a and b corresponding well to properties of molecules as we now understand them. By the beginning of the twentieth century it was acknowledged that intermolecular forces weren't of simple nature and in 1903 Mie[42] proposed an interaction pair potential of the form:

$$w(r) = -\frac{A}{r^n} + \frac{B}{r^m} \tag{2.15}$$

where A and B are parameters are related to the constants a and b in the van der Waals equation and r is the distance of separation between both particles (measured from the centre of one particle to the centre of the other particle). This was the first inclusion of a repulsive term as well as the attractive term. Although this approach has since been superseded, the forces of attraction and repulsion between molecules are still often named 'van der Waals' interactions.

The Lennard-Jones potential is a variation of Mie's work and was adopted by Lennard-Jones in the 1920s. It sets the n in Equation 2.15 to 12, m to 6 and

has values of $A = 4\varepsilon\sigma^{12}$ and $B = 4\varepsilon\sigma^{6}$. ε is the well depth and so is a measure of how strongly the two particles attract each other, σ is the distance at which the intermolecular potential surpasses zero and it gives a measurement of how close two non-bonding particles can get and is thus referred to as the van der Waals radius. It is equal to one-half of the internuclear distance between non-bonding particles. r_{eq} is the equilibrium distance of separation between both particles (measured from the centre of one particle to the centre of the other particle).

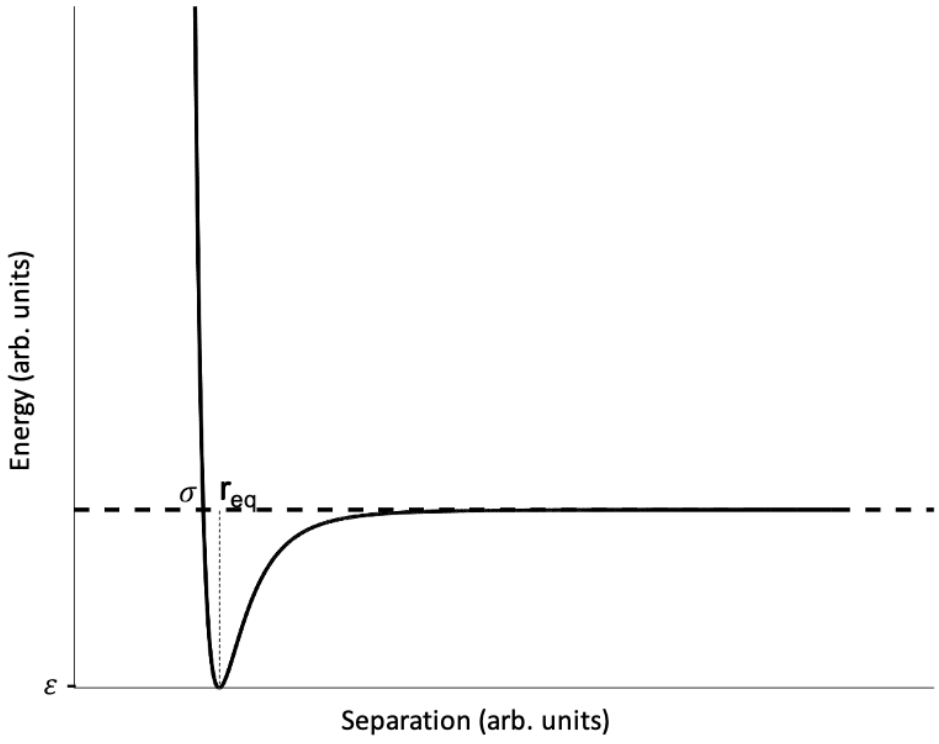

Figure 2.3: *A typical intermolecular potential energy function. ε is the well depth and so is a measure of how strongly the two particles attract each other, σ is the distance at which the intermolecular potential surpasses zero and r_{eq} is the equilibrium distance of separation between both particles.*

Figure 2.3 shows the interaction energy as a function of the distance between particles. The general features of the interaction potential remain as seen in Figure 2.3 but the precise form of the function is dependent on the chemical

species involved.

The van der Waals (vdW) forces involve momentary attraction between particles (atoms or molecules) and their origin lies at the atomic level. Although vdW forces are the weakest of all intermolecular attractions they are omnipresent, and, in instances where contribution from van der Waals forces is significant, the interaction can be very strong, playing a vital role in aggregation of molecules. If we consider the full picture of interaction between many-body systems, electrostatics alone is not enough.

2.3.1 Hamaker's Solution

The original form of vdW interactions implemented in the electrostatic solution was a variation of Hamaker's non-retarded van der Waals interactions which was developed to calculate the vdW interaction energy in vacuo between two bodies with simple geometries. It makes the assumptions that the interaction is additive as well as non-retarded. Equation 2.16 gives the interaction energy between spherical bodies of smooth surfaces of radii a_1 and a_2 and was first approximated by Hamaker[43] in 1937.

$$W(s) = -\frac{A}{6}\left(\frac{2a_1a_2}{(2a_1+2a_2+s)s} + \frac{2a_1a_2}{(2a_1+s)(2a_2+s)} + \ln\frac{(2a_1+2a_2+s)s}{(2a_1+s)(2a_2+s)}\right) \tag{2.16}$$

Equation 2.16 considers a vdW interaction between two clusters (radii a_1 and a_2) which are separated by a surface-to-surface separation of s. The total energy of all interacting pairs is calculated and integrated over the total volume of the object. A, the Hamaker constant is defined as:

$$A = \pi^2 \times C \times \rho_1 \times \rho_2 \tag{2.17}$$

ρ_1 and ρ_2 are number densities of the two interacting particles and C is the coefficient in the particle-particle interaction.

Hamaker's equation was added to the many-body code to give interaction energies which are a sum of the electrostatic and vdW interactions. In this work, the first system tested was that of the simple neutral fullerene dimer. The electrostatic interactions were calculated with the addition of Hamaker's form of the vdW interaction to produce an energy profile. As can be noted from Equation 2.16, there is an inversely proportional relationship between the vdW energy and the surface-to-surface separation, s. This means that as s tends towards zero and the particles get closer to touching, the vdW energy tends to negative infinity. This ultimately always leads to aggregation regardless of the system as the vdW contribution overpowers all other effects. At first, a limitation was added to Hamaker's vdW equation in order to cap the magnitude of the vdW interaction below an arbitrary minimum separation s_{min}. The issue arises here of accuracy. Although setting a limit solves the issue of infinite attraction at short separations, s_{min} is arbitrary.

The next step in reducing the magnitude of the vdW interactions at short separations was to dampen the energy using a modified dampening function presented by Mason *et al*[44]. The function shown in Equation 2.18 originated from studying empirical corrections in DFT-D methods. The dampening function inherent in this correction has been modified to also include a description of repulsion at small distances and has the form:

$$f_{damp} = 1 - e^{-\beta(\frac{a_1+a_2+s}{a_1+a_2})-1}, \tag{2.18}$$

where s is the surface-to-surface separation and β is a variable. Using this dampening function gives similar results (Figure 2.4) to the original form at

larger separations but provides a more realistic representation of dispersion at short separations due to the additional consideration of repulsion.

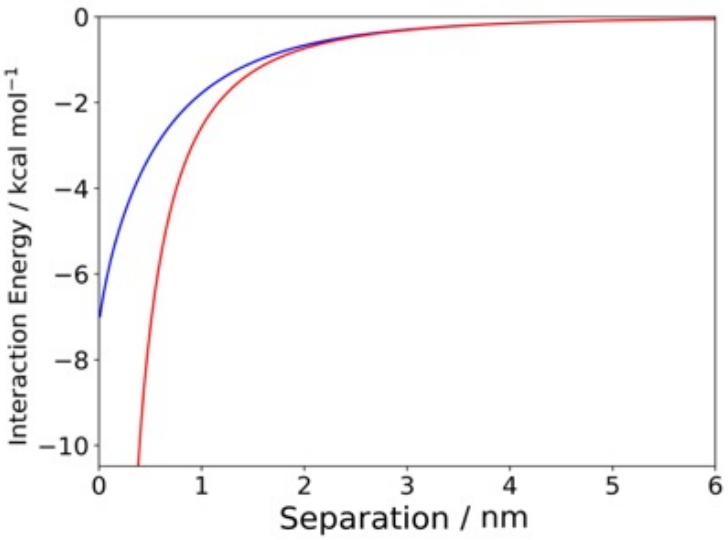

Figure 2.4: *The difference between Hamaker's non-retarded vdW interactions alone (red) and with the dampening function applied (blue) for a neutral fullerene C_{60} dimer.*

As can been seen from Figure 2.4, application of the dampening function means that when the surface-to-surface separation is zero the interaction energy becomes significantly smaller at $\sim$7 kcalmol^{-1}. In order to test the validity of continuing use of the dampened Hamaker, the results from Figure 2.4 were compared to those from multiple well-known computational techniques. The model was tested from intermolecular distances of 0 Å to 4 Å as it assumes the particles to be hard spheres. However, for the computational techniques referenced, data for overlapping atomic distances can be found[7]. With the addition of the dampening correction, and so the addition of a repulsive contribution at small distances, a much more suitable curve is seen in Figure 2.5. The dampened dispersion is seen to give results that fit amongst those of the techniques referenced at short separations and gives a much better fit that when Hamaker's equation is implemented.

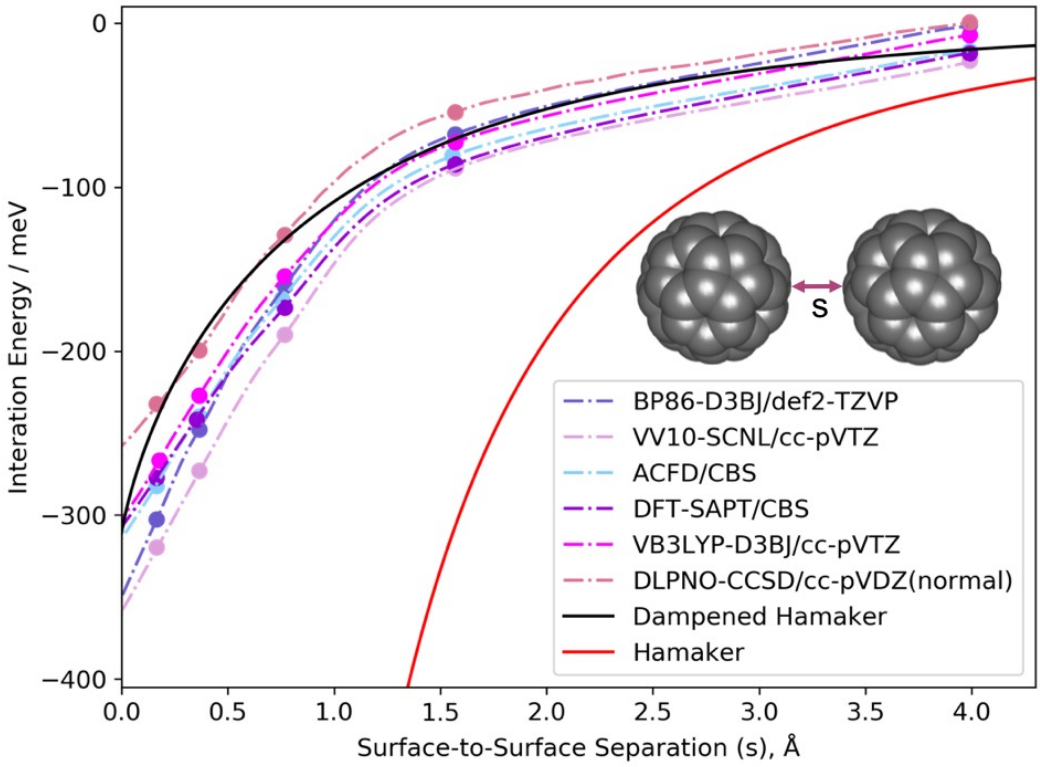

Figure 2.5: *The difference in interfullerene potential between Hamaker's non-retarded vdW interactions alone (red) and with the dampening function applied (blue) alongside different quantum approaches[7].*

The calculations in Figure 2.5 were also repeated at significantly larger (s = 100 nm) separation distances to ensure that the interaction plateaued to zero and there were no interaction at large separations, confirming the short-range nature of the interaction was still present.

Although created to calculate the vdW interaction energy in vacuo between two bodies with simple geometries, which is seemingly universal, there are many drawbacks of the Hamaker model that make it an unideal fit. As mentioned, it is based upon some assumptions, two of which assume additivity as well as the interaction being non-retarded. The neglect of the retardation effect is not such an issue in this work. The retardation effect becomes important when dealing with a liquid medium, so limits the breadth of theory this code is relevant for. Hamaker's equations are based on the assumption that summation of all interacting pairs can be replaced by integration. For this to

be valid, the separation between the two bodies must be large enough that all interacting materials can be treated as continuous media. Therefore, at separations less than a few molecular diameters the 'graininess of matter' can become an important factor. Additionally, pairwise additivity ignores the influence of neighbour molecules on the interaction between a pair of molecules which we know is present. Although this can be overcome, albeit through complicated calculations, there are many other versions of treating dispersion interactions which are more fitting. In addition, the dampening function introduced to limit the infinite value of dispersion, although presenting results comparable to other quantum-mechanic methods, was not designed to be used in the way it has been in this research.

2.3.2 Pacheco and Prates-Ramahlo's Approach

Before the work published by Pacheco and Prates-Ramahlo[5], most of the theoretical work carried out took the interfullerene interaction as that resulting from the superposition of carbon atom-atom classical interactions[5]. In spite of their success, these approaches have several drawbacks. Firstly, the interfullerene interaction is basically taken as a two-fullerene interaction only. Furthermore, each fullerene is usually treated as a superposition of non-interacting carbon atoms, disregarding their individual character and the high stability of the system. These are undesirable features which highlighted the need for a more sound theoretical scheme to determine the interfullerene interaction. An accurate calculation of the interaction specifically between C_{60} molecules was performed by Pacheco and Praters-Ramalho[5], which from hereon out shall be referred to as PPR. By application of first principles local-density approximation (LDA), the short-range part of the interaction potential is calculated. It is recognised that LDA cannot describe the long-range forces accurately and so the time-dependent-local-density-approximation (TDLDA) is used to evaluate the long-range part of the interaction potential. More detail on the princi-

Table 2.2: Coefficients implemented in the PPR potential for intermolecular interaction between two C_{60} cages.

C_6(eV Å^{-6})	C_8(eV Å^{-8})	C_{10}(eV Å^{-10})	C_{12}(eV Å^{-12})	C_{AT}(eV Å^{-9})
21 N_{at}^2	2534 N_{at}^2	2.09×10^8	7.78×10^{10}	21 N_{at}^3
M_0(eV)	τ	d_0(Å)	μ(Å)	σ(Å)
0.3	9.75	10.3	10.05	1.04

ples of both LDA and TDLDA and their applications to cluster science are described in a review by Calvayrac *et al.*[45]. The results of PPR were fitted analytically in the following manner. The interaction potential is comprised of two parts, a long-range and short range one.

The former is written as:

$$W(r) = \frac{C_6}{r^6} - \frac{C_8}{r^8} - \frac{C_{10}}{r^{10}} - \frac{C_{12}}{r^{12}}, \tag{2.19}$$

where the coefficients C_6, C_8, C_{10}, C_{12} are computed using the TDLDA and r is the distance between the particles. The values of the coefficients are listed in Table 2.2 where N_{AT} is the number of atoms in a single fullerene (60) and C_{AT} gives the magnitude of the Axilrod-Teller term.

The short-range part is written in the form of the Morse potential:

$$M(r) = M_0 exp\left[\tau\left(1 - \frac{r}{d_0}\right)\right]\left\{exp\left[\tau\left(1 - \frac{r}{d_0}\right)\right] - 2\right\} \tag{2.20}$$

where M_0, d_0 and τ are the Morse parameters (also in Table 2.2). The short and long-range parts of the potential can be combined using a switching function $F(r)$. The two body parts of the potential can be written as follows:

$$V_2(r) = F(r) \times M(r) + (1 - F(r)) \times W(r). \tag{2.21}$$

Function $F(r)$ is given by the expression:

$$F(r) = \frac{1}{1 + exp[(r - \mu)/\sigma]} \tag{2.22}$$

So $F(r) \longrightarrow 1$ for $r \longrightarrow \infty$ and $F(r) \longrightarrow 0$ for $r \longrightarrow 0$.

The PPR potential includes not only a two-body part of the potential. but a three-body consideration. This three-body term is called the Axilrod-Teller interaction and is written as:

$$V_3(r) = C_{AT} \left(\frac{1 + 3cos\gamma_i cos\gamma_j cos\gamma_k}{{r_{ij}}^3 {r_{jk}}^3 {r_{ki}}^3} \right), \tag{2.23}$$

where

r_{ij} is the distance between molecule i and j

γ_i is the angle between r_{ij} and r_{jk}

and C_{AT} gives the magnitude of the Axilrod-Teller term.

The contribution of the three-body force amounts to 6% of that of the two-body interaction at the maximum - sometimes enough to change the global minimum of structures of clusters[46].

Once the potential functions, two-body term V_2, and three-body term V_3, are given, the total potential energy of the system can be written as:

$$V_{tot} = \sum_{i,j} V_2(r_{ij}) + \sum_{i,j,k} V_3(r_{ij}, r_{jk}, r_{ki}) \tag{2.24}$$

The three-body term of the PPR potential considers the interaction between all possible combinations of three particles. When these three particles are close to one another there is significant vdW energy but when they are further

apart, there is minimal vdW contribution as can be seen in Figure 2.6.

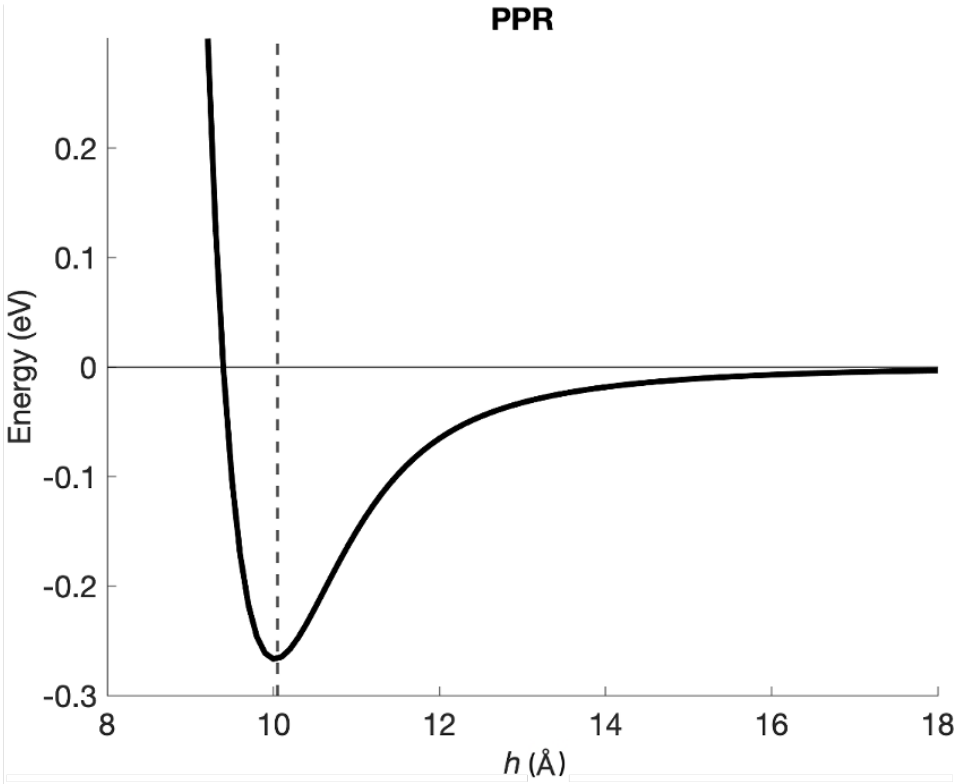

Figure 2.6: *Graph showing the PPR potential.*

Originally, the PPR implemented in the code was rather computationally expensive as they were testing all combinations of three particles in the system (systems now tested include over 4000 particles in this work). I have implemented a cut-off for consideration of the interaction such as in Figure 2.7. It is currently set to 25 Å, which is equivalent to 2.5 times the cage diameter and is shown in Figure 2.7b. This has very significantly improved calculation time and has made negligible difference to the energies calculated as seen in Figure 2.8b.

Figure 2.8a shows the validation of the PPR potential implemented in MATLAB. As PPR has been specifically developed as an interfullerene potential, we know it is the best fit for investigating C_{60}s in our model. In order to test the implementation of the PPR potential into the many-body solution, the vdW

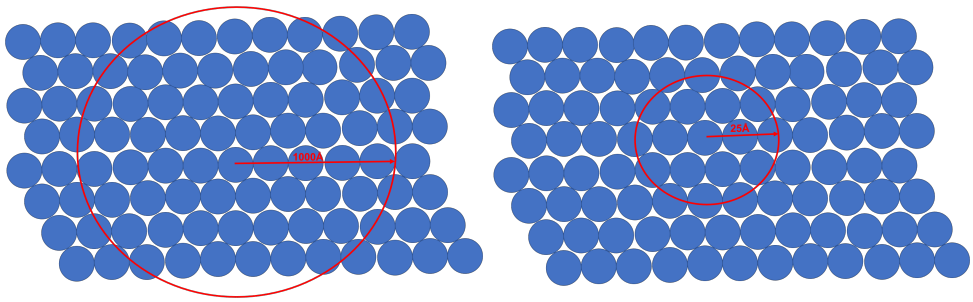

(a) **(b)**

Figure 2.7: *Figure (a) shows an example of a large distance cut-off distance for 3-body interactions. Figure (b) shows an example of the cut-off distance currently used in MATLAB of 25 Å.*

energy was calculated for fullerene clusters ranging from 3 to 150 fullerenes. This was then compared to the energies listed in the Cambridge Landscape Energy Database for the same cluster sizes using the PPR potential. As seen in Figure 2.8a the values for the vdW energy at each size are the same.

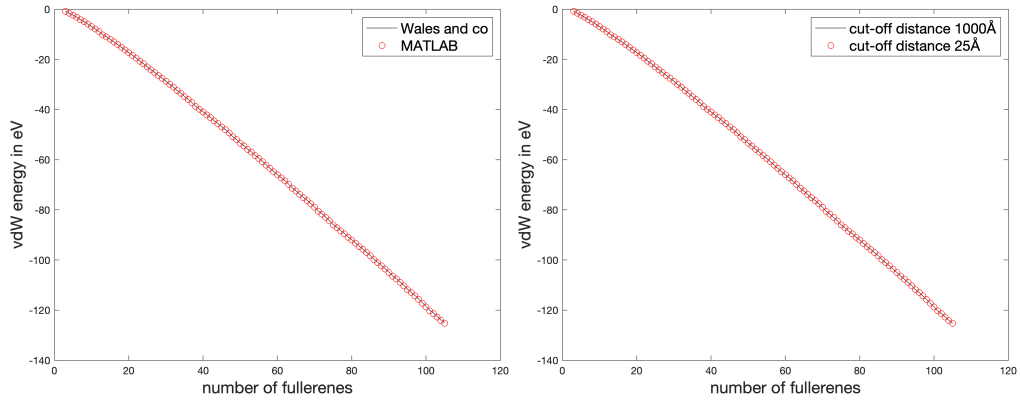

(a) **(b)**

Figure 2.8: *(a) The vdW energy for fullerene clusters of sizes 3-150 outputted from the PPR potential in MATLAB (red circles) using a three-body radial cut-off distance of 1000 Å and those values listed in the Cambridge Landscape Energy Database (black line). (b) The vdW energy for fullerene clusters of sizes 3-150 outputted from the PPR potential in MATLAB when the Axilrod Teller cut-off was set to 25 Å (red circles) and 1000Å (black line).*

Additionally, the difference in energy for setting the Axilrod Teller cut off to 1000 Å and 25 Å was investigated and illustrated in Figure 2.8b. It was found that there is a negligible difference between a large and current cut-offs for the Axilrod Teller term independent of structure size. Therefore the smaller

cut-off can be implemented to reduce computational cost without impacting accuracy.

2.3.3 Girifalco's Potential

An expression for determining an appropriate interaction potential between two C_x molecules was proposed by Girifalco[9]. The expression has been widely used, like PPR, due to its considerable accuracy and simplicity. However, unlike PPR, the Girifalco potential does not consider three-body interactions. It assumes that the fullerene-fullerene interaction is the sum of the pairwise interactions between the carbon atom of one fullerene molecule and that of the other molecule. For each carbon-carbon interaction, the Lennard-Jones potential is assumed and the interaction is averaged over the orientation of the molecules. The Girifalco potential has the following form:

$$V = -\alpha\left(\frac{1}{s(s-1)^3}+\frac{1}{s(s+1)^3}-\frac{2}{s^4}\right)+\beta\left(\frac{1}{s(s-1)^9}+\frac{1}{s(s+1)^9}-\frac{2}{s^{10}}\right) \quad (2.25)$$

where s=$\frac{r}{2a}$ is the distance between the centres of the fullerene molecules divided by the diameter of a single fullerene molecule so that the value of $2a$ is 7.1 Å for buckminsterfullerene[46]. Additionally:

$$\alpha = \frac{A(n^2)}{12(2a)^6} \quad (2.26)$$

and

$$\beta = \frac{B(n^2)}{90(2a)^{12}} \quad (2.27)$$

where n is the number of carbons in the fullerene and the parameters A and B were fitted to experimental data for the lattice constant and heat of sublimation.

An advantage of Girifalco over potentials such as PPR is that it has not only already been used in order to calculate several bulk properties of C_{60} and C_{70}[9, 47], but also for the determination of the liquid–vapor and liquid–solid coexistence lines of C_{60}, C_{70}, C_{76} and C_{84} (see Ref[48] and references therein).

We note that a spherical representation of fullerene particles has also been proposed by other authors[49–51] who, on the basis of simple topological considerations, assume an average molecular diameter proportional to the square root of the surface area of the molecule. Support for a spherical shape assumption also comes from experimental determinations of the gyration radii of C_{60}, C_{70} and C_{84}[52]. Work involved in this thesis considers the encapsulation of metals into C_{60} fullerenes. However, in order to maximise charge transfer in these systems, the encapsulation of molecules would be interesting to investigate. This would ultimately require fullerenes larger than that of C_{60} and so the Girifalco potential is also implemented into the electrostatic solution for some of the work seen later on in Chapter 5. The difference in the Girifalco intermolecular potential between C_{60}-C_{60}, C_{60}-C_{84} and C_{84}-C_{84} is plotted in Figure 2.9 and shows that due to the larger cage size, interactions between C_{84} cages happen at a larger value of h and also have a more significant interaction energy, implying that interactions between $C_{84}s$ are likely to be stronger than those between C_{60} cages.

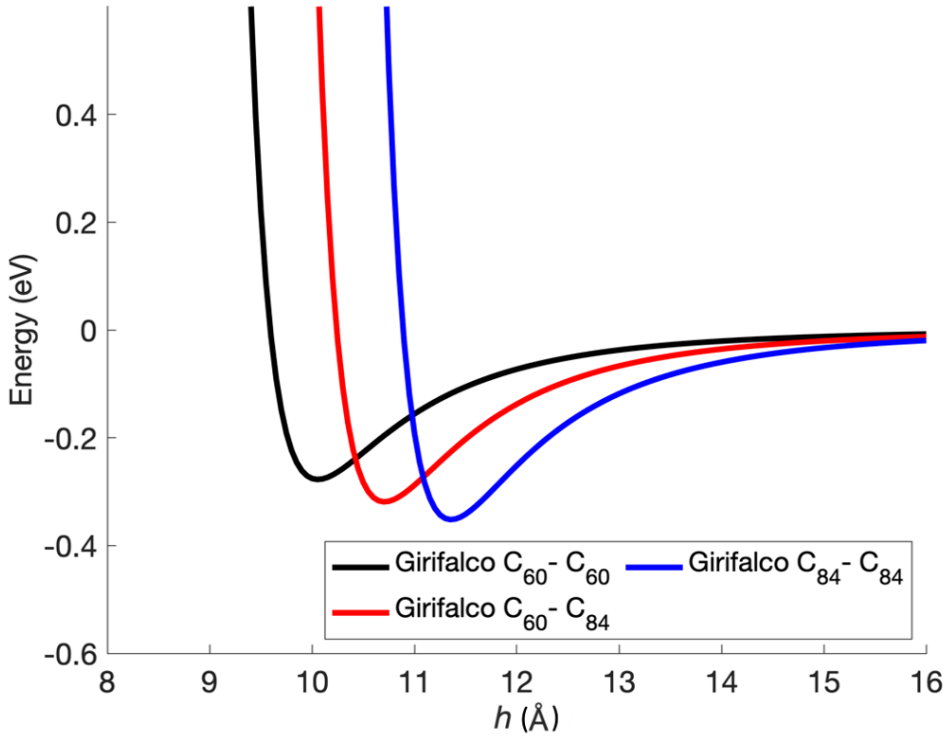

Figure 2.9: *The Girifalco intermolecular potential energy function for a C_{60}-C_{60} interaction, a C_{60}-C_{84} interaction and a C_{84}-C_{84} interaction.*

2.3.4 Theory Development

The many-body electrostatic theory described in Section 2.2 was coded into MATLAB by Lindgren prior to his publication in 2018[34]. The code included a van der Waal switch connected to Hamaker's equation for dispersion that had not yet been validated. As discussed in this work, Hamaker's equation is insufficient at accurately representing dispersion in large fullerene structures. To account for this, I added both the PPR and Girifalco equations to the electrostatic code. This meant that, depending on the system, one of these can be switched on in the many-body electrostatics code. The calculated van der Waal energy of the structure gets added to the Coulomb and polarisation energies to give a new total interaction energy. Additionally to this, I included a radial limit on the three-body Axilrod-Teller term to reduce the computational cost of these calculations.

Chapter 3

Investigating the Stability of Multiply Charged Fullerene Clusters

3.1 The Discovery of Buckminsterfullerene

Fullerene C_{60} was first discovered in 1985 by Kroto and colleagues[53] whilst they were attempting to study the formation mechanisms of long-chain carbon molecules in interstellar space. It is a nanostructured allotrope of carbon, along with graphite, diamond, amorphous carbon, nanotubes and graphene, and has significant interest in various science and engineering specialties. "Fullerene" is the umbrella term for closed-caged structures of carbon which form large spheroidal molecules consisting of a hollow cage and entirely pentagonal and hexagonal plane structures, as shown in Figure 3.1. Although carbon clusters of all sizes are referred to as fullerenes or "buckyballs", the specific type of fullerene referenced in this Chapter is the C_{60}, or football-like molecule with icosahedral symmetry.

A single fullerene has a closed-shell electronic structure and strong chemical bonds between the carbon atoms. Just like most atoms and molecules,

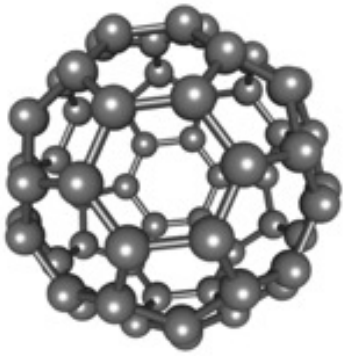

Figure 3.1: *Buckminsterfullerene, C_{60}.*

fullerenes can form clusters – referred to as "clusters of clusters"[46]. Fullerene aggregates are abundant in nature in many different forms and have many potential uses. For example, their interactions with graphene have been reported to have exciting potential uses in nanotechnology such as in hydrogen fuel cells[54]. Specifically, charged fullerene systems have been noted to have applications inclusive of biomedicine and molecular electronics[55] —provoking considerable interest in the properties of such clusters.

The first experimental research undertaken on clusters of fullerenes was in 1993 by Martin*et al.* [56], who produced clusters of fullerenes (both C_{60} and C_{70}) by using a low-pressure, low temperature helium gas atmosphere to prompt the condensation of fullerene vapour. This produced neutral clusters which were then subsequently ionised by an excimer laser before time-of-flight (TOF) mass spectrometry was used to produce a mass spectrum. The strong peaks seen in the photofragmentation mass spectra of singly ionised fullerene clusters were noted to be similar to those seen in rare-gas clusters, bearing significant resemblance to a charged $(Xe)_n$ spectrum and indicating the presence of structures based upon Mackay icosahedra up to size n = 55. However, computational simulations have not reached the same conclusion, with many predicting that past a certain size threshold (**n**) clusters should have a decahedral or close-packed structure, with the value of **n** varies from 13-16 depending on the computa-

tional model [57, 58]. It has been proposed by Rey *et al.*[59] that the transition seen from icosahedral to the decahedral or close-packing structures is the result of the short range interaction between single fullerenes, in comparison with its diameter. This is also the proposed mechanism acting behind some of the more peculiar behaviours of bulk C_{60}, such as the limited temperature range for the existence of the liquid phase[60].

In Martin's first experiment, it was not only singly charged, but also doubly and triply charged, clusters of fullerenes that were observed. For multiply charged clusters, the values of **n** were very similar to the singly charged cluster, giving the indication that the structure of the fullerene clusters is not reliant on charge[46]. However, this was then contradicted by the aforementioned computational investigations which present a theory proposing[56] the difference in experimental and theoretical results of the C_{60} structures can be attributed, in part, to the fact that experimental work inferred conclusions for only positively charged clusters whereas theoretical calculations have focused on neutral clusters. A seemingly plausible explanation, is due to the large polarisabilty of the C_{60} molecule, the addition of a long-range Coulomb term could influence the structure of the clusters —favouring icosahedral configurations.

This appeared a valid mechanism, but one which was disproven by Branz *et al.*[61] when they conducted experiments on both charged and neutral C_{60} clusters. Their investigation included heating the clusters to definite temperatures in a helium bath heating cell with subsequent characterisation by a TOF mass spectrometer and found a 35% increase in binding energy of the charged dimer compared to that of the neutral value. However, they also found that this increase had no impact on the structure of the clusters and concluded that the structure of ${C_{60}}^{(n+1)}$ clusters is insensitive to their charge state. The general proposed reason for the rapid disappearance of the icosahedral structures

therefore is charge independent and due to the short-ranged intermolecular potential. With decreasing range of the potential, structures with high internal strain, such as the icosahedra, are energetically less favourable as they involve nearest-neighbour distances that deviate from the ideal pair separation.

3.2 Are Fullerenes Dielectric or Metallic?

There has been much debate[27, 62, 63] in the scientific community as to whether or not fullerenes should be treated as dielectric or metallic in nature. It is important to know how to model such particles in a range of applications such as descriptions of cluster polarisabilities, charge transfer processes of fullerenes (and other spherical molecules) and force calculations between spheres with varying sizes and dielectric constants. The debate centres around whether or not it is possible to assign macroscopic properties to isolated C_{60} molecules and, if so, what is the permittivity value that best describes the electronic response of C_{60} due to external electric fields. There is also little known on whether this property would translate to a large cluster.

For our calculations, we suggest that fullerenes can be accurately represented as dielectric particles[27]. Icosahedral C_{60} from experiment has a very large HOMO-LUMO gap of 1.57 ± 0.03 eV[64]. As we cannot physically incorporate a fullerene into an electric circuit, there are other characteristics that need to be assessed to determine if it behaves as a dielectric or a conductor. The static and dynamic polarisabilities of C_{60} have been calculated using experimental data on the photoabsorption cross section[65]. It showed that C_{60} in a static electric field behaves not as a conducting sphere, but as a collection of individual carbon atoms and that its static polarisability way exceeds that expected of a conductive sphere[65]. These properties could be unique to C_{60} and may not apply to fullerenes in general. As an example, Fowler and Pisanski[66] indicate in their work that C_{20} represents the opposite extreme to that of C_{60}

as it has almost a zero HOMO-LUMO gap.

The value for the dielectric constant of a C_{60} fullerene cluster used in this work, 3.46, was taken from a publication by Nakamura *et al.*[4]. It was calculated using the Clausius-Mossotti formula:

$$\frac{k_i - 1}{k_i + 2} = \frac{4\pi}{3}\rho\alpha \tag{3.1}$$

Where $\rho = 1/\sigma^3$ and is the density of the fullerenes within the cluster and α is the static polarisability of an isolated fullerene taken as 76.5 Å^3, measured by means of a molecular beam deflection technique[67], giving a corresponding dielectric constant of 3.459. However, there have been varying accounts of the value, with the most striking coming from experiment at a larger value of 4.4[68].

In order to assess whether or not larger fullerene clusters maintain the dielectric nature of a single C_{60}, we investigate a basic linear chain. Modelling a dielectric five-body linear fullerene chain with two charges has numerous combinations of charge placements. As Table 3.1 shows, the system is most stable when charges are placed on the first and last fullerenes in the chain (*p1=1 and p2=5*). This is unsurprising as Coulomb's law shows that maximising the distance between charges will minimise repulsion.

Table 3.1: The interaction Energy, E_{int}, Coulombic energy (E_{Cou}), polarisation energy (E_{Pol}) and van der Waals energy (E_{vdW}) for a dielectric linear chain of C_{60} for varying charge placements. p1 and p2 are positions of the charges and $q_1 = q_2 = +1$

p_1	p_2	E_{Int} / eV	E_{Cou} / eV	E_{Pol} / eV	E_{vdW} / eV
1	2	-0.04	1.41	-0.20	-1.25
1	3	-0.67	0.71	-0.13	-1.25
1	4	-0.92	0.47	-0.15	-1.25
1	5	-0.99	0.35	-0.10	-1.25
2	3	-0.13	1.41	-0.29	-1.25
2	4	-0.74	0.71	-0.19	-1.25

In terms of polarisation energy, we see that the maximum separation at positions 1,5 gives the lowest interaction energy as the reduction in Coulomb repulsion is so great. When the charges are placed adjacent and centred, there is the highest polarisation contribution to stability which would be expected as when the charges are touching, negative surface charge will build up on one sphere and positive on the other, leading to an attractive force. This induces a build-up of charge where spheres touch one another, producing significant polarisation. As the distance between the charges is increased, the polarisation effect between them is decreased, hence the lowest polarisation energy is seen in the (1,5) configuration.

Now that the most stable charge placement for the chain has been confirmed, the fragmentation of the chain can be investigated in two ways as seen in Equations 3.2 and 3.3. Clusters, and in this case chains, have limited spatial extension with charges tending to move away from one another due to Coulomb repulsion; consequently there will come a point where the attractive binding energy is overcome. This phenomenon is called Coulomb fragmentation, or Coulomb decay, named after the driving force for the effect occurring. For a dielectric linear chain of five fullerenes with charges placed in positions with the maximum separation, there are two main pathways for fragmentation as can be seen in Figure 3.2.

$$(C_{60})_5^{2+} \rightarrow (C_{60})_4^{+} + (C_{60})^{+} \tag{3.2}$$

$$(C_{60})_5^{2+} \rightarrow (C_{60})_3^{+} + (C_{60})_2^{+} \tag{3.3}$$

Figure 3.3 is an energy profile of the fragmentation process of a linear fullerene chain via the two differing pathways shown in Figure 3.2. The interaction energy E_{int} is the energy of the system relative to that of the linear chain ($s = 0$).

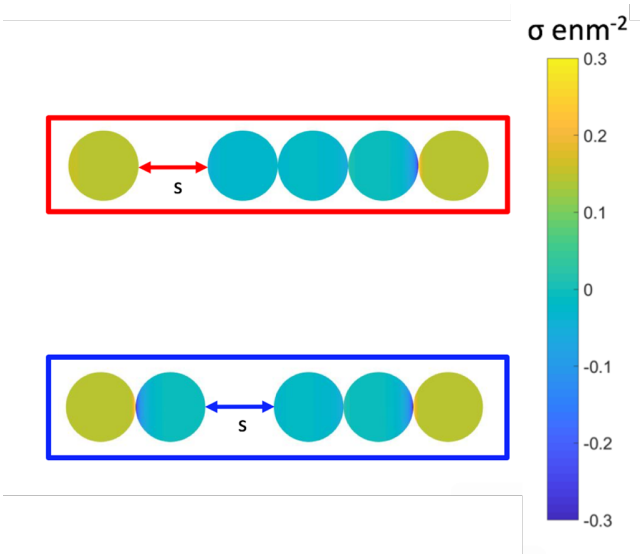

Figure 3.2: *Energy profiles for fragmentations in* $(C_{60})_5^{2+} \rightarrow (C_{60})_4^{+} + (C_{60})^{+}$ *[red] and* $(C_{60})_5^{2+} \rightarrow (C_{60})_3^{+} + (C_{60})_2^{+}$ *[blue].*

As the fragmentation begins to occur and the separation between the two fragments increases, energy barriers arise for the two processes. The energy barrier for the more symmetrical fragmentation (3.3), is seen to be noticeably smaller (~ 0.05 eV) than that shown by the emission in (3.2) making the more symmetrical fragmentation the more energetically favourable and most likely fragmentation pathway. In addition to this, the interaction energy of the fragments is significantly lower than that of the chain and lower than that of the fragments for fragmentation pathway 1, again confirming it to be the most likely mechanism and confirming the instability of the chain conformation. However, it cannot be stated that this is the only fragmentation occurring. Pathway 1 sees the fragments becoming more stable than the chain, only to a lower degree than that of pathway 2, indicating this fragmentation could also occur, just less likely or less often than the more symmetrical splitting of the chain.

In order to investigate the claims discussed above regarding the metallic behaviour of C_{60}[62, 63], then we would assume the charge is delocalised across the chain and does not reside on specific spheres like the results above. The

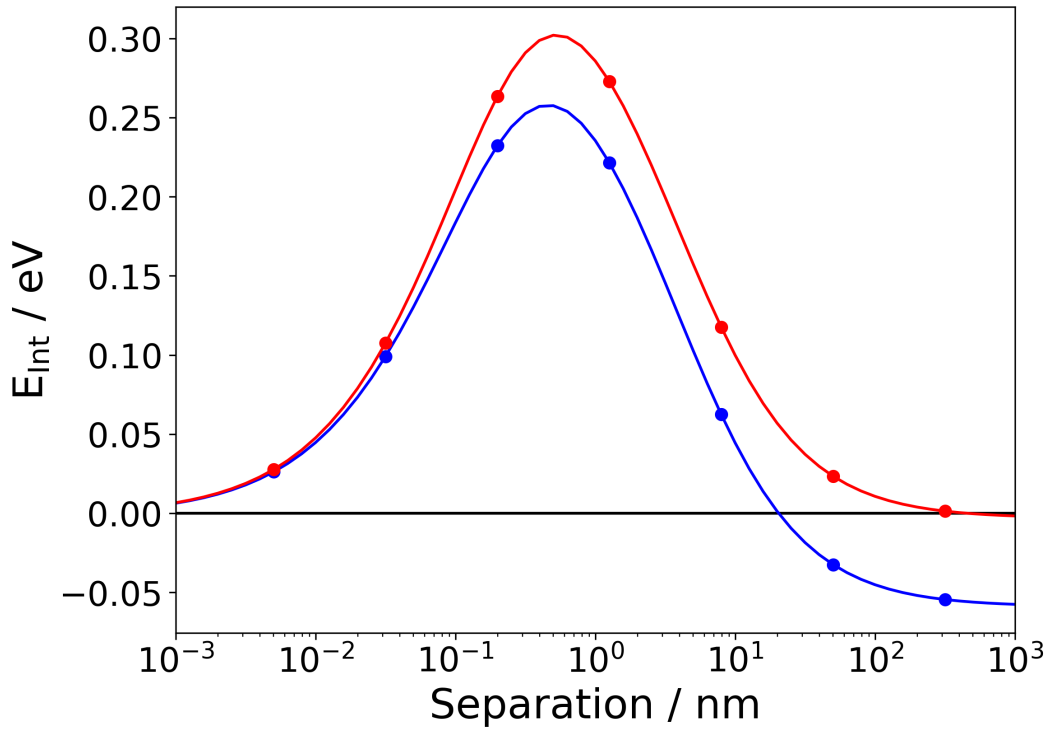

Figure 3.3: *Figure showing fragmentation of a dielectric linear chain by two different pathways as a function of the separation. Pathway 1:* $(C_{60})_4^+ + (C_{60})^+$ *[red]. Pathway 2:* $(C_{60})_5^{2+} \rightarrow (C_{60})_3^+ + (C_{60})_2^+$ *[blue]. The colour bar denotes the values of surface charge density present on the particles.*

model is based upon simulating spherical, dielectric particles but still has the capability to model a system as either metallic or dielectric by varying the value of the dielectric constant and the charge distribution. In this work, when referred to as being modelled in a 'metallic' nature it is implicit of conditions including uniform charge distribution over all spheres and a dielectric constant of 3000. Fragmentation of the chain was then modelled in the same way as in the dielectric, following pathways (3.2) and (3.3).

Much like its dielectric counterpart, the metallic model favours a more symmetrical fragmentation pathway with pathway 4 showing a smaller energy barrier as well as fragments which are lower in energy, when compared to pathway 3. However, unlike Figure 3.2, the main driving force for this difference is unlikely to be solely the polarisation energy. Although it can be noted that as separation increases, the asymmetric split sees an increase in polarisation energy

comparative to the symmetric split which has higher polarisation energy at smaller separations.

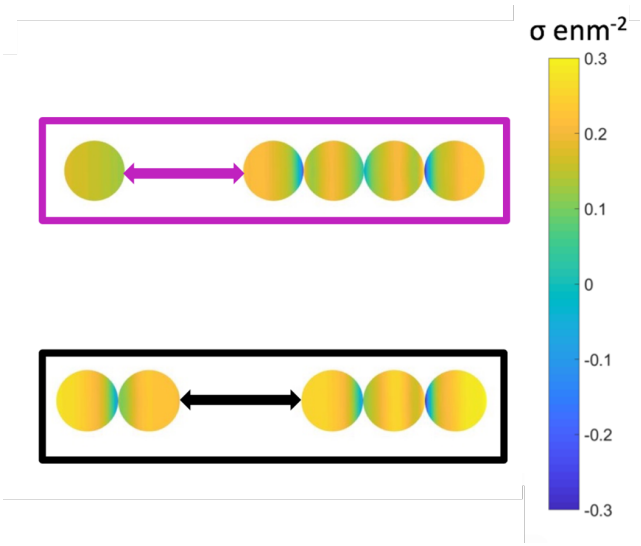

Figure 3.4: *Graphic showing fragmentation of a metallic linear chain by two different pathways. Pathway 3 (purple) shows fragmentation of a single fullerene. Pathway 4 shows a more symmetrical fragmentation (black).*

This can also be seen from the graphic in Figure 3.4, where pathway 4 results in polarisation occurring within both the fragments, unlike pathway 3 where polarisation is only in effect in the larger fragment.

The main contribution to the symmetric fragmentation in this case is the Coulomb repulsion. As can be seen from Figure 3.5, there is minimal variation in the plot for the different fragmentations at small separations from the attractive contributions of vdW and polarisation energies. However, as the separation increases between the fragments, the plots differ significantly as Coulomb forces dominate at long-range. In our metallic model, the charge is equally distributed across each fullerene meaning they are all positively charged. When they are in the chain with no separation distance, the repulsion is likely to be high between the charges. Either fragmentation pathway will see a reduction in this repulsion but it will be more apparent in pathway 4. For the dielectric, the reactions are thermodynamically allowed but kinetically

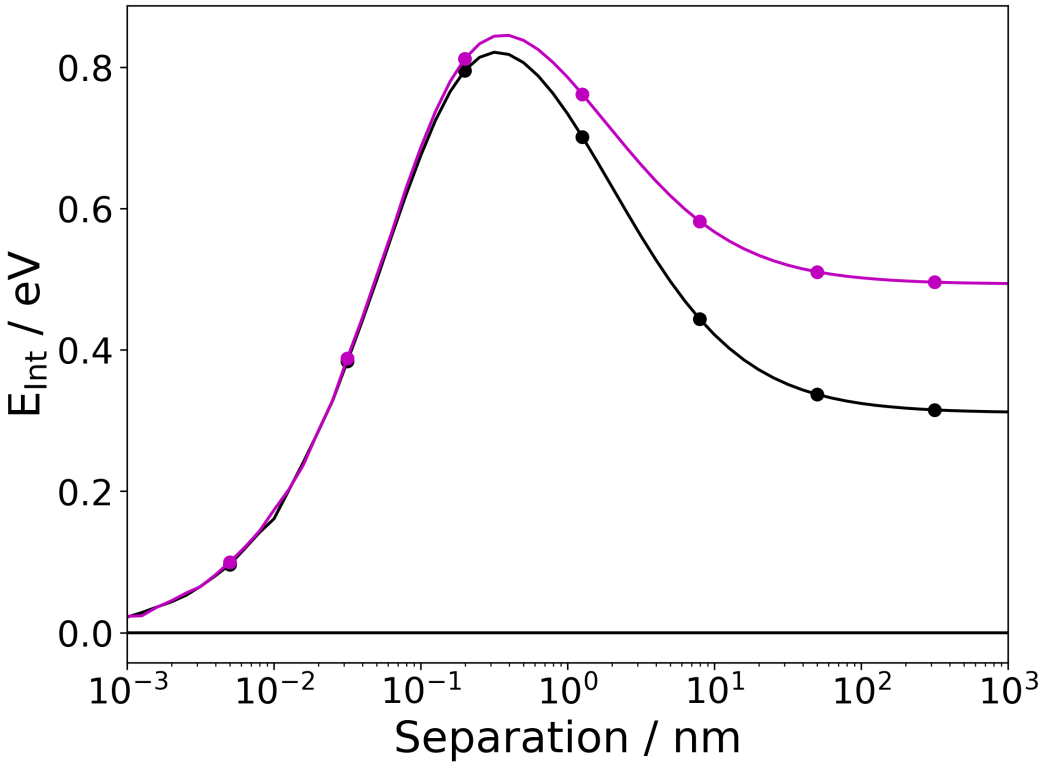

Figure 3.5: *Figure showing fragmentation of a metallic linear chain by two different pathways as a function of the log of the separation. Pathway 3 (purple) shows fragmentation of a single fullerene. Pathway 4 shows a more symmetrical fragmentation (black). The colour bar denotes the values of surface charge density present on the particles.*

unfavorable. However, for the metallic case the pathways are both thermodynamically and kinetically unfavorable. The energy barriers for the metallic configuration, 0.8210 eV (3) and 0.8449 eV (4), are significantly larger than those for the dielectric case, 0.2575 eV (1) and 0.3020 eV (2).

The value for the dielectric constant of 3.46, found by using an experimental static polarisabilty value in the Clausis-Mossotti equation, indicates that fullerenes would act as poor conductors. As we know that metallic species can hold high amounts of charge, and so have very high values for k, a value of 3.46 indicates that a fullerene molecule has more dielectric than metallic properties. This section has proven that the many-body theory can model both metallic and dielectric systems but it is when the linear fullerene chain is modelled as the latter that the system is more stable. With a relatively low

dielectric constant value and a stable system with charges found at large separation distances such as seen in Figure 3.2, the system is found to be stable. If the system were to act more metallic, with delocalised charge, the energy barriers to fragmentation are significantly larger, meaning significant energy would be needed for fragmentation. Therefore, we conclude agreement with Stace *et al.*[27] that fullerene systems can be treated as dielectric in nature, with charge localised to fullerene cages.

3.3 The Structure of $(C_{60})_N$ Clusters

As the structures of charged fullerene clusters were found to be independent of charge[61], the structures of the clusters are taken from the Cambridge Energy Landscape Database made available by Wales and Doye. They locate putative global minima for $(C_{60})_N$ clusters modelled by the potential of Pacheco and Prates-Ramalho up to N=105. These minima are based on icosahedral packing up to N=15, but above this size the lowest-energy structures are decahedral or close-packed[69]. To locate global minima for PPR potential basin hopping[70] (Monte Carlo plus minimisation[71]) was used as it has been found to be a very effective method for a variety of cluster systems.

3.4 Position of Charges in the Fullerene Cluster

As experimental techniques such as TOF mass spectroscopy cannot provide details on where the charged fullerenes may sit in the cluster, we investigate as many different charge placements as are computationally feasible. The energies of all possible charge placements were calculated for clusters with charges $2 \geq q \leq 4$ and stability with respect to fragmentation was investigated. As the amount of charge on a cluster increases, even by one, there is a dramatic increase in the number of fullerenes involved. This presents a significant com-

putational challenge. Taking as an example, the experimentally found cluster size for q=+4 is only stabilised by 21 fullerenes. There are 5985 viable ways to arrange the charges on the cluster.

3.5 Calculating Minimum Stable Cluster Sizes

Following Martin's[56] 1993 experiment which detected the existence of doubly and triply charged clusters and concluded that the mass distribution of these multiply charged clusters were similar to that of the singly charged, there has been further investigation into multiply charged fullerene clusters —more specifically, the minimum stable size for charges (q) from 2 to 7[4]. The most plausible channel of decay for multiply charged clusters is the emission of a monomer ion in the form:

$$C_{60_n}^{q+} \rightarrow C_{60_{n-1}}^{q-1} + C_{60}{}^{+} \tag{3.4}$$

Which has been proven by Nakamura *et al.*[4] to be the lowest dissociation channel up to z equal or less than 7. It was previously proposed by Zettergren *et al.*[3] that fragmentation would involve a symmetric or near symmetric separation of charge due to complete delocalisation across a dimer of conducting spheres. It is plausible that the reason this is not the case, and emission of a singly charged fullerene occurs, is that the high charge density on the larger fragment will strongly polarise the $C_{60}{}^{+}$ fragment and this strong attraction will lower the magnitude of the outward reaction barrier. This results in Coulomb repulsion being seen at larger fragment separations and a reduced kinetic energy release. This was modelled previously by Stace *et al.*[27] using a two-body dielectric particle model which was a first as, although there are many models to analyse data on Coulomb fission from fullerenes and such molecules, the dielectric particle model recognises them as dielectric materials. For each value of q^{+}, n was varied until $C_{60_{n-1}}^{q-1} + C_{60}{}^{+}$ became attractive at

short distances and this value of n was taken as minimum stable size. Due to the discussion upon the accurate value of the dielectric constant of fullerene, they used values of both 3 and 5 as shown in Table 3.2.

Table 3.2: Minimum stable size structures of $C(_{60})_n^{z+}$ with respect to the process $C_{60\ n}^{q+} \rightarrow C_{60}{}_{n-1}^{q-1} + C_{60}{}^{+}$ from Stace's[1] two-body model using values for the dielectric constant of 3 and 5, experimental values[2, 3], another two-body theory[4] and results from the many-body electrostatic theory presented in this work.

	Two-body model (n)[1]			**Theory[4]**	
q	$k_i = 3$	$k_i = 5$	**Expt.[2, 3]**	$k_i = 3.46$	**This work**
2	8	6	5	7	6
3	18	11	10	13	14
4	33	20	21	23	22
5	50	33	33	31	36
6	71	45	-	35	
7	96	56	-	38	

In previous calculations[27] using two-body theory[24] the size of one sphere was calculated using a liquid drop approach, $a_2(n) = r_0 n^{1/3}$, where r_0 is the radius of a single C_{60} molecule and minimum stable sizes were calculated. As Table 3.2 shows, the results are very sensitive to the value of k_i chosen, but with a value of 5 the experimental values were reproduced very closely. The experimental data[2, 3] has also been the focus of theoretical analysis by Zettergren *et al.*[3] who accounted for stable $(C_{60})_n^{q+}$ structures by using a nearest-neighbour model that localised charge on individual C_{60} molecules in order to minimise Coulomb repulsion. Similarly, Nakamura *et al.*[4] used a contact sphere model to calculate the energy barrier for the loss of one or more charged fullerenes but didn't consider the dielectric nature of C_{60} outside of the repulsive Coulomb contribution to the total energy of a charged cluster of fullerenes. These models have one thing in common; they all model large fullerene clusters using two-body solutions.

However, a knowledge of two-body forces is often not sufficient for a quantitative description of processes that involve interactions between more than two charged particles and, under these circumstances, a solution to the more

complex problem of multiple particles interaction is required. The calculations presented here improve upon work from the previous publication shown in Table 3.2[24] by implementing the recently developed integral equation[34] approach introduced in Chapter 2 to calculate many-body electrostatic interactions in charged fullerene clusters. Van der Waals interactions are calculated using the Pacheco and Prates-Ramalho (PPR) intermolecular potential[5] based on first-principles determination of the dispersion interaction between fullerenes, using time dependent density functional theory.

Interaction energies, which are a summation of Coulombic, multipolar and vdW energies, were compared before and after the loss of a charged fragment. A lower interaction energy before fragmentation can imply that the cluster will not fragment and so we can classify the structure as stable. Such interaction energies are shown in Table 3.3. Previous work[24] using a two-body solution looked at fullerene clusters using multiple dielectric constants. However, using the Clausius-Mossoti formula in equation 3.1, we can now confidently use the 3.46 value [4]. The minimum stable sizes using this approach are shown in the final column of Table 3.2 and are depicted in Figure 3.6, which shows the stable structures for clusters with charges of +2, +3 and +4 where clusters of 6, 14 and 22 fullerenes are required to stabilise the respective charges. Additionally Figure 3.7 shows a stable 36-body cluster with 5 charges shown from different angles in order to see the placements of all the charges.

Table 3.3: Interaction energies of minimum stable size clusters (n) before and after fragmentation of a charged C_{60} for q=2,3,4 and 5.

q	Cluster Size	E_{int} of $(C_{60})_n^q$ (eV)	E_{int} of $(C_{60})_{n-1}^{q-1}$ + $(C_{60})^+$ (eV)
2	6	-2.5162	-2.3345
3	14	-9.3731	-9.2339
4	22	-16.366	-16.307
5	36	–31.207	-30.933

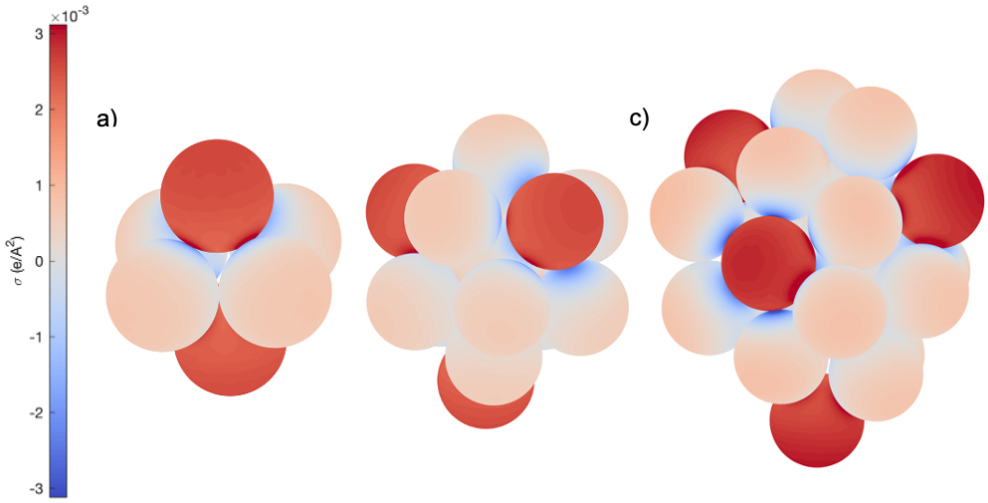

Figure 3.6: *Figures of the clusters of minimum stable size for a) 2 charges (6 fullerenes), b) 3 charges (14 fullerenes) and c) 4 charges (22 fullerenes). Shading on each particle depicts the calculated surface charge as being either negative (blue) or positive (red). Regions of more intense colouration correspond to enhanced charge due to the polarisation of bound charge.*

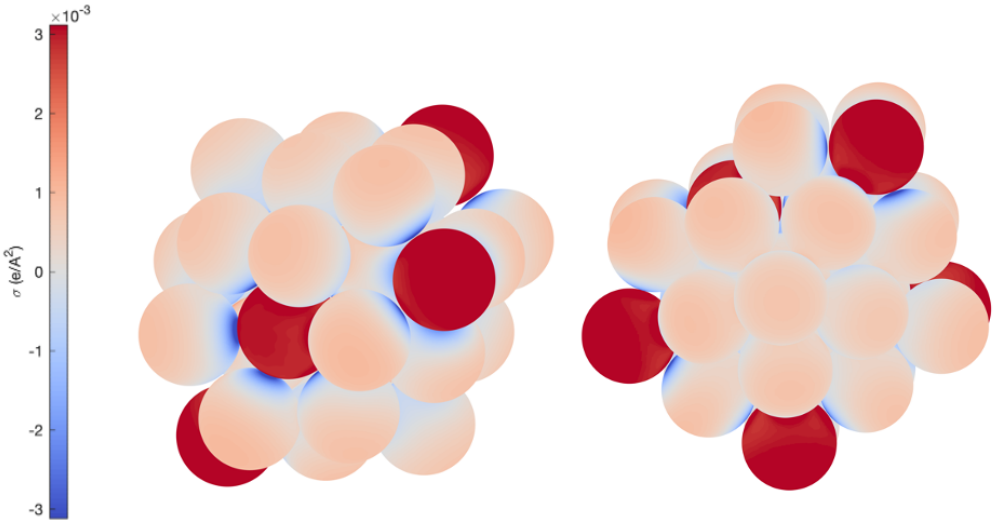

Figure 3.7: *Figure of the minimum stable size of 36 fullerenes for 5 charges, shown from two angles to indicate placement of all charges.*

Figure 3.8 shows the interaction energy as a function of fragmentation of a charged fullerene away from the cluster for clusters with 3, 4 and 5 charges respectively (doubly charged clusters are discussed in-depth later). Apparent from all three graphs is the high energy required to get to a distance of about 10 Å before a step energy decrease where long-range repulsive interactions take

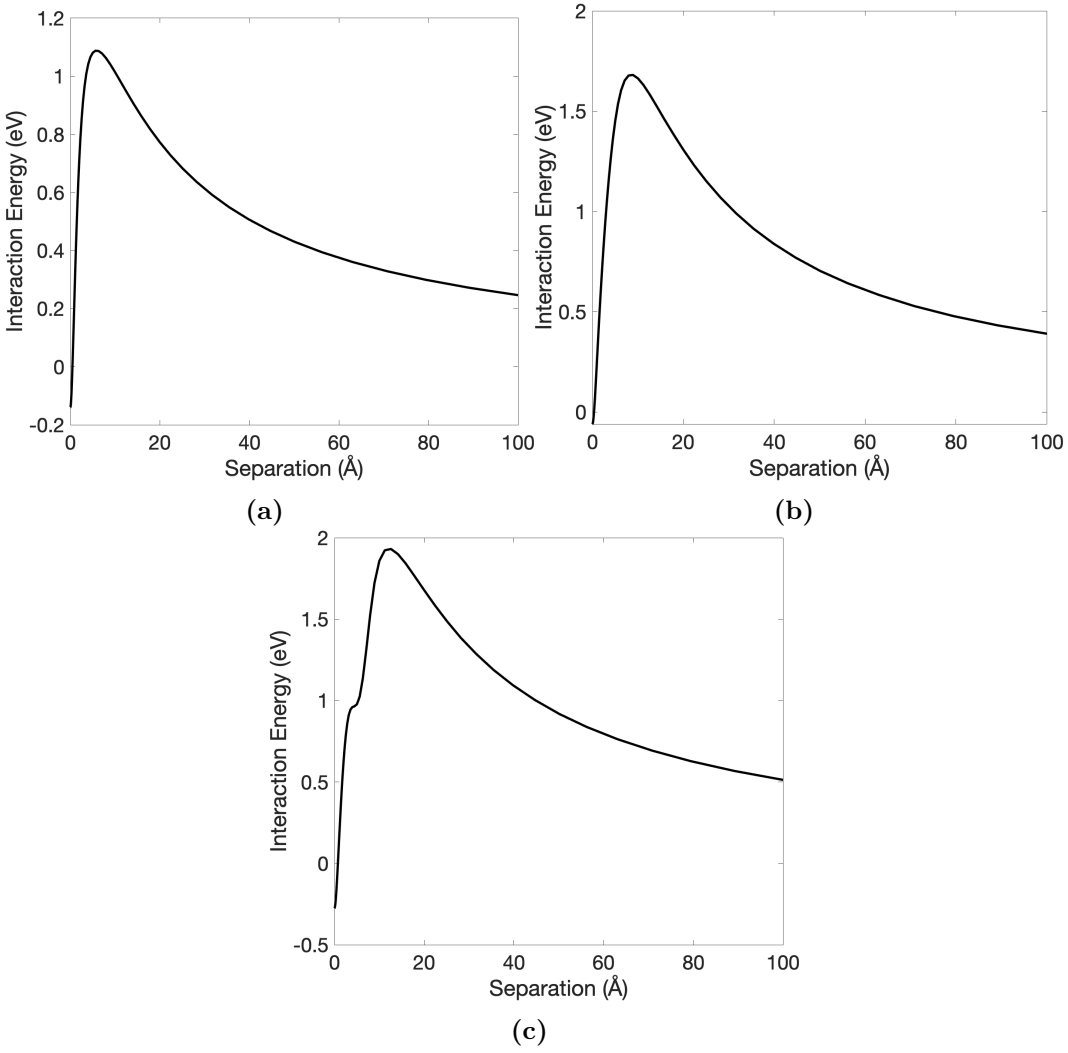

Figure 3.8: *Energy barriers for the fragmentation of a C_{60}^{+} from a (a) 14 body cluster with 3 charges, (b) a 22 body cluster with 4 charges and (c) a 36 body cluster with 5 charges.*

over.

The location of the peak of the separation graph appears at a distance equivalent to the diameter of one fullerene. In this range, short-range attractive interactions are dominant, requiring sufficient energy to overcome the barrier. What is unique is that in the q=+5 case we see a small peak appears before the large energy barrier, which is shifted to a larger separation distance than the other minimum stable size clusters examined here. This is due to the position of the charge, with it being on the surface but embedded as seen in Figure 3.7. The geometries of the smaller clusters led to less closely packed C_{60} on the surface, meaning the charged species was able to fragment with less force. The dip in the energy barrier seen in Figure 3.8(c) at $\leq$ 10 Å corresponds to the fullerene being pushed forward out of it's tightly fitting space in the cluster's face.

Table 3.4: Energy barriers of minimum stable size fullerene clusters with charges 2 to 5.

Cluster Size	Charge	Energy Barrier(eV)
6	2	0.8686
14	3	1.2271
22	4	1.7400
36	5	2.2050

The energy barrier to fragmentation increases with the size of the cluster and the number of charges, from 0.8686 eV in a 6-body system to 2.2050 eV in a 36-body system as seen in Table 3.4. Although Coulomb repulsion will be larger in those systems with higher charge, the drastically increasing size of the clusters comes with significant vdW stability. This, in turn, requires more energy to remove a fullerene from the cluster leading to heightened energy barriers.

It was previously found[27] that the fragmentation step of a doubly charged dimer had K.E release values of 1.60 eV or 1.68 eV depending on the dielectric constant used (3 or 5, respectively). This was vastly different from that found from the experimental work of Zettergren[3], where a value of 0.44 ± 0.02 eV was established. In the same paper as the quoted experimental data[3], the authors also presented some theoretical calculations of the K.E release values for multiply charged clusters. Their image charge calculations concluded a K.E release value of 1.1 eV for a doubly charged cluster, a value that sits inbetween their 0.44 eV experimental value and the 1.6 eV found using a two-body model [24]. Zettergren *et al.*[3] suggest that their lack of agreement in experimental and theoretical values are due to high levels of internal excitement in the reaction products.

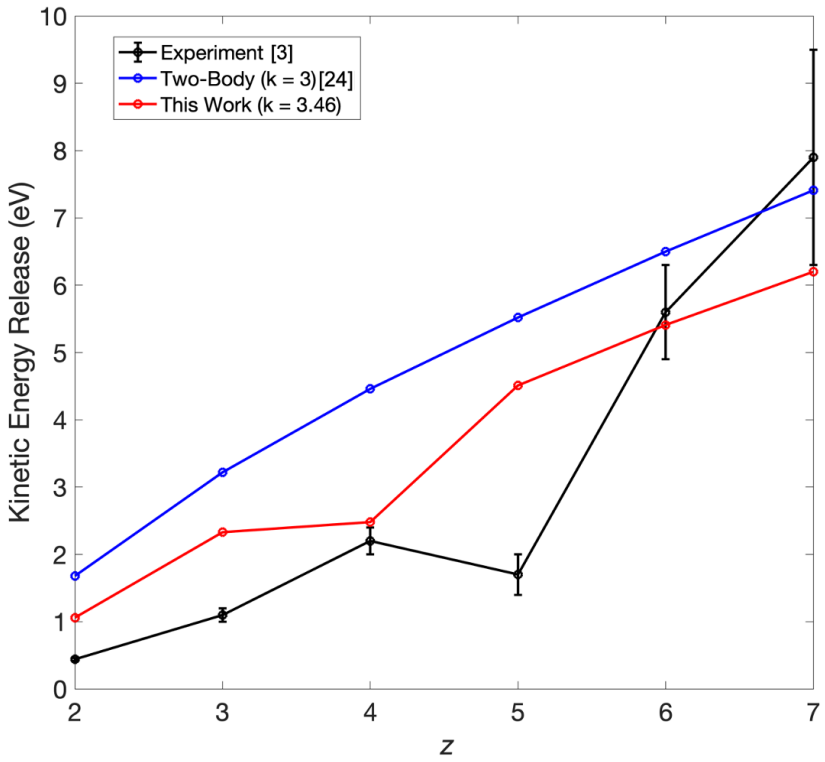

Figure 3.9: *Kinetic Energy release values for dimers with charges 2≥q≤7 for experimental values (black), values using two-body theory (blue) and many-body theory (red).*

For values of q up to 6, many-body theory more closely matches experimental values of kinetic energy release than the pairwise potentials. However, the values are still consistently larger due to significant errors associated with the experimental results[3]. With a charge of +6, our calculations are only 0.19 eV different to Zettergren's calculations, as can be seen where the black and red lines cross on Figure 3.9. At the highest charge, q=7, we see two-body theory appearing to give better predictions but this cannot be stated with much certainty as the error of ± 1.6 eV associated with this value means that the calculated value of 6.2 eV here is still in the accepted range.

3.6 Fragmentation Pathways

Whilst we acknowledge the high energy barriers present in some of these cluster fragmentations, as we explored in Figure 3.8, we are aware that there are numerous possible mechanisms of how the charge could be expelled and that some of those will be lower in energy than the way seen above. For a doubly charged cluster, we have established that at least 6 fullerenes will be required to stabilise such charge. Below, we explore possible fragmentation of doubly charged clusters of sizes 4≤n≤6.

Table 3.5: Kinetic energy release values for doubly charged clusters of 4, 5 and 6 fullerenes

Cluster Size	No. of Fragmentation Steps	KE (eV)	Energy Barrier (eV)
4	2	-0.5981	0.1661
5	1	-0.6062	0.1727
5	2	-0.6071	0.1726
6	2	-0.5992	0.1763

Table 3.5 shows the kinetic energy release values for doubly charged clusters where 4≤n≤ 6. It is assumed that fragmentation is an over-the-barrier process and that kinetic energy is determined from a maximum in potential energy with respect to infinite separation of the parent cluster and the fragment. It

is clear from the fragmentation graphs and Table 3.3 that 6 fullerenes are required in the cluster to stabilise two positive charges, as this is the smallest cluster where the interaction energy is lower before than after fragmentation of a charge.

The kinetic energy release for different size clusters, and also for different fragmentation pathways, is always similar as seen in Table 3.5. The average K.E release being -0.60265 eV. With two-body modelling, employing a two-body model [24], multiple fragmentation steps were considered, however it has since been established that the emission of a single, charged fullerene is the lowest in energy as proven by Nakamura's calculations on clusters with charges *et al.*[4] up to q = 7. This is due to the fact that emission of a singular particle results in a smaller reduction in attractive vdW energy but the same reduction in repulsive Coulombic energy than if multiple fullerenes were to be emitted at once as can be seen from Figures 3.4 and 3.2.

To confirm the conclusion of Nakamura's work[4], that emission of a singular, charged fullerene is the most likely fragmentation pathway, we calculated the kinetic energy release values for this pathway alongside fragmentation pathways involving emission of multiple fullerenes. In large fullerene systems, we expect substantial stabilisation from vdW interactions, as discussed in Chapter 2. Emission of a charged fullerene and its charge neutral neighbours from a cluster results in the same reduction in Coulomb repulsion as just fragmenting the charged fullerene alone, but with an additional reduction in attractive vdW energy as the remaining cluster now has less charge neutral fullerenes to stabilise the remaining charges. In smaller, less close-packed structures such as the 5-body linear chains discussed earlier in this Chapter, there are significantly less stabilising vdW interactions and so a more symmetrical split is energetically favourable.

Figure 3.10 shows that a 4-body structure begins as a tetrahedron, with two charged and two neutral components. Here, at Phase 0, we see a stable structure with an interaction energy around -0.5 eV; stabilised by significant vdW and multipolar interactions, despite significant Coulombic repulsion from the charges in contact. This repulsion drives a rearrangement where we see the rotation of the charge, seen on top of the trigonal base in the image for Phase 0, rotated around the y and z axes to rest at the point furthest from the other charged particle. We can see, Phase I, that the two charges are now separated by the two neutral C_{60}. As Figure 3.10 suggests, this creates a new interaction energy minimum as the reduction in repulsion outweighs the minor loss of vdWs and multipolar interactions in this less closely packed diamond configuration. From here, the charge rotates until it is in line with the other charge and the central neutral particle as seen at Phase II. In this position, the charge can fragment to infinity (Phase III); it only has to break a single vdW connection, meaning a much lower energy barrier to overcome than fragmentation from, for example, the Phase 0 configuration where the charge was in contact with all three other fullerenes. At the end of this pathway, we are left with a 3-body, singularly charged cluster that is more energetically stable than the 4-body, doubly charged cluster - implicit of an unstable starting structure.

A doubly-charged trigonal bipyramidal structure (n=5) will separate the charges in order to minimise Coulombic repulsion. This is what we see at Phase 0 of Figure 3.11. This is the furthest charge separation possible and hence the most stable configuration for 5 spheres, due to minimised repulsion and significant attractive interactions that come with closely packed structures. However, as we have seen, the removal of a charge from this shape comes with a high energy barrier to overcome. Much like that discussed for the tetrahedron configuration in Figure 3.10, we see the charged spheres in contact with three other fullerenes - three interactions to break at once if the charge were to fragment from here. That is why we propose the rotation of the top charge to the side

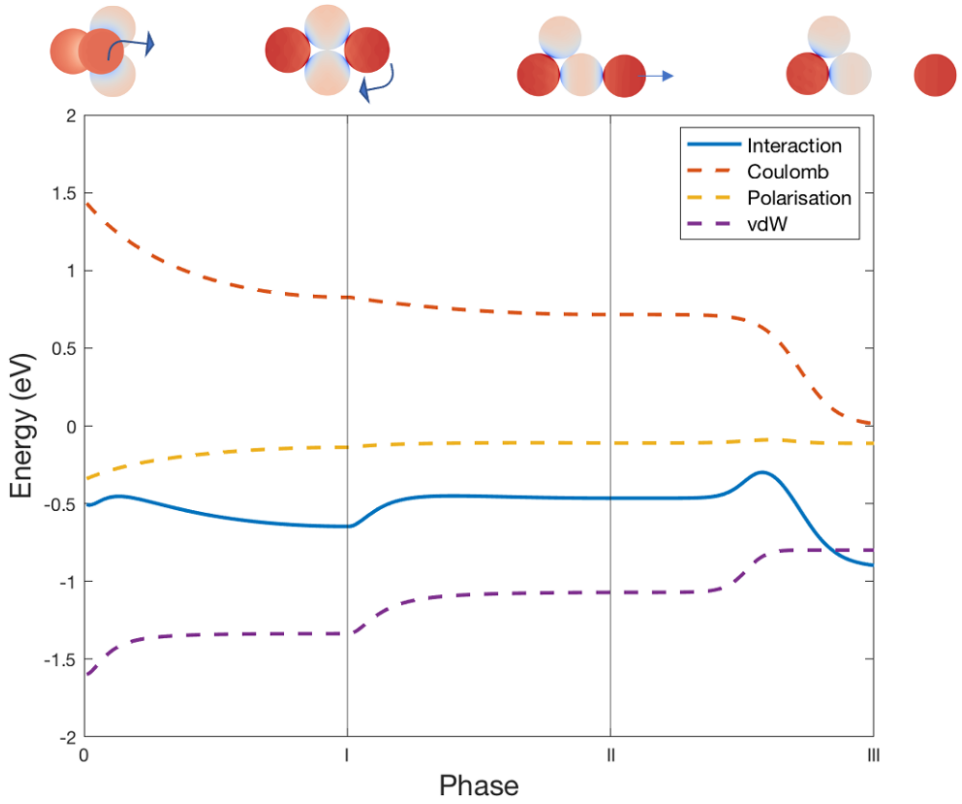

Figure 3.10: *Graph showing the fragmentation pathway for a 4 body cluster with 2 charges. The solid blue line represents the total interaction energy of the process with the dashed lines representing the contributions to that energy. Red is Coulomb, yellow is polarisation and purple is vdWs.*

of the structure at Phase I. The transition from Phase 0 to Phase I breaks two of the three vdW interactions, losing about -0.5 eV of attractive energy. Then when we see fragmentation to Phase II, there is less of an energy barrier as there is only one more vdW connection remaining. Although we still see lower interaction energy at Phase II than Phase 0, there is much less difference than that of a 4-body, implying that 5 fullerenes was nearly sufficient to stabilise the two +1 charges.

Similar to Figure 3.11, in Figure 3.12 we explore the same pathway but with an extra step so there is only the loss of one vdW bond at a time instead of the double break we saw at Phase I of Figure 3.11. Depending on the time-frame of the Coulomb fission, it is possible that the pathway could be that of either Figure 3.11 or Figure 3.12. The final step gives the same energy barrier

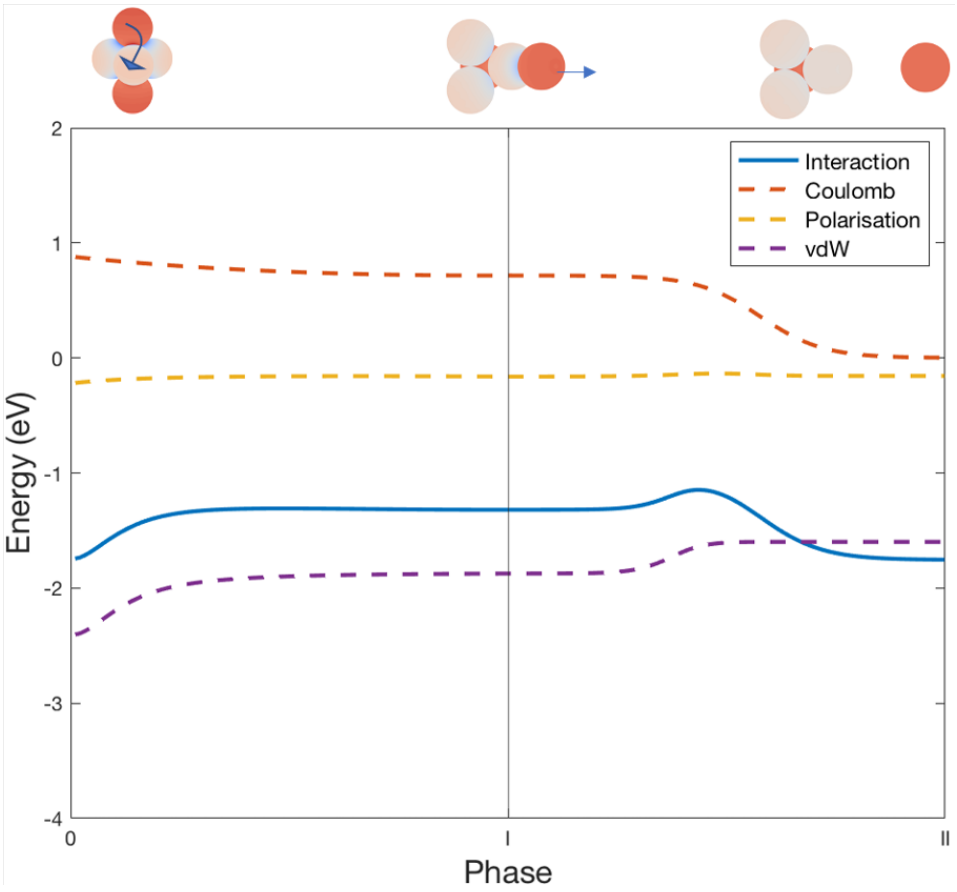

Figure 3.11: *Graph showing the one-step fragmentation pathway of a 5 body cluster with 2 charges. The solid blue line represents the total interaction energy of the process with the dashed lines representing the contributions to that energy. Red is Coulomb, yellow is polarisation and purple is vdWs.*

for both as shown in Table 3.5, but we see a smoother energy profile in the three-step process with minimal change in vdWs and Coulomb energies until the emission of the charge.

As established in Table 3.4, 6 fullerenes are required in a cluster to stabilise two positive charges. The values in this table for charges from 2 to 7 were found by comparing energies before and after fragmentation. The fragmentation being direct removal of the charged C_{60} from the cluster in the direction of the force acting upon it due to the other charge in the system as seen in P1 in Figure 3.13.

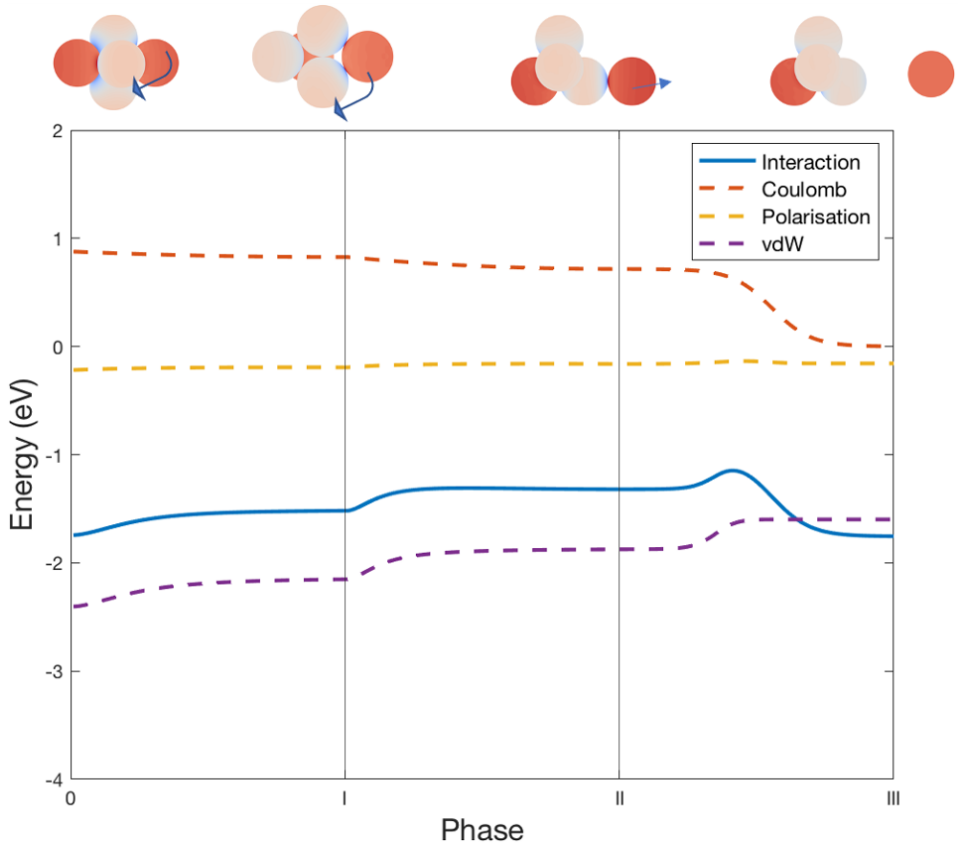

Figure 3.12: *Graph showing the two-step fragmentation pathway of a 5 body cluster with 2 charges. The solid blue line represents the total interaction energy of the process with the dashed lines representing the contributions to that energy. Red is Coulomb, yellow is polarisation and purple is vdWs.*

Figure 3.13: *P1: Fragmentation of charge from a doubly charged 6-body cluster, in the direction of force, from cluster in one step process.*

The separation graph for this fragmentation is shown as the red line on Figure 3.14. There is a significant energy barrier as the charge is removed and multiple vdWs connections are broken.

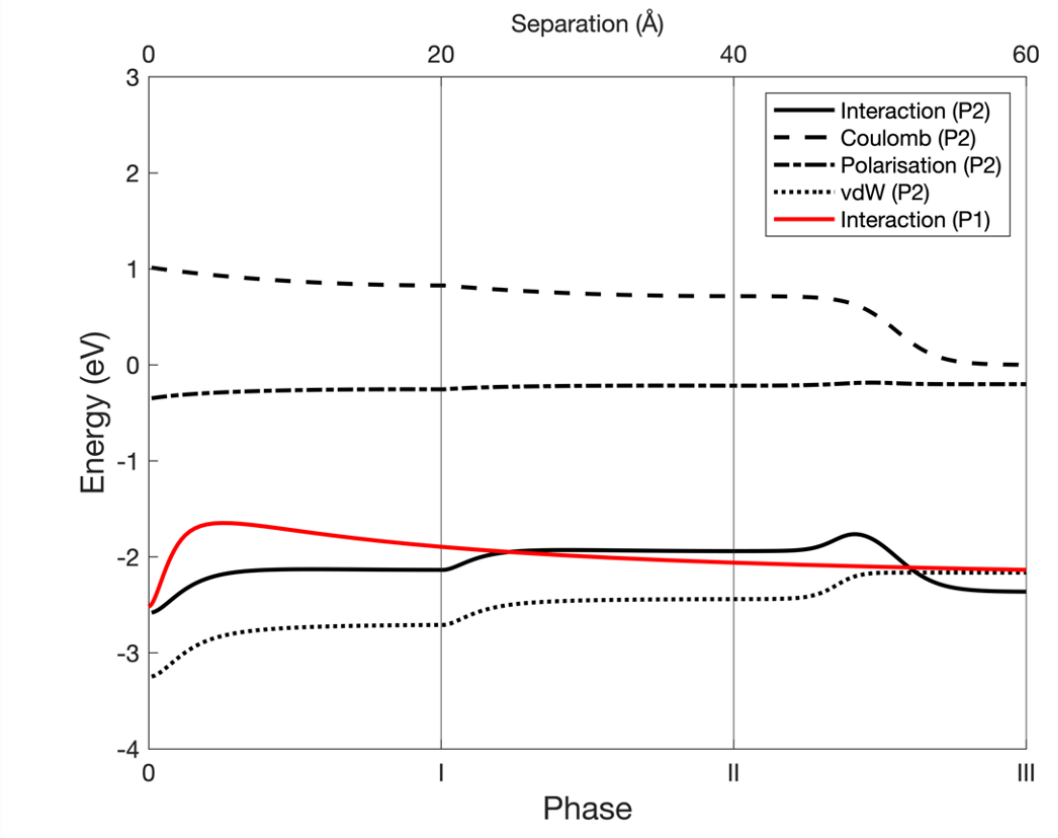

Figure 3.14: *Graph showing the three-step fragmentation pathway of a 6 body cluster with 2 charges (P2) in comparison to straight repulsion of the fullerene from the cluster (P1).*

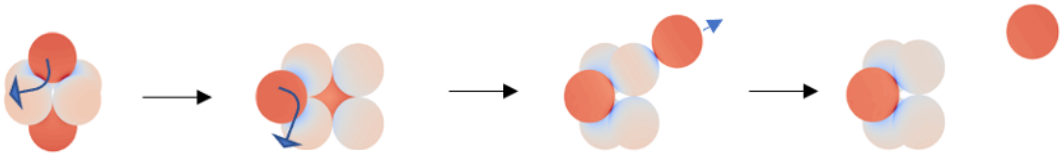

Figure 3.15: *P2: Fragmentation of charge from a doubly charged 6-body cluster in 4 phases. At phase 0, the cluster is in complete. By phase 1, the charge has rotated from the center of the tetrahedral base to now only have 2 connections. By phase II the charge is now only touching one neutral sphere and from here it fragments as seen in the final phase, III.*

We have found that a cluster of 6 fullerenes, such as that shown at Phase 0 of Figure 3.14, is required to stabilise two charged fullerenes, with the four and five-body structures discussed above being too small to sufficiently spread out the Coulombic force between the charges. The energy barrier for the 6-body structure was concluded to be 0.8686 eV in Table 3.4, if the charge were to be emitted by breaking all vdW connections instantaneously, which is unlikely.

The pathway shown in Figure 3.15 is proposed to be the most energetically favoured way of fragmentation, lowering the energy barrier to just 0.1763 eV.

This case study of doubly charged clusters of sizes $4 \leq n \leq 6$ acts to suggest that the energy barriers stated in Table 3.4 are overestimates of the fragmentation process. By breaking down the pathway we can conclude that the energy barrier for a n=6 cluster is actually nearly 5 times less. This finding can be carried over to all the values in Table 3.4, giving much more achievable energy barriers for the process to overcome.

3.7 Predictions for +6 and +7 Charged Clusters

The complexity of calculation and the computational cost of exploring many-body interactions in large, multiply charged clusters is exponential. As mentioned beforehand in the discussion of charge placements, an increase of even one more charge in a cluster can substantially increase the number of neutral fullerenes needed to facilitate overall stability. The results presented so far cover multiply charged clusters where the charge ranges from 2 to 5, with a cluster size of 36 being found to be the minimum stable size required for a charge of 5. There are 376,992 ways that 5 charges can be placed on a 36-body cluster - testing that many charge placements and removing one charge at a time to monitor the change in interaction energy begins to require drastic computational time. Although we were able to investigate all charge placements and the removal of all included charges from the cluster for charges +2, +3 and +4, the jump in size to accommodate a +5 charge means modelling of the most stable charge placements, and those within kT of the minimum, could be investigated.

When the charge increases to +6 and +7, where there are only predictions from two-body computational methods[27], we can see predictions of cluster sizes rising to 96. At this point there are 1.19 x 10^{10} different ways to place charge. Trying to investigate the stability before and after fragmentation for this many different clusters would be computationally unfeasible with the current level of theory development. Further enhancement of the FMM is currently in progress[72], meaning that in the near future it will be achievable to produce a quantitative answer for clusters with charges $\geq$ +6.

Previously, Bichoutskaia[24] predicted a minimum stable size of between 45 to 71 for a +6 charged cluster, with dielectric constants of 3 and 5, respectively. The dielectric constant of 3.46[4] used in this work sits between these values and so we would assume that we would find a minimum stable size in this range. We found a 71-body cluster with 6 charges to be stable with respect to fragmentation by implementation of the many-body electrostatic theory. Figure 3.16 shows a figure of the stable structure with its 6 charges spread across the surface.

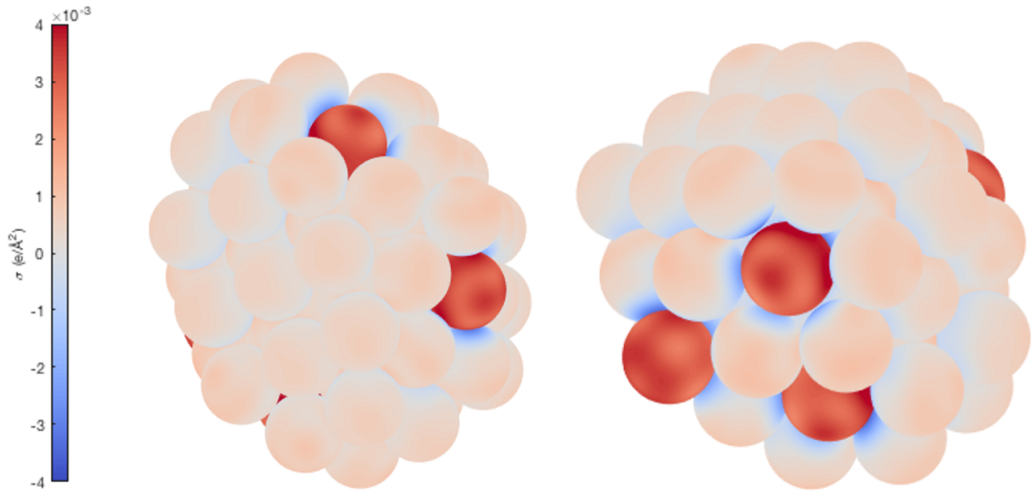

Figure 3.16: *Figure of the minimum stable size of 71 fullerenes for 6 charges, shown from two angles to indicate placement of all charges.*

The structure in Figure 3.16 was found to have a more negative interaction energy before fragmentation, as is shown in Table 3.6, than after it loses a charge - implying it would rather keep that charge than fragment and so we can call it a stable structure with respect to fragmentation.

Table 3.6: Total, Coulomb, Polarisation and vdW energy for a 71-body fullerene cluster with 6 charges before and after fragmentation of a C_{60}^{+}.

Fragmentation Distance (nm)	**Interaction Energy (eV)**	**Coulomb Energy (eV)**	**Polarisation Energy (eV)**	**vdW Energy (eV)**
0	-74.3819	9.1379	-2.923	-80.5967
1e6	-74.2779	6.4693	-2.525	-78.2221

The loss of a C_{60}^{+} results in a reduction in the stabilising vdW interactions as is the case here, as seen in Table 3.6. However, as we investigate larger and larger cluster sizes, the loss of a single fullerene has less and less impact relative to the substantial vdWs that stabilise large clusters. This loss, alongside a reduction of 0.398 eV in attractive multipolar interactions, outways the reduction in Coulomb repulsion that comes from the loss of a charge, making fragmentation of this charge energetically unfavourable overall.

This prediction is only based on the fragmentation of one specific charge. We found that if any another charged particle were to leave then the system would be lower in energy after emission of the charge and so then the starting cluster would be unstable with respect to fragmentation of the charge.

The charge we have investigated the fragmentation for in Table 3.6 is shown below in Figure 3.17, and although it is still on the surface of the cluster and not central, it is well-embedded. Additionally, it is in contact with multiple other fullerenes meaning that in order for it to fragment away from the cluster, multiple vdW interactions would have to be broken. This is likely why the structure is stable with respect to the fragmentation of this charge and not others. Removal of other charges, with fewer contacts to neutral neigh-

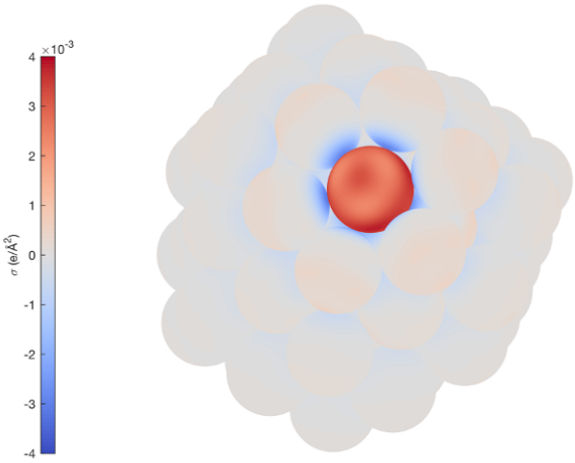

Figure 3.17: *Figure of the minimum stable size of 71 fullerenes with just the fragmenting charge shown.*

bours, will give the same reduction in Coulombic repulsion but with a smaller decrease in vdW energy. As we have investigated above, the emission of a charge by breaking of all vdW interactions at once is not the most energetically favourable way to fragment and a slower, step by step fragmentation is more likely.

Chapter 4

The Significance of Induced Electrostatic Interactions for the Controlled Fabrication and Stability of Binary Nanoparticle Superlattices (BNSLs)

4.1 The Self-Assembly of Binary Nanoparticle Superlattices

The 'bottom up' assembly of small building blocks into macroscopic structures is a process commonly seen throughout chemistry, biology and material science[73]. Self-assembly of binary components of large and small colloidal particles was the centre of much attention in material science in the 1980s. Chemical methods developed over the past two decades have enabled these colloidal components for self-assembly to be extended from micrometer-sized such as silica[74] to nanometer sized nanoparticles which can be of differing intrinsic properties. The assembly of nanoparticles of two different materials

into a binary nanoparticle superlattice (BNSL) can provide an inexpensive mechanism which leads to a large range of materials with precisely controlled chemical compositions and thus unique bulk properties. Binary sphere mixtures often pack more densely than a single component alone, for example, by filling the voids in a close-packed lattice with smaller spheres.

BNSLs form through an inexpensive self assembly process. Self-assembly of ordered arrangements was first investigated using micrometer-sized spherical beads with a silica core and organic stabilising layer[75, 76]. Progression from here has seen the self-assembly of different colloidal particles of varied sizes become widely studied for purpose in many areas including in solar cells and thermoelectric devices[73]. Simply confining the colloidal particles in a small amount of solvent will lead the particles to form ordered arrays, without any other external stimuli. This is driven by the increase in translational entropy of the particles which arises from maximising the free volume that is available to each particle[73]. This entropy driven crystallisation favours the most densely packed arrangements, as has been shown in many studies[77, 78].

The beauty of BNSLs is that you can combine materials with any desired property. It is possible to combine metals, semi-conductors, ferroelectric, magnetic, dielectric and other materials. This, alongside the relative size of the component nanoparticles, are the primary parameters for fabricating arrays of particles. The creation of new materials[79] with a wide variety of unique and novel electronic[80], optical[81] and magnetic[82] properties, together with lattices shown to possess new thermoelectric[83] and chemical[84] characteristics can all come from the controlled formation of ordered arrays into BNSLs. Since nanoparticle superlattices can perform functionalities that their individual component atoms or molecules cannot, they have proven themselves as a new type of material which has novel and potentially revolutionary applications in areas including but not limited to metamaterials, catalysis and novel

energy sources.

Directing the outcome of the self-assembly process can also be achieved through templating, using interactions with a structure or electric field in order to manipulate the arrangement of the crystal[85, 86] and the resulting superlattice can be manipulated with ligands, including DNA[87]. The self-assembly process is reversible with the addition of solvent causing the superlattice to break down into its constituent particles[88]. Therefore, the stability of self-assembly of a superlattice is directed by the forces at play in the structure. Generating stable equilibrium structures relies on achieving a minimum in the Helmholtz free energy (F),[89] which can be expressed in terms of an internal energy (U),[90] together with the system's entropy (S) and temperature (T):

$$F = U - TS \tag{4.1}$$

where contributions to U come from a combination of van der Waals and electrostatic (permanent and induced) interactions[90]. The presence of capping layers on polymer chains present an extra intricacy as they can often soften particle-particle contact. This is quantified by a *softness* parameter which is discussed further in 4.2.2. In all cases, entropy will only make a favourable change to the free energy if that of the binary lattice is higher than the sum of the entropies of separate lattices formed from the individual components.

In close-packed, single component structures, such as face centered cubic or hexagonal close packed, the maximum packing fraction is ρ=0.7405. Binary mixtures of different-sized particles can be characterised by a size ratio, $\gamma = a_{small}/a_{large}$. where a is the particles radius. In some AB_n, values of $\rho > 0.7405$, can be achieved where vacancies generated within a close-packed structure of large particles can accommodate the smaller particles[89, 91]. Superlattices that are isostructural with NaCl and AlB_2 and composed of hard-

spheres are stabilised through favourable changes in entropy[77, 92, 93] and so produce these high packing fractions. There is, however, a diverse range of BNSL structures with packing fractions that are significantly less than this 0.7405 value. For these lattices, entropy alone is not sufficient to account for their stability, meaning that other factors must be taken into account when discussing favourable changes in free energy[73, 90, 91]. Of the contributing forces to the internal energy, the long-range Coulomb interactions between oppositely charged particles are particularly influential[73, 90], whereas the contribution to U from van der Waals interactions are insufficient to solely account for the stability of low density structures[90].

4.2 Computational Parameters

The systems used in this body of work use the packing of frequently observed lattice types —such as NaCl. The particles in such a lattice, however, do not have the chemical properties of such atoms. I.e. in a NaCl lattice type, the particles in the positions of Na and Cl are dielectric spheres with given sizes and dielectric constants which are in the same 3D space of the lattice-type being investigated. The types of particles that could be included in the model are concentrated colloidal solutions, Coulombic crystals, fullerenes and hard spheres as discussed in Chapter 2.

In this chapter, systems have been investigated as a function of their size ratio, $\gamma = a_1/a_2$, where the radius of the smaller particle (a_1) is varied during the calculations, and $a_2 = 5$ is a fixed radius assigned to the larger particle, meaning that γ varies from 0.05 to 1. Each particle is given a nominal charge, q, of one or a fraction thereof in accordance with the repeat formula unit of the isostructural crystal in order to ensure overall neutrality of the charge in each superlattice structure. Take for example an AB-type superlattice, here, each particle would be given a nominal charge of $q_1 = 1$ and $q_2 = -1$ respectively.

In an AB_2-type superlattice, particles in position B were assigned a nominal charge of 0.5 whereas particles in position A had a charge of -1.

For each system discussed in this work, the electrostatic interaction energy, E_{int} has been calculated as a function of the radius ratio, γ, between the two constituent particles. E_{int} is defined as the difference between the total interaction energy for the system and the sum of the individual self-energies, i.e.:

$$E_{int} = E_{system} - E_{self} \tag{4.2}$$

which gives the relative gain in energy that arises from the particles adopting a specific superlattice structure with respect to them being separated to infinity, as is discussed in more detail in Chapter 2. Actual energies are not reported in this chapter as instead the focus is on finding the more electrostatically stable structures out of those investigated here to use in future applications including those discussed in Chapter 5. Units are not used for energies or lengths in this chapter but energies (in eV) associated with the equivalent absolute charges used in this chapter can be recovered using the scaling relationship: $E = 1.4366 q_1 q_2 / r$, where r is a measure of the lattice cell size in nm.

4.2.1 Dielectric Constant

The results discussed in this work are for a medium which has a dielectric constant set to 1, which is representative of a vacuum, and a dielectric constant of 20 for all particles. This was chosen as a value that is a compromise between materials which are strongly polarisable, such as water, metals and some inorganic solids and those which are more weakly polarisable, for example, polymers and hydrocarbons. The consequences of employing a higher or lower value for the dielectric constant on lattice energy are shown in Figure 4.1.

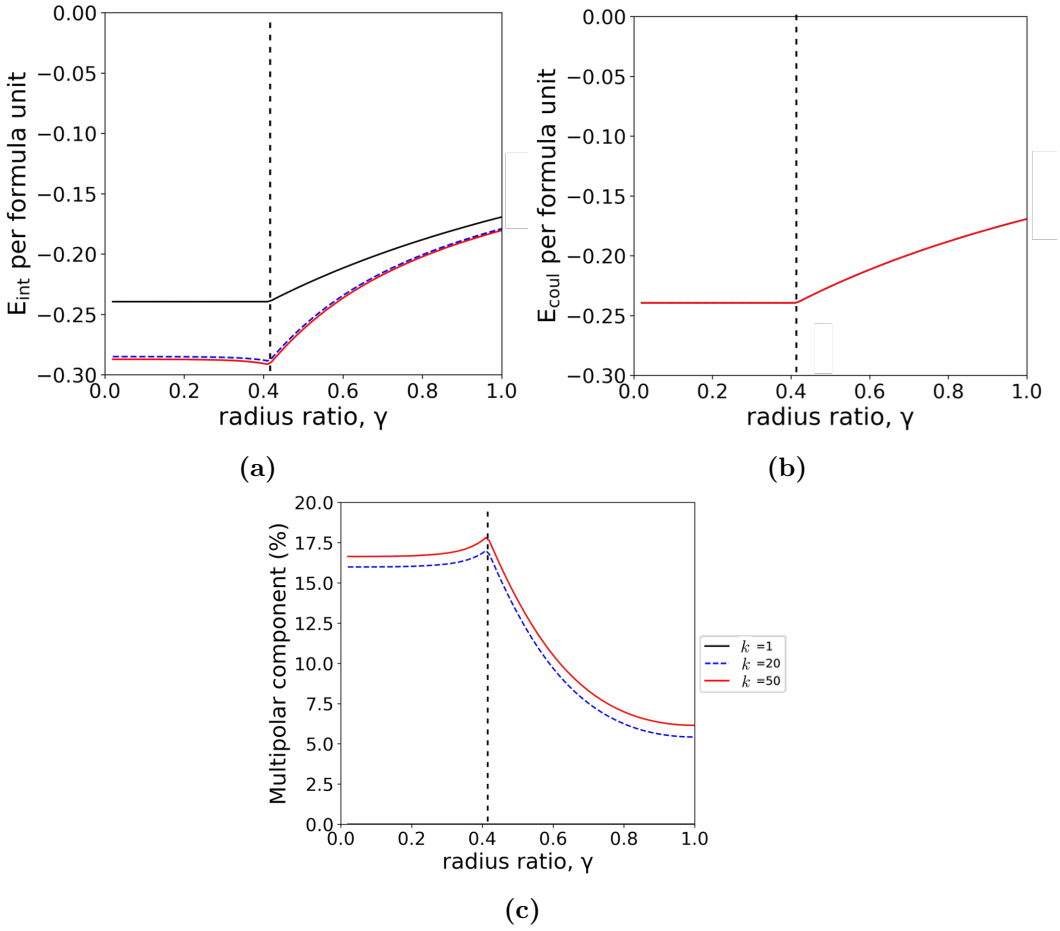

Figure 4.1: *Plots of interaction energy (E_{int}) in eV as a function of size ratio (γ) showing the effect of varying dielectric constant for a NaCl BNSL structure. Dielectric constant values of 1 (black), 20 (blue) and 50 (red) were used and the effect on (a) the total (Coulomb and multipolar) interaction energy, (b) Coulomb component and (c) % contribution from multipolar effects to total electrostatic energy. The dashed line is at a value of $\gamma_{electrostatic}$ for NaCl of 0.41.*

Figure 4.1 (b) shows the independent nature of Coulombic effects to changing dielectric constant. As might be expected, with the smaller dielectric constant, the energy curve is shifted towards higher (more positive) values whereas the significantly higher dielectric constant shows strong multipole contributions that increase the stability of the superlattice. There are no multipolar contributions when the dielectric constant is equal to unity as its absolute permittivity is equal to that of the medium; meaning, no polarisation of bound charges takes place. Such effects are going to be particularly noticeable for any lattice structures found to have a high contribution from polarisation to their stability. Figure 4.1 is for a NaCl lattice structure whose size ratio at the electrostatic

minimum ($\gamma_{electrostatic}$) is already established at 0.414[73], which as the graphs show is not changed by dielectric constant. As the dielectric constant is a measure of particles' polarisability, the structures which have higher contributions to stability from multipolar contribution will see a more significant increase in stability with increasing values for the dielectric constant.

4.2.2 Softness Parameter

An added complication for any interaction stems from the presence of capping layers of polymer chains, which can soften particle-particle contact and is quantified in terms of a softness parameter (s). Recent experiments have shown that a judicious choice of polymer chain can be used to fine-tune particle-particle length scales[94]. In many lattice structures composed of nanoparticles in the form of a BNSL, the particles generally consist of a solid spherical core covered by surface ligands that form the capping layer. Each particle then has an effective radius formed by the sum of the two components, the core radius (a) and the ligand length (l). Together, these characterise the softness parameter, $s = l/a$. Typically, $s \sim 0.01$ for micron-sized colloids, while $s \sim 1$ for nanocrystals.

While the ligands have a contribution to the interaction between particles, they also mechanically prevent any contact between cores. The main objective of this work is to consider the electrostatic interactions between hard particles, which in the case of colloids, is solely equivalent to the core. As it is desirable to consider the consequences of varying the softness parameter in terms of interpreting experimental data, calculations have been performed on a basic NaCl superlattice structure with s = 0, 0.5 and 1.

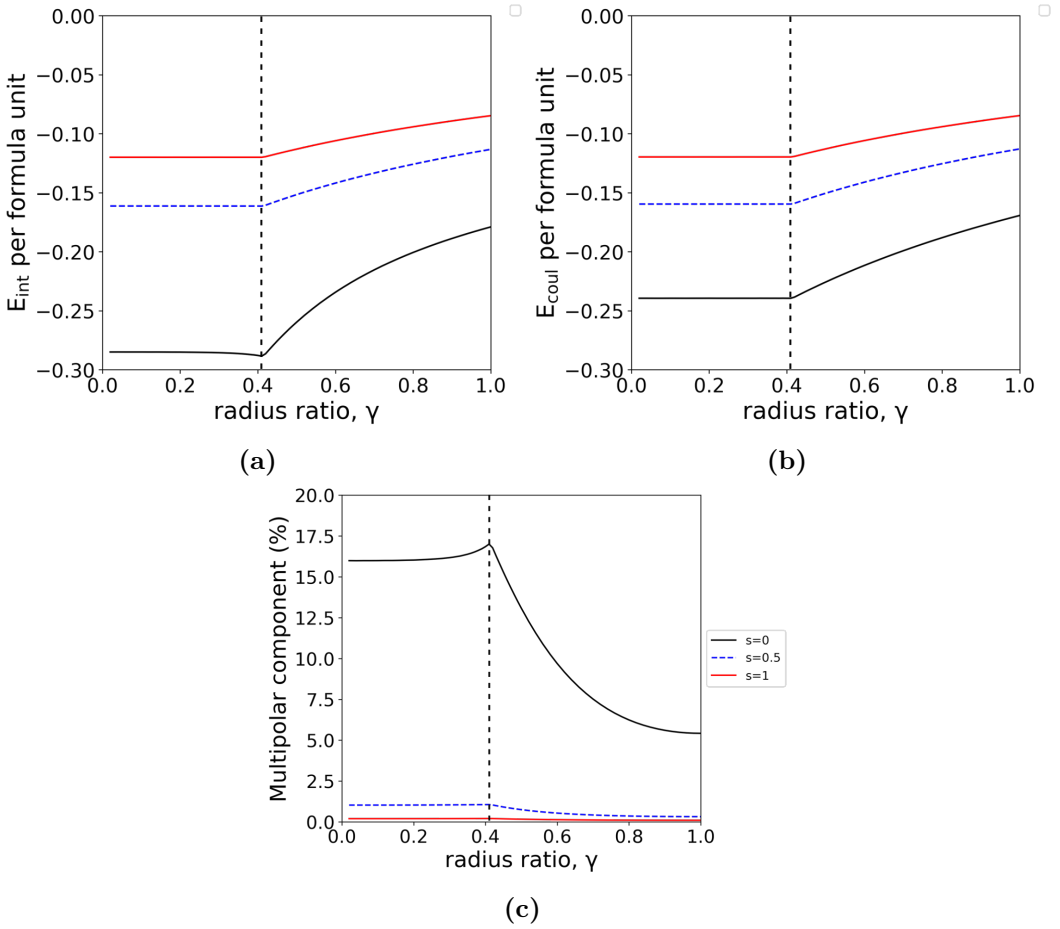

Figure 4.2: *The effect of varying softness parameter for a NaCl BNSL structure. Softness parameter values of 0 (black), 0.5 (blue) and 1 (red) were used and the effect on (a) the total (Coulomb and multipolar) interaction energy, (b) Coulomb component and (c) % contribution from multipolar effects to total electrostatic energy. The dashed line is at a value of $\gamma_{electrostatic}$ for NaCl of 0.41.*

As expected, Figure 4.2 shows that with decreasing softness parameter there is increased Coulombic and multipolar (and thus total) interaction energy. With a softness parameter ~ 1, there is minimal contribution to stability from polarisation effects due to the short range nature of polarisation and the increased core to core distance provided by the longer ligand causing the higher softness parameter. As found for dielectric constant, with varying softness parameter, the $\gamma_{electrostatic}$, where a_2 remains fixed in size and a_1 varies, remains unchanged.

4.3 Computational Calculations on Experimentally Observed BNSLs

The binary superlattices selected for this initial work have been taken from lattice types which are commonly observed in experiment, which are: AB, AB_2, AB_3, AB_4, AB_5 and AB_6[73, 90]. As input geometry for the calculations, the relative position of each particle in the lattice was obtained through accessing the Crystallographic Information File (CIF), made available through the *Materials Project* database[95].

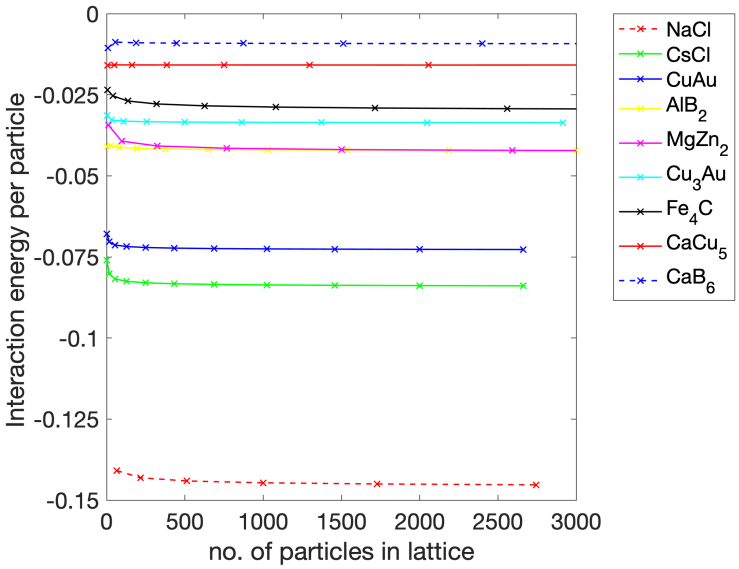

Figure 4.3: *The convergence of the interaction energy of the system dependent on the size of the structure for experimentally observed BNSLs. 1000 particles was chosen as a suitable minimum structure size for all lattice-types based on these energy profiles.*

For this work, the positions of equivalent atoms in a crystal with 1000 particles were used as input coordinates. This was decided because, as Figure 4.3 shows, at this size we can see that the energy of all the lattice types we wish to investigated have converged. Using lattice sizes smaller than 1000 wouldn't ensure the energy of all lattice-types had converged yet. Using lattice structures larger than 1000 particles would increase energy by $\sim 0.012\%$ (based on 1000 and 2744 particle NaCl structures) but 1000 particles is a compromise between accuracy of data and computational cost. Investigation into the significance

of induced electrostatic interactions in the controlled fabrication and stability of these systems will be discussed here but is described in detail in work by Lindgren *et al.*[38].

Table 4.1: Data on lattice types including giving atomic environment, $\gamma_{packing}$ corresponding to the radius ratio at which the maximum packing fraction taken from hard sphere studies and the$\gamma_{electrostatic}$, where calculations have found each lattice type to have a minimum in electrostatic energy. The last column gives the radius ratios, electrostatic, where calculations show each lattice-type to have a minimum electrostatic energy. Values in parentheses refer to the presence of local energy minima.

	Atomic Environment[96]	**Space Group**[96]	$\gamma_{packing}$	$\gamma_{electrostatic}$
NaCl	Na_6- octahedron Cl_6- octahedron	$Fm\bar{3}m$ (225)	0.41[90]	0.41
CsCl	Cl_8Cs_6- rhombic dodecahedron Cs_8Cl_6- rhombic dodecahedron	$Pm\bar{3}m$ (221)	0.74[89]	0.73
CuAu	Au_8Cu_4- cuboctahedron Cu_8Au_4- cuboctahedron	P4/mmm (123)	1.0[89]	0.91
AlB_2	B_{12} - hexagonal prism B_3 - coplanar triangle	P6/mmm (191)	0.53[89]/ 0.58[90]	0.58
$MgZn_2$	$Zn_{12}Mg_4$ - 16-vertex Frank-Kasper Zn_6 Mg_6-icosahedron	$P6_3/mmc$ (194)	0.82[89]/ 0.81[90]	0.81
Cu_3Au	Cu_8Au_4- cuboctahedron Cu_{12} - cuboctahedron	$Pm\bar{3}m$ (221)	1.0[89]	1.0
Fe_4C	C - single atom Fe_4 - tetrahedron	$P\bar{4}3m$ (215)	-	0.32
$CaCu_5$	Cu_{18} - sixcapped hexagonal prism Cu_8Ca_4 - cuboctahedron	P6/mmm (191)	0.65[89]	0.46 (0.73)
CaB_6	B_{24} - truncated cube (dice) B_5 - square pyramid	$Pm\bar{3}m$ (221)	0.41[97]	0.40

Nine examples of frequently observed superlattices recorded from experiment are recorded in Table 4.1 along with the size ratios which have been calculated to give stable structures at their energy minima. The results correspond to hard particles ($s = 0$) where it can be seen that for each system there is a clearly defined value of γ where the energy is at a global minima. From a comparison of the calculated results with the radius ratios found at the max-

imum packing fractions, which were determined from experiment, it can be noted that, for almost every lattice type there is good agreement between $\gamma_{packing}$ and $\gamma_{electrostatic}$. As a high packing fraction indicates that particles are generally closer to one another, favouring opposite charge interactions, this agreement would be expected.

Images showing the unit cells of the BNSL isostructural with those in Table 4.1 are shown in Figure 4.4. Similarities between structures with the same space group, such as CsCl and Cu_3Au or AlB_2 and $CaCu_5$, can be seen from the images in Figure 4.4.

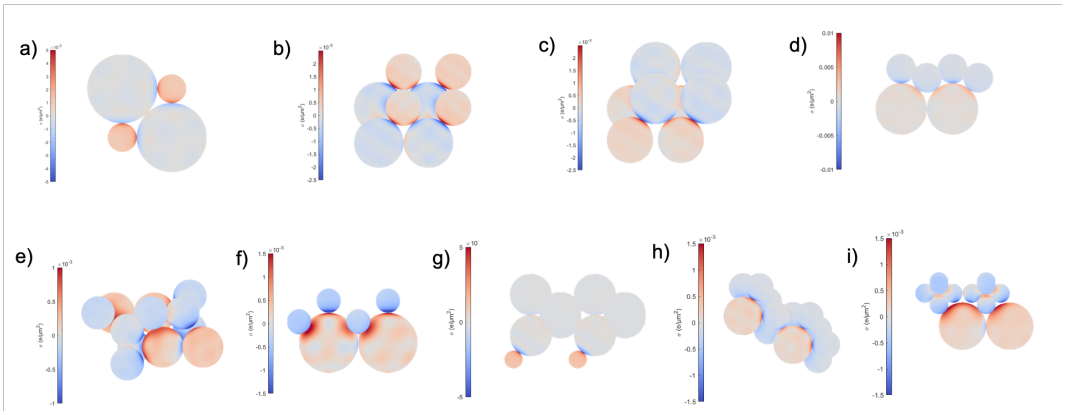

Figure 4.4: *Images showing the BNSL isostructural with a) NaCl, b) CsCl, c) CuAu, d) AlB_2, e) $MgZn_2$, f) Cu_3Au, g) Fe_4C, h) $CaCu_5$ and i) CaB_6 at the radius ratio at which the structure is at a minimum in electrostatic energy.*

For hard particles (s = 0), the results of varying the value of γ are shown in Figure 4.5, where it can be seen that for all lattice types there is a clearly defined value of γ at which the energy passes through a global minimum, with the exception being Fe_4C. As the size of the formula unit is not constant for every lattice-type, the systems have been split into four graphs so that the energy per formula unit are comparable.

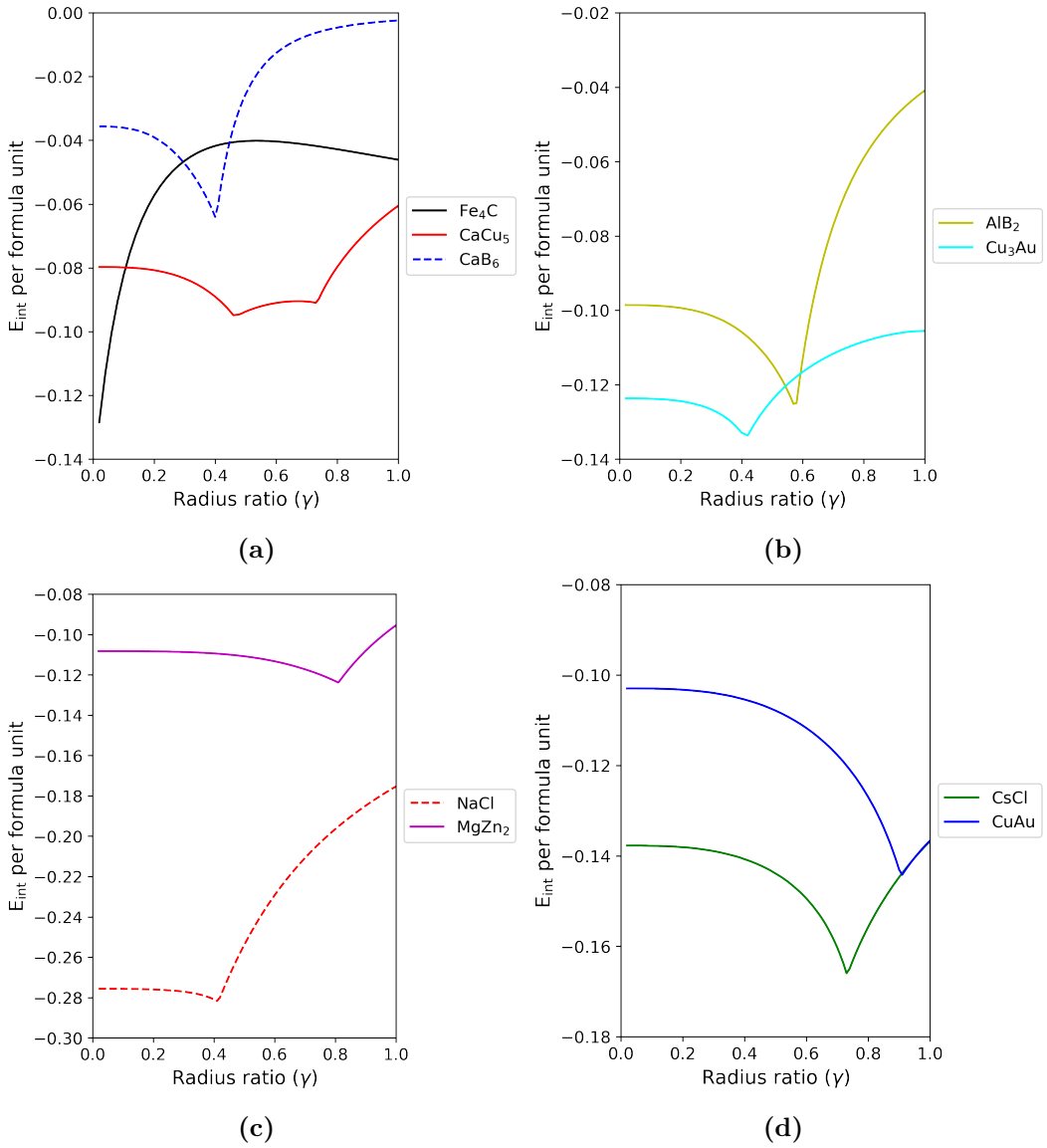

Figure 4.5: *Interaction energy as a function of radius ratio, γ, for all lattice-types, split into number of formula units in the lattice so that energies can be directly compared. (a) The AB_x stoichemietries where x =4,5,6 Fe_4C, $CaCu_5$ and CaB_6 contain 216 unit formula in their lattice structures, (b) AlB_2 and Cu_3 contain 343 unit formulae, (c) NaCl and $MgZn_2$ are composed of 500 unit formula and (d) CsCl and CuAu pack 512 formula unit into their ∼1000 particle lattice structures.*

Figure 4.6 shows the percentage contribution to stability from Coulombic (a) and multipolar (b) interactions. In their percentage forms, all systems can be directly compared. Of the forces contributing to the internal energy, long-range Coulomb interactions between oppositely charged particles are considered to be particularly influential[73, 90] and it is also acknowledged that contributions to U from van der Waals interactions are not, in themselves, sufficient to account for the stability of low-density structures.[90] Therefore only Coulombic

and multipolar interactions contribute to the total interaction energy, hence why the percentage values for each system in Figures 4.6 (a) and (b) sum to 100%. The Coulombic contribution to the total energy is shown in Figure 4.6 (a). We would assume that for each system the Coulombic energy would remain fixed after γ dips below the value which corresponds to the global energy minima as the particles are in contact and so after this unique value of γ the interaction energy is driven by changing multipolar interactions. This is seen in Figure 4.6 (b), which gives the percentage contributions to the total energy that charge-induced multipolar interactions are responsible for. Where s=0, the particles are positioned in the closest packed form for each lattice-type, maximising contributions from these short-range forces. For structures such as Fe_4C lattices, this contribution is a massive $\sim$ 90%, but then just $\sim$ 15% for a NaCl lattice. Comparison of Figure 4.6 (a) and (b) highlights the significance of including multipolar interactions. It can be seen that the true minima for electrostatic energy at unique values of γ in Figure 4.5, only appears when the effects of polarisation are included as, in many cases seen in Figure 4.6, multipolar contributions contribute over 50% to the interaction energy.

NaCl is seen, from Figure 4.5, to be the most stable of the lattices investigated despite its relatively low multipolar contribution. Figure 4.7 shows the effect of changing the smaller particle in a NaCl-type lattice. Below a size ratio value of 0.41, we see all of the larger particles (Cl in this case) are touching each other. Any value of $\gamma > 0.41$ will be met with a constant Coulomb energy. By increasing the size of the smaller particle past $\gamma < 0.41$ distance between the larger spheres will appear as gaps in the lattice structure, ultimately lowering stability as seen in Figure 4.5. As discussed in Chapter 2, uniform distribution of charge on a particle is electrostatically equivalent to a point charge - or having the charge concentrated at a point localised to the centre.

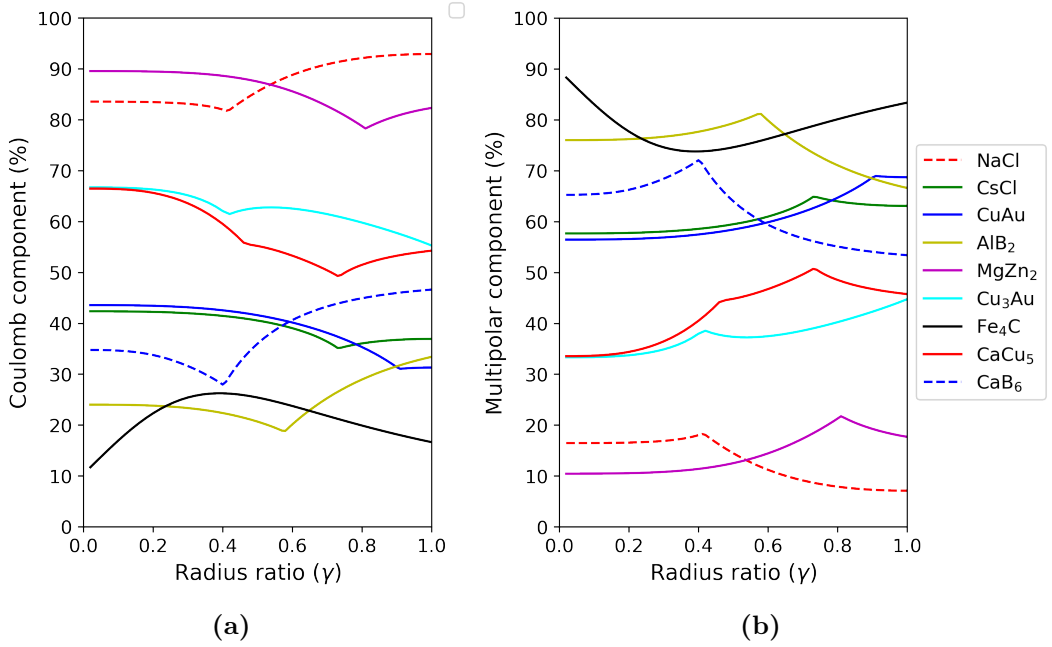

(a) **(b)**

Figure 4.6: *Percentage that (a) Coulombic interactions and (b) Multipolar interactions contribute to total lattice stability for all lattice-types.*

For this NaCl-type lattice, the radius ratio $\gamma = 0.41$ corresponds to the perfect fit of the smaller particles in the octahedral gaps defined by the position of the larger particles. Below this value of γ the small particle is free to move in the gaps and, although the structure could technically keep a negative interaction energy, it is possible that the structure would destabilise. Calculations have, however, shown that here lattices can stabilise from an increase in free-volume entropy. We see in this work that in structures such as NaCl, which has been highlighted here, unique energy minima must be achieved through such interactions as the stabilisation through polarisation is only small.

In other AB-type lattices, there are stronger contributions from multipolar interactions. In the cases of CsCl and CuAu, energy minima for the lattices were found to be $\gamma = 0.73, 0.91$ as seen in Figure 4.5 (d) and match experimental values of $\gamma = 0.74, 1.0$ well. Studies[83, 98] have shown that AB structures can undergo a structural phase change depending on the ionic strength of the suspension medium or the temperature of the system[98]. However, in these studies the switch in structure only occurs when γ is much larger than that for

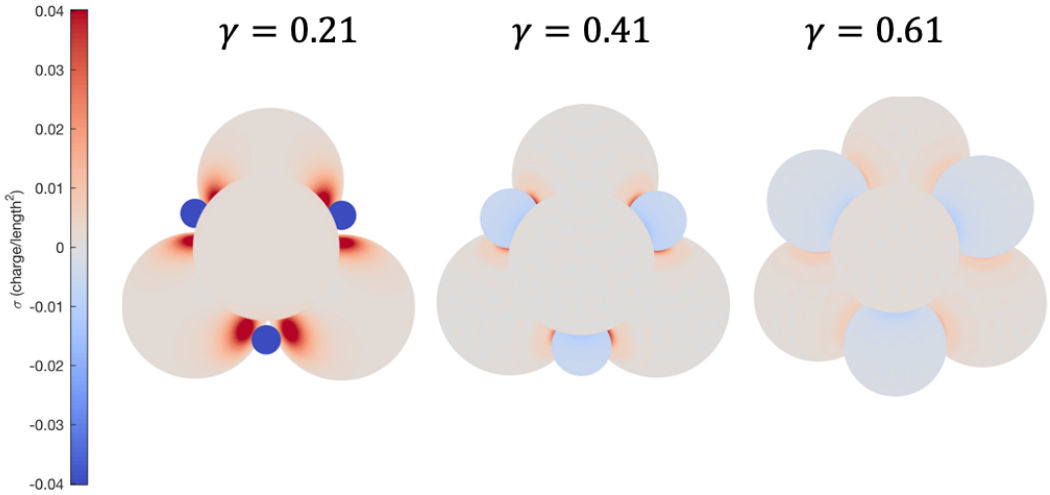

Figure 4.7: *NaCl-type lattice at selected values of the radius ratio, γ, where γ = 0.21, 0.41 and 0.61. The central representation corresponds to the electrostatic energy minimum.*

a highly stable NaCl lattice. As the size ratio approaches 1 in Figure 4.5 (a), we can see that both CsCl and CuAu benefit from advanced stability from many-body contributions and, as the size ratio approaches 1, they are comparable in energy. At this higher packing fraction, switching between the AB-type lattices becomes more likely as it becomes more energetically favourable than at smaller values of γ. However, as the transition requires a large size ratio, it isn't seen in this work where we find that NaCl is always the most stable AB structure in Figure 4.5 and no transition from NaCl-type lattice to either CsCl or CuAu would be seen.

A CaB_6 structure, as seen in Figure 4.5 (a), is dominated by Coulomb interactions and if the structure interacted only by Coulombic forces, the total energy would be positive for all size ratios and the structure would be never be electrostatically stable. It is only through significant multipolar interactions of up to 70% up to the point of $\gamma_{electrostatic}$ that the lattice is stabilised. Such a structure is likely to be electrostatically unstable with a wide range of ligands. The effect of increasing the softness parameter was shown in Figure 4.2 where we see a reduction in multipolar interactions in response to the addition of

ligands. It can therefore be concluded that structures such as CaB_6 would be entropy driven and electrically neutral, as found in the work by Ye *et al.*[97] on CaB_6 nanocrystal superlattices.

After CaB_6, Fe_4C had the highest Coulombic contribution, although unlike its AB_6 comparison it remained negative in sign. Overall, Fe_4C could be seen to be one of the more stable structures - particularly apparent at small size ratios in Figure 4.5a. This is because of the extreme contribution to stability that comes from the multipolar component. Over 90% of the interaction energy is due to attractive multipolar interactions. Although seen experimentally by Shevchenko[73], calculations using electrostatic pair potentials and van der Waal interactions by Ben-Simon *et al.*[99] failed to find a stable structure for a Fe_4C lattice. This work finds that with the significant inclusion of many-body multipolar interactions, a Fe_4C lattice structure is comparable in energy with the other eight structures investigated, highlighting the importance of considering dispersion as a many-body problem.

For $CaCu_5$ there is also evidence of secondary stable minima. The gradual increase of the size of the smaller particle leads to a reduction in the interaction energy as the gaps in the lattice are continuously filled until the global energy minimum is achieved at a value of $\gamma = 0.46$. This value of γ will, uncoincidentally, be consistent with a structure where each particle is in contact with a neighbour of opposite charge. Continuing to increase the size of the smaller particle beyond $\gamma = 0.46$ we would expect to see the energy increase initially. Then at $\gamma = 0.76$ the system reaches a local minimum. It can be seen in Figure 4.5 (a), that the configuration at $\gamma = 0.76$ is where the system sees the peak contribution from multipolar interactions. At about half of the total interaction energy, this is highly significant but remains insufficient to shift the global minima in Figure 4.5 (a) from $\gamma = 0.46$ to 0.73. However, if we computed the multipolar interactions as a sum of the pairwise interactions instead

of a complete many-body treatment, the energy would be overestimated and the multipolar contribution peak at $\gamma = 0.73$ would shift this to be the global minimum. Again highlighting the importance of investigating these systems with many-body theory.

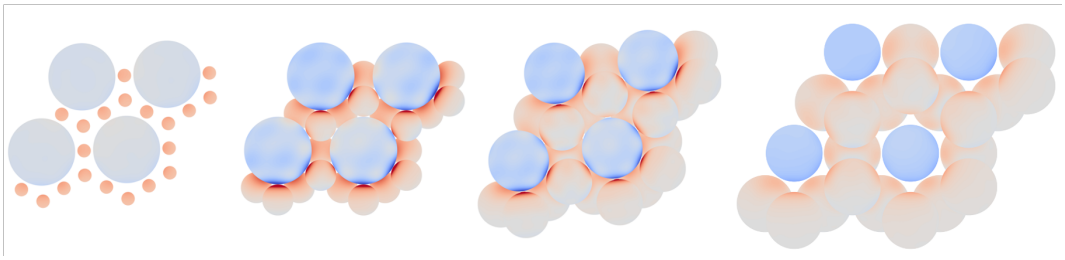

Figure 4.8: *Images of particles in a $CaCu_5$-type lattice for selected values of the radius ratio, γ. Particles representing Ca are shown in blue and have a fixed radius $a = 5$, increased areas of polarisation are visible with regions of darker red and blue at the interface of the oppositely charged particles.*

As can be seen from Figure 4.8, the particles do not always starting from touching one another. This is due to the scaling up of the structures from the unit cells taken from the Materials Project Database. The unit cells themselves are for the atomic unit cell structures. In this work, these same unit cells are used as the coordinates for larger arbitrary particles which can be assigned their own chemical properties. The size of the particles are varied in this work and the distance between the particles is scaled up accordingly. This means that the particles may not be at equilibrium distance for the structures that they are isostructural with. The results concluded using the many-body model in this work cannot be directly transferred to the atomic unit cells as the values for interaction energy are likely to be different. Some structures will be more affected that others, specifically those where the scaling up of the unit cell leaves the particles at a great distance from each other such as $CaCu_5$. This is a possible cause for the difference between $\gamma_{packing}$ and $\gamma_{electrostatic}$ seen in Table 4.1, but still serves to highlight the important role that many-body consideration has in determining an accurate size ratio for a minimum in electrostatic energy.

4.4 Predicting Novel BNSL Structures

As an extension to this study, we predict the stability of novel superlattice structures where there is currently a lack of experimental data thus, γ are compared to those found from hard-sphere modelling[100, 101] as seen in Table 4.2. The five AB-type lattices investigated where CoAs, CrB, γ-CuTi, FeB and α-IrV. For each system, each component particle has been varied in size and plotted as a function of (a) varying the size of particle A and (b) varying the size of particle B, in systems of hard particles (s=0). Both versions were calculated to highlight the difference in data obtained due to the lattice structures.

Table 4.2: Data on lattice types including giving atomic environment, $\gamma_{packing}$ corresponding to the radius ratio at which the maximum packing fraction taken from hard sphere studies and the$\gamma_{electrostatic}$, where calculations have found each lattice type to have a minimum in electrostatic energy. (1) follows the particle which is varied in size while the other remains fixed.

	Atomic Environment[96]	Space Group[96]	$\gamma_{packing}$	$\gamma_{electrostatic}$
Ag_2(1)Se	Ag- Metabidiminished icosahedron	$P2_12_12_1$(19)	0.820[100]	0.76
Ag_2Se(1)	Ag- Bicapped square prism Se– square-face bicapped trigonal prism			0.34
$AuTe_2$(1)	Au- Octahedron	C2/m(12)	0.528[100]	0.32
Au(1)Te_2	Te- Octahedron			0.74
CoAs(1)	Co- Trigonal-face bicapped square antiprism	Pnma(62)	0.414[101]	0.69
Co(1)As	As- Bicapped octahedron			0.57
CrB(1)	Cr- Pentagonal-face capped pentagonal antiprism	Cmcm(63)	0.414[100]	0.64
CrB(1)	B- Tricapped triangular prism			1.00
γ-CuTi(1)	Cu - Octahedron	P4/nmm (129)	0.414[100]	1.00
γ-Cu(1)Ti	Ti - Tricapped triangular prism			0.89
FeB(1)	Fe- Square-face capped hexagonal prism	Pnma(62)	0.414[101]	0.64
Fe(1)B	B- Tricapped triangular prism			0.64
$HgBr_2$(1)	Hg- Octahedron	$Cmc2_1$(36)	0.528[100]	0.15
Hg(1)Br_2	Br- Triangular non-coplanar			0.24
IrV(1)	Ir - Cuboctahedron	Cmmm(65)	1.00[100]	0.85
Ir(1)V	V- Cuboctahedron			0.97

The local environments describe the shape formed by the arrangement of one particle around a central atom of the other particle. Previously, investigation into varying both would not have been as appropriate as in lattices such as NaCl, both Na and Cl possess the same atomic environment and the lattice has a perfectly cubic structure (space group $Fm\bar{3}m$ (225)). This implies that the energies observed would be independent of which particle was varied in size. As can be see in Table 4.2, IrV is the only AB lattice investigated in this work to have identical atomic environments for Ir and V which should imply less variance would be observed with varying both particles. However, it is not a perfectly cubic structure so it is unlikely to provide exactly identical energies. The unit cells of those structures listed in Table 4.2 are shown in Figure 4.9 at a value of γ=1 as the value of $\gamma_{electrostatic}$ was found to differ depending on whether particle A or B was varied.

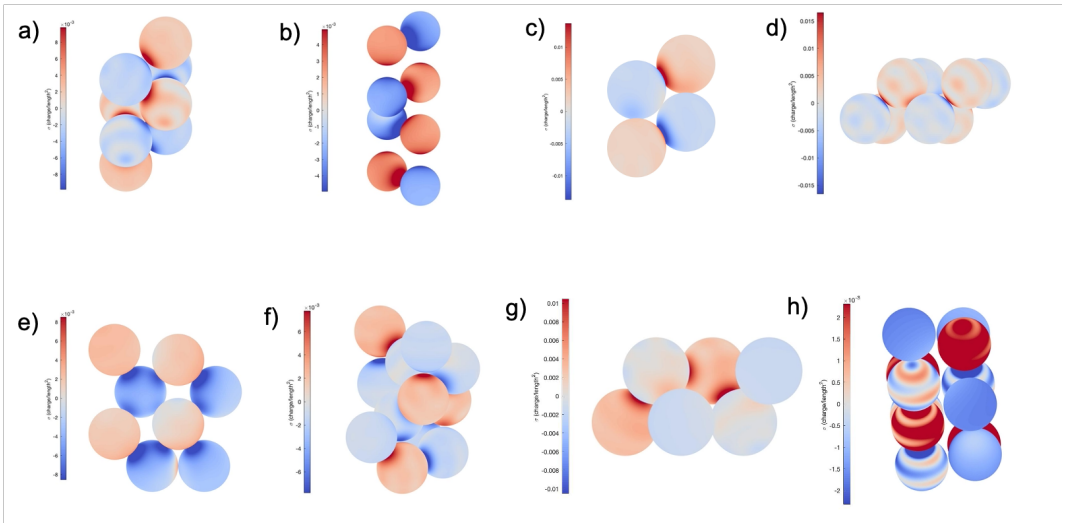

Figure 4.9: *Images showing the BNSL isostructural with a) CoAs, b) CrB, c) γCuTi, d) FeB, e) IrV, f) Ag_2Se, g) $AuTe_2$ and h) $HgBr_2$ at the radius ratio γ=1.*

4.4.1 AB Stoichiometries

There are two general trends observed from the (a) and (b) graphs in Figure 4.10. Firstly, the difference in electrostatic energy observed between the different structures is due to the different space group and atomic environments of the particles within. Closer packed structures will experience stronger interactions and thus a lower interaction energy. Varying one particle in size compared to the other will result in different $\gamma_{electrostatic}$ due to the different atomic environments; meaning in cases like IrV, where the atomic environments are the same, the $\gamma_{electrostatic}$ are similar.

Figures 4.10 (c) and (d) show that up until the electrostatic minima noted in the graphs showing electrostatic energy, (a) and (b), if just the Coulomb contribution was taken into account, that any value of γ up until the $\gamma_{electrostatic}$ would give the same minimum energy. This is due to the fact that when the radius ratio is below $\gamma_{electrostatic}$, each particle is now in contact with a next nearest large particle meaning displacement of their core by any additional decrease in γ is constrained.

Figures 4.10 (e) and (f) show the percentage multipolar contribution to the total electrostatic energy. $\gamma - CuTi$ has a significant contribution regardless of which particle is varied in size due to its symmetrical tetragonal P4/nmm space group as seen in Figure 4.9c. The stabilisation due to polarisation is shown to be dependent on which particle is varied when looking at less symmetrical space groups, as we see that Co(1)As has a higher contribution than CoAs(1) and Fe(1)B experiences less polarisation effects than FeB(1). Both CrB(1) and FeB(1) have multipolar peaks at γ=0.64 corresponding to the minimum electrostatic energy. The energy then begins to gradually increase until it reaches a local minimum at $\gamma = 0.7$, due to there still being a high contribution

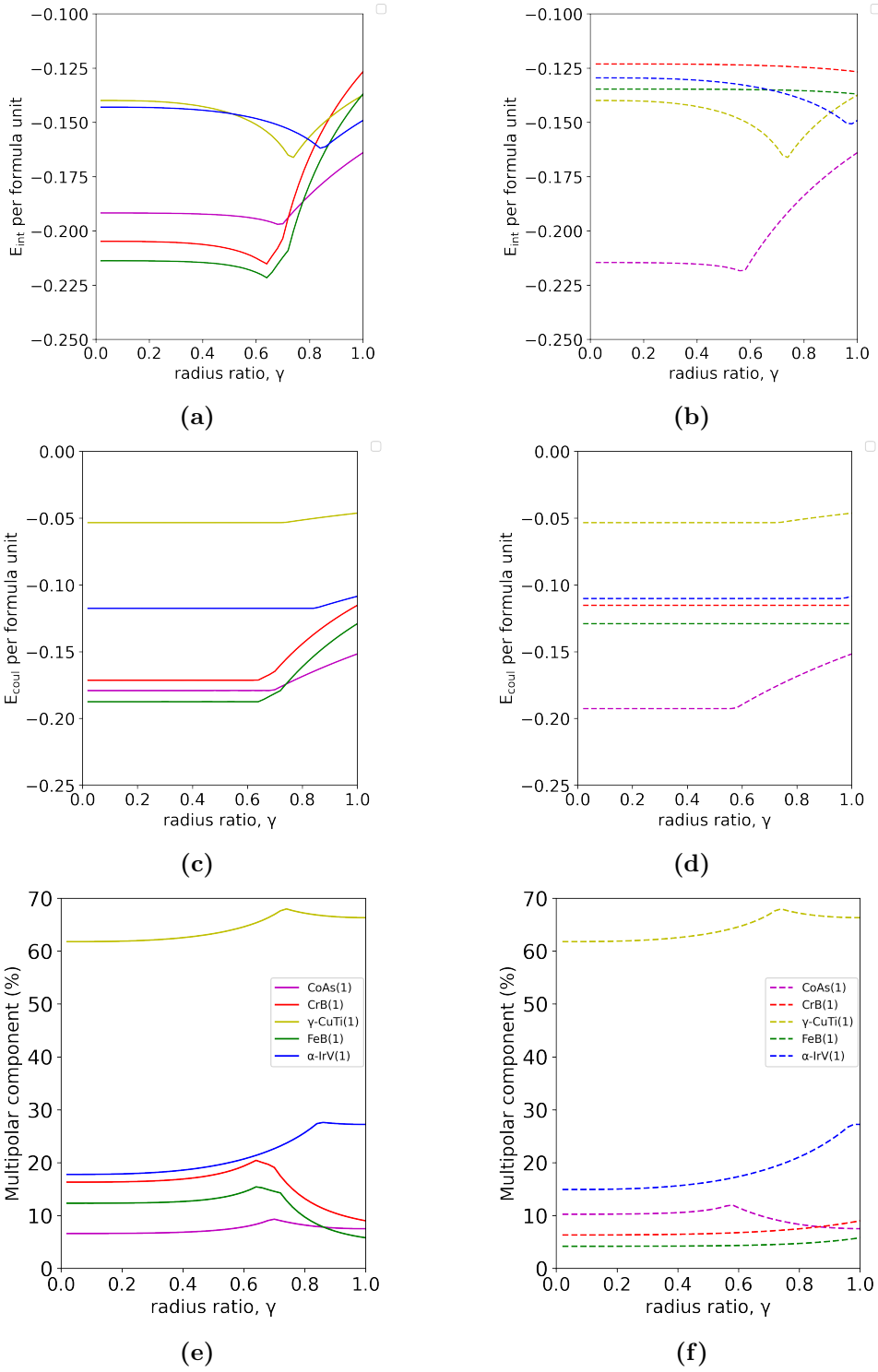

Figure 4.10: *(a),(b) The total (Coulombic+multipolar) interaction energy, (c),(d) individual Coulombic component and (e),(f) the percentage contribution to the total energy from multipolar forces plotted as a function of radius ratio, γ, for s=0. For the solid line graphs, (a),(c),(e),the particle being varied in size from 0.1 to 5 being As(purple), B(red), Ti(yellow), B(green) and V(blue). For dashed graphs (b),(d),(f) the particle being varied in size being Co(purple), Cr(red), Cu(yellow), Fe(green) and Ir(blue).*

from multipolar interactions. Then, past γ=0.7, the polarisation contribution decreases and Coulomb dominates and thus the total energy decreases.

4.4.2 AB_2 Stoichiometries

Three AB_2 systems have also been tested to see if the observations made about AB systems hold true. The three lattice types are Ag_2Se, $AuTe_2$ and $HgBr_2$. Just as the AB systems, these systems have been plotted as a size ratio of both A and of B. Although in actuality, when self assembling into a BNSL the B_2 particles will be the one varying in size, growing in size until they fit inside the voids left in the close-packed structure of the larger A particle.

As a general trend, the AB_2 stoichiometries appear to give a γ value corresponding to less dense packing fractions than the AB systems as can be noted by observing the $\gamma_{electrostatic}$ in Figure 4.11 and more clearly in Table 4.2. Of interest is the vast difference in the two $HgBr_2$ systems. When presented as a function of varying Hg size, the total electrostatic energy drops significantly at small values of γ. Figure 4.11 (b) shows that a gradual increase in the Hg particle leads to a gradual decline in the electrostatic energy until the $\gamma_{electrostatic}$ at 0.24. After this, a sharp increase ensues, where at high size ratios $Hg(1)Br_2$ and $Au(1)Te_2$ share similar electrostatic energy values.

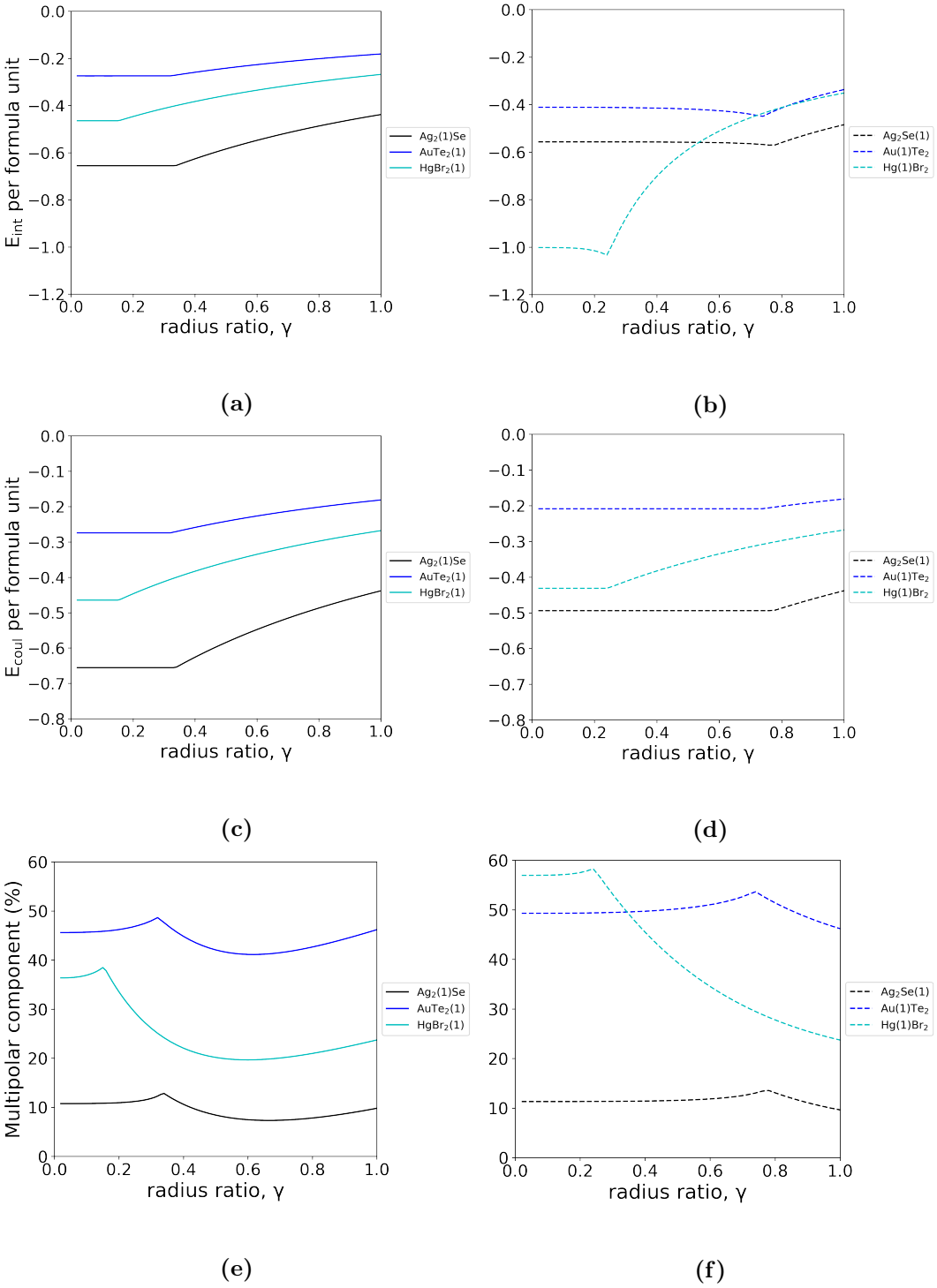

Figure 4.11: *(a),(b) The total (Coulombic+multipolar) interaction energy, (c),(d) individual Coulombic component and (e),(f) the percentage contribution to the total energy from multipolar forces plotted as a function of radius ratio, γ, for s=0. For the solid line graphs, (a),(c),(e),the particle being varied in size being Ag(black), Te(blue) and Br(cyan). For dashed graphs (b),(d),(f) the particle being varied in size being Se(black), Au(blue) and Br(cyan).*

The $AB_2(1)$ systems see larger contributions to the interaction energy from Coulomb interactions as shown in Figure 4.11 (c) and (d). It is unsurprising that in Figure 4.11 (e), $AuTe_2(1)$ has the highest percentage contribution as it is one of the densest binary sphere packings. However, when the graphs are reversed to be as a function of Hg, $Hg(1)Br_2$ experiences a significant stabilisation at γ=0.24 corresponding to a nearly 60 % contribution from multipole effects. As illustrated in Figure 4.12 (a), when Hg particles are assigned to a_1 and are small enough to mimic behaviour of a point charge there are twice as many larger Br, leading to more areas of polarisation than would be present if the Br were the smaller particle.

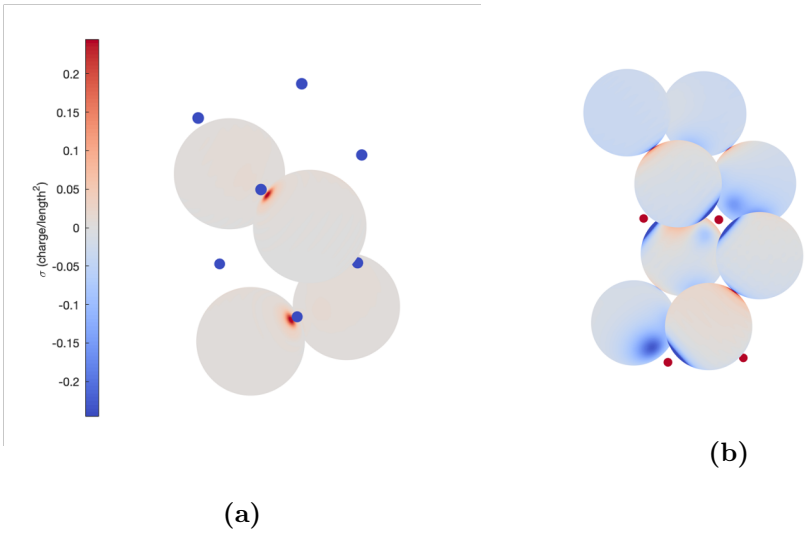

Figure 4.12: *$HgBr_2$ structure for (a) $HgBr_2(1)$ and (b) $Hg(1)Br_2$.*

For Ag_2Se, constant pressure calculations[100] have found that it can transform into $MgCu_2$ at pressures where more symmetric $MgCu_2$ is predicted to be more stable. Thus, Ag_2Se can be looked at as a high-pressure distortion of $MgCu_2$, likely explaining the difference between $\gamma_{electrostatic}$ and $\gamma_{packing}$ for this case.

Generally, there is a significant variance in the values listed in Table 4.2 for $\gamma_{electrostatic}$ obtained from the discussed calculations and for $\gamma_{packing}$ produced from hard-sphere models. In the hard-sphere crystal structure[100] a genetic

algorithm and Monte Carlo simulations are used to find the stability of such structures and if unstable, to identify the relaxed geometry the system would adopt. The identified space groups and atomic environments for the individual lattice structures, as seen in Table 4.2, are not studied in energy calculations. Instead, this work concluds that all AB-lattice structures would collapse to the same basic cubic structure of that of NaCl, as it is of lower overall energy. This is why the $\gamma_{packing}$ for all AB systems in Table 4.2 is 0.414 - the $\gamma_{packing}$ established for a NaCl superlattice. In order to conduct a meaningful comparison between the results discussed in this work and the hard sphere theory, the only other published work on these structures, energy minimisation would need to implemented going forth in order to agree or disagree with the $\gamma_{packing}$ of 0.414.

4.5 Increasing Stability in BNSL Structures by the Addition of Excess Charge

Without entropic contributions, a system which is made up of charged particles, yet remaining overall neutral, will aggregate[16]. In BNSLs, growth that is accompanied by the accumulation of a non-compensated charge has always been considered self-limiting on the basis that it will result in instability and thus hinder the formation of extended lattices[73, 90]. Successful attempts to add small amounts of uncompensated charge to such superlattice structures as those discussed throughout this study would result in BNSLs being composed of constituent particles of different charge magnitudes and increase their scope as devices such as capacitors. Not only this but being able to tune the charge state of constituent nanoparticles would provide another way to vary the BNSL structure by directing the self-assembly process[73].

The key to electrostatic stability will be in balancing the attractive and repulsive interactions. An increase in charge of the system is met with heightened multipolar interactions but also significant Coulomb repulsion which, if it is more dominant, will ultimately lead to the breakdown of the lattice. In order to review the impact of this finding on BNSL stability, the experimental mechanism for the addition of charge to superlattices needs to be understood. The addition of excess charge onto superlattices can be experimentally achieved via a couple of methods. Bartlett *et al.*[98] specify using the concentration of bromide to modify the charges on particles in solution. They use two PMMA particles of similar radii (777 nm and 720 nm), labelled each with differing cationic fluorescent dyes and placed them in a mixed solvent of cycloheptyl bromide and cis-declin. The low polarity solvent induced a small positive surface charge on the PMMA spheres. The bromide ions can either be produced by irradiating the suspension or by introducing a ferromagnetic wire which acts as a site for decomposition of the cycloheptyl bromide. By leaving the length of ferromagnetic wire in the solution for longer, Bartlett was able to increase the concentration of bromide ions to a point where the charge on the particles was negative.

The point at which each particle reached zero charge differed and so the particles could have different magnitudes of charge - meaning that there would be a point where whilst one particle had negative charge, the other remained positive. Charge as a function of the volume fraction as well as a function of contact between solution and metal was investigated and it was found that different structures were found based upon the amount of charge that was present.

Additionally, the choice of ligand can increase the quantity of negative and positive charges. This has been seen by use of carboxyl, trioctylphosphine oxide (TOPO) or dodecylamine ligands[73]. Addition of tetrabutyl ammonium bromide (TBAB) salt has also been investigated as a method for modulating

charge on particles by tuning the range of the electrostatic interactions.

Work by Leunissen *et al.*[102] included the application of an external electric field to *'melt'* the crystals and confirmed that the constituent particles must be charged. A method to measure and locate the charge on the particles is studying the electrophoretic mobility of the nanocrystals in addition with laser Doppler velocimetry[73]. Electrophoresis facilitates the controlled movement of the charged particles in a solvent in the presence of an electric field and laser Doppler velocimetry then uses the Doppler shift of a laser beam to record the velocity. The combination of the two techniques allows for the quantitative calculation of charge on constituent nanoparticles.

In the following calculations the same γ that resulted in a minimum in the electrostatic energy was used. Excess charge was then introduced on the smaller and larger particle in turn, to observe the effect on the electrostatic energy. The dielectric constant remained at 20, an intermediate between materials which are strongly and weakly polarisable. Other studies also used a higher dielectric constant of 15 in their studies[103].

Figure 4.13 shows how the electrostatic interaction energy varies with respect to addition of excess charge in NaCl lattices of varying sizes. Excess charge has been introduced by fixing the amount of charge on the negative particles, while varying the amount of charge on those that are positive. As can be noted from Figure 4.13, energy minima can be identified for lattices that are not net neutral and even when we only consider Coulomb interactions between free charges (dashed lines in Figure 4.13).

By application of Coulomb's law to elements of charge (free and bound) on the surfaces of the particles, it can be seen that a small amount of excess charge will in fact enhance the interactions between each negatively charged

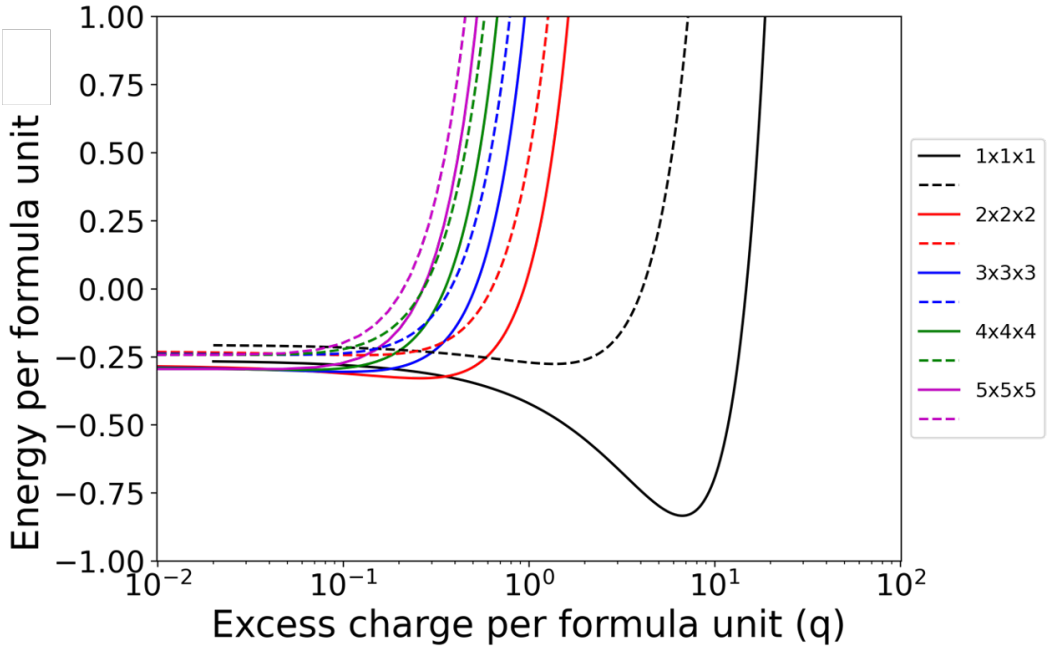

Figure 4.13: *Plot of the electrostatic energy (solid lines) and the contribution from point charge interactions (dashed line) as a function of the excess charge per formula unit for each of the different sized unit cells.*

neighbour and close positively charged neighbours, resulting in the lattice becoming more negative in energy. The inclusion of charge-induced multipolar interactions acts to further enhance this effect. However, this initial gain is short lived as the addition of further uncompensated charge leads to repulsive interactions becoming dominant. The maximum excess charge per particle decreases rapidly as a function of lattice size as seen in Figure 4.13 and is also the case if we consider the absolute excess charge on each size of BNSL. For example, a unit cell (8 particles) achieves an energy minimum with an excess charge of -3.38 and can hold -7.41 uncompensated before the lattice energy switches sign be but when the lattice size increases to 5x5x5 unit cells (1000 particles) these values decrease to -0.0233 and -0.288, respectively.

Chapter 5

Designing a Stable Binary X@C_{60} Superlattice

5.1 Endohedral Fullerenes

The fabrication of both nanoparticles[104–106] and molecular fullerenes[107–109] into functional materials has advanced significantly to a point where some of their unique properties are becoming fully characterised and leading to the development of future electronic, magnetic and optical devices. For fullerenes, these advances have come about because of a dramatic increase in the ability of synthetic techniques to prepare a wide range of endohedral fullerenes, X@C_n, where n usually starts at 60, and for X as a metal, a significant fraction of the periodic table has been accessed.[107–109] Particular attention has been paid to the encapsulation of rare-earth metals as these may have applications in optics and could form new magnetic and electronic materials.[107–109] For example, Gd@C_{82} has been shown to display gate-controlled switching between electronic states in the presence of an external electric field.[110] Recent work has also demonstrated that other metals, such as encapsulated lithium, Li@C_{60}, have the potential to act as molecular switches,[111, 112] and calculations on Ca@C_{60} have identified internal motion on the part of the metal atom

as a mechanism for switching charge polarisation on the cage[113].

Parallel to work on fullerenes in Chapter 3, has been the fabrication of nanoparticle crystals with compositions varying from polymers through semiconductors to metal-centred particles,[104–106] and where self-assembly frequently leads to the formation of ordered lattices with regular structures resembling those adopted by crystalline atomic materials, e.g. NaCl, CsCl, AlB_2 etc. as seen in Chapter 4. Depending on the nature of the particles used in the fabrication process, the lattices have been identified as materials which could have a range of unique properties.[104–106]

The purpose of this work is to use the recent development in many-body electrostatic theory to explore some of the known characteristics of endohedral fullerenes with a view to determining if they could form new and novel nanolattice structures[31]. As a consequence, some of the optical and electrical properties previously identified for fullerenes[110, 111] could be incorporated into new materials fabricated into the regular lattice structures known to be adopted by nanoparticles[104–106].

The literature on nanoparticle lattices[104–106] shows there to be a certain degree of ambiguity in the nature of the constituent particles: they are often charged in isolation, but there is uncertainty as to whether or not any charge remains in the lattice once the particles have assembled. Additionally, there is often some dispersion in particle size; and the particles are frequently decorated with ligands which could influence both van der Waals interactions and the dielectric constant of, for example, a particle that has a metallic core. In contrast, much of this uncertainty disappears with fullerenes, C_n: their exact size is known and shows no dispersion for a fixed value of n;[5] a value for the dielectric constant has been published;[114] an accurate van der Waals potential is available;[5, 58, 115] and finally, whilst the particles are overall neutral,

a charge of either sign can be induced on the cage through the judicious selection of X, the encapsulated species in X@C_n.[107–109].Thus, interacting particles will experience a combination of electrostatic and van der Waals interactions that can be fully characterised to define a lattice structure and a lattice energy. Several stable endohedral fullerene complexes involving Li@C_{60} have already been prepared,[116–118] and of these, Li^+@C_{60}.$SbCl_6^-$,[116] and Li^+@C_{60}.PF_6^-, [117] are probably the most fully characterised. The stability of such complexes relies on electron transfer between the two constituents leading to the formation of an ionic solid, and attempts to form similar complexes involving other metallofullerenes have not been successful[109]. In part, this problem appears due to the extreme reactivity of X@C_{60} fullerenes;[109] however, samples of crystalline C_{60} metallofullerenes have been prepared through functionalisation, which has been shown to increase the HOMO-LUMO gap thereby reducing reactivity[119]. Issues with the reactivity of endohedral C_{60} metallofullerenes would clearly present difficulties with fabricating the types of lattices envisaged here; however, C_{60} is the most fully characterised of the fullerenes and those features of the molecule are used to underpin the calculations.

The ideas discussed here are equally applicable to any quasi-spherical fullerene, such as C_{84}, and recent work on electrostatic interactions between spheroids offers the potential to extend this type of study to ellipsoid structures, such as C_{70}.[120]

In the analysis that follows, each endohedral fullerene in the form of X@C_{60} remains overall neutral, but because many of the interactions could involve fractional amounts of charge, it is possible to explore the participation of metallofullerenes that may not be susceptible to reactivity or the donation or acceptance of integer numbers of electrons.

5.2 Computational Parameters

The van der Waals interactions between C_{60} fullerene molecules were described using two- and three-body potentials given by Pacheco and Prates-Ramalho (PPR), discussed in Chapter 2[5]. For C_{84} fullerenes, a two-body van der Waals potential due to Girifalco has been used[9] together with parameters taken from Micali *et al.*,[6] which are summarised in Table 5.1.

Table 5.1: Parameters used to describe van der Waals interactions: PPR potential [5] for C_{60}, and the Girifalco Potential[6] for C_{84}.

C_{60} Parameters	
Radius	0.5025 nm
Dielectric Constant	3.46
C_{84} Parameters	
d	0.8401 nm
α	5.356 $\times 10^{-}14$ erg
β	3.542 $\times 10^{-}10$ erg
R_0	1.1357 nm
$-\varepsilon/K_B$	4081.5 K
Dielectric Constant	4.24

Density functional theory was used to optimise the geometry of endohedral fullerenes using the wB97X-D/6-311G* level of theory, as provided by the Q-Chem 5.0 quantum chemistry software package.[121] For the prediction of partial charges, the density-derived electrostatic and chemical (DDEC) method [122–124] has been selected as it reproduces reference ion states and provides an approximately spherical atomic electron distribution, thus combining the advantages of both the Hirshfeld [125] and iterative stockholder atom [126] methods.

Much like in Chapter 4, the size of all different lattice types were investigated as a function of interaction energy to ensure energy convergence of the system. Lattices of 1000 particles can continue to be used as Figure 5.1 indicates, we see a plateau of energy as the lattice increases in size past this point.

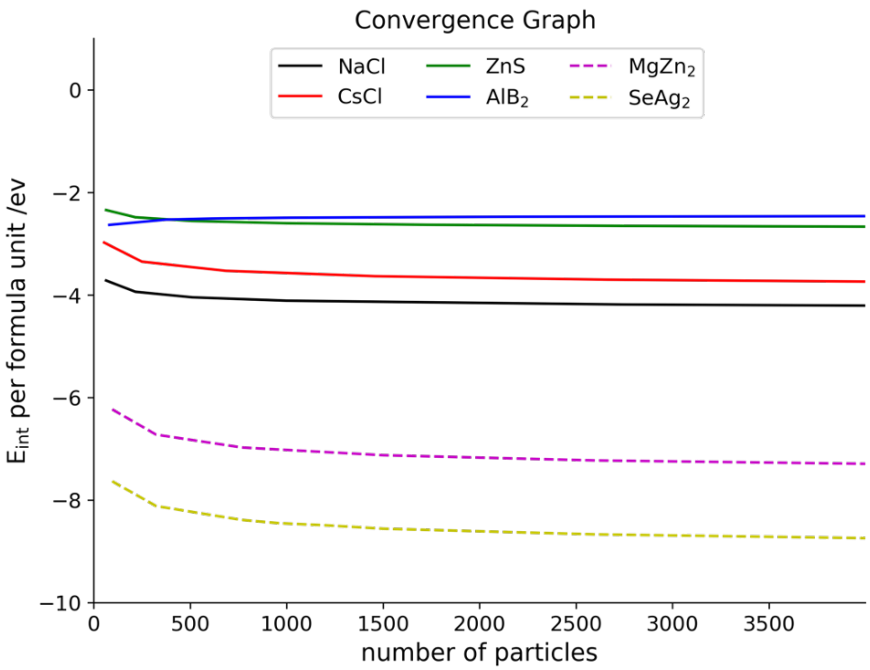

Figure 5.1: *Interaction energy per formula unit in eV for 6 different superlattice structures made up of endohedral fullerenes, shown as a function of lattice size. We can confer that systems with 1000 or more particles can be used.*

Five of the six systems, namely NaCl, CsCl, AlB_2, $MgZn_2$ and Ag_2Se have been investigated in this work previously as BNSL structures. In addition to these ZnS, Zincblende with the space group $F\bar{4}3m$ (216) was included and presents a very similar energy convergence to AlB_2. It is interesting to note from Figure 5.1 that incorporating properties of fullerenes into the constituent particles does not influence the convergence of the energy profile.

5.3 Analysis of Lattice Types

The energetics of lattices consisting of two frequently observed binary nanoparticle stoichiometries,[104–106] AB and AB_2, have been explored as a function of the ratio of charge residing on cages associated with separate A and B endohedral $X@C_{60}$ fullerenes (how charge appears on the fullerenes is the subject of a detailed discussion below). The total interaction energy of each lattice type has been determined from calculations combining van der Waals (vdW), Coulomb and charge induced multipolar interactions. The vdW interactions

are described following the work of Doye, Wales and co-workers,[58, 115] who have demonstrated that expressions due to Pacheco and Prates-Ramalho[5] can be used to determine minimum energy structures for large clusters of C_{60} molecules. The electrostatic contributions to the stability of collections of endohedral fullerene cages have been calculated using a recently developed theory of many-body electrostatic interactions, described in Chapter 2,[34] which provides quantitatively accurate descriptions of the large number of Coulomb and charge-induced multipole interactions that may be present in an ordered lattice of charged particles. Batista *et al.*[127] have previously recognised the significance of non additive interactions in the treatment of nanoparticle structures.

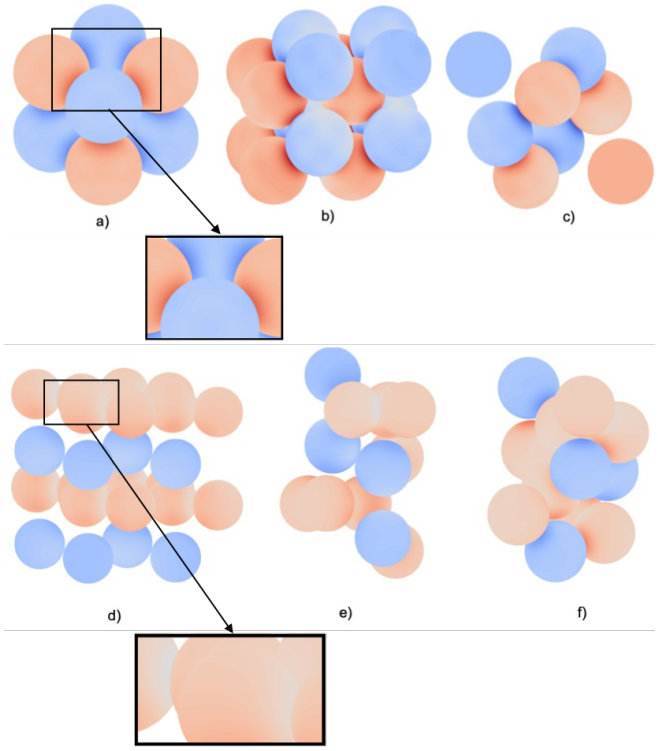

Figure 5.2: *Section of each lattice type: a) NaCl; b) CsCl; c) ZnS; d) AlB_2; e) $MgZn_2$; f) $SeAg_2$. Shading on each particle depicts the calculated surface charge as being either negative (blue) or positive (red). Regions of more intense colouration correspond to enhanced charge due to the polarisation of bound charge and are shown in the enlarged images*

Figure 5.2 shows small sections of each of the lattice types examined. In addition to the obvious colour difference between negatively and positively charged particles, there are also regions of more intense colour showing enhanced charge

due to polarisation. This is particularly evident in, for example, structure b where there is a large contribution from charge-induced polarisation (illustrated in the expanded image and see Figure 5.2). Also evident in some of the AB_2 structures, for example, (d) and (e), is the presence of negative charge (shown in blue) between two adjacent positively charged particles (shown as red). This latter effect is highlighted in the expanded image and has been discussed previously,[24, 128] where it has been shown that such mutual polarisation can ultimately lead to like-charge attraction.

The formation of a binary lattice requires there to be two types of particle, which is not immediately obvious in the case of fullerenes; however, calculations show that changes in the nature of the encapsulated species can utilise electron affinity to create a positive or negative charge on the former. Table 5.2 summarises the results of calculations showing the consequences of introducing different atoms into the C_{60} cage[129–132]. The presence of a metal atom, such as calcium or lithium, generally has the effect of ionising the atom and at the same time adding electron density to the cage, and resident metals and metal complexes have been classified as being either mono, di, or trivalent[107–109] depending on the number of electrons assumed to be transferred to the cage.

Table 5.2: Summary of calculated charge populations on the C_{60} cage following the encapsulation of metal and halogen atoms. The numbers quoted are dependent on the methods used to calculate the populations, details of which can be found in the cited articles. Values in bold indicate results produced in this work.

Endohedral species	Calculated charge on the cage (e)
Mg	-0.10[130]
Na	-0.88[130]
K	-0.95[130]
Al	-0.89[130]
La	-1.07[130]
Lr	-0.77[131]
Au-Au_6	-0.1 to -2.0[132]
Ca	-1.27[130]; -1.33; **-1.44**
Li	-0.68[129]; -0.91[130]; -0.55[131]; **-0.94**
F	0.4[129]; **0.38**;
Cl	**0.58**;

The wide range of metal atoms that have been (or could be) encapsulated in fullerenes means that, for the examples shown in Table 5.2, the calculated charge on the cage can vary between -0.1 e and -2.0 e[129–132]. In contrast, the introduction of a fluorine or chlorine atom removes electron density from the cage and adds negative charge to the endohedral F or Cl atom[129]. Since chlorine has the higher atomic electron affinity, the calculated charge on a cage induced by its presence is an upper limit to what can be achieved with a single atom. Experimental confirmation of the anticipated charge transfer when metal atoms are encapsulated in fullerenes, can be seen from studies of $Li@C_{60}$[133, 134], where it has been shown that in isolation, $Li@C_{60}$ takes the form $Li^{+}C@_{60}^{-}$. However, in the condensed phase, the endohedral complex has been shown to form a dimer $Li@C_{60}$ - $Li@C_{60}$[133, 134].

The limitations discussed above regarding the amount of positive or negative charge that can be transferred to a fullerene cage could be relaxed with the inclusion of species more complex than simple atoms. The presence of both Sc_3N and Ti_3C_3 in a fullerene are thought to result in the transfer of up to 6 electrons to the cage;[135, 136] likewise, recent calculations have shown that a series of superhalogens, including AlF_4, MgF_3 and LiF_2,[137] together with $PtCl_9$ and Pt_2Cl_9,[138] and Mg_3F_7[139] all have electron affinities higher than that of chlorine, and in some cases, calculations have already shown these molecules to be capable of removing electron density from the C_{60} cage.[135, 137].

Finally, experiment and theory have identified molecules capable of forming stable dianions with first and second electron affinities above that of the single electron affinity of chlorine. These species include ZrF_6[140] and $B_{12}(CN)_{12}$,[141–143] which can form stable dianions when the second electron becomes trapped behind a Coulomb barrier; as such, their inclusion in an endohedral fullerene, could result in the cage losing up to 2 electrons and acquiring a charge of +2. Many of these molecular examples would obviously require

accommodation in fullerenes larger than C_{60};[144] however, they do offer the possibility for generating a wider range of lattice structures.

A large number of metal-containing endohedral fullerenes that have, to date, been synthesised are readily available[107–109]. What is less obvious are routes to the synthesis of the required counter ion, and although recent experiments have identified the formation of stable $F@C_{60}$,[145] that aspect of the work will require further experimental investigation. It is encouraging to note, however, that thermally stable quantities of the non-metallic endohedral fullerenes $N@C_{60}$ and $P@C_{60}$ have been prepared, although calculations show there to be no electron transfer from or to the cage[146]. What all of the examples given in Table 5.2 do demonstrate, is that there is some flexibility in the amount of charge, either negative or positive, that could be induced to reside on the surface of a fullerene cage. For the purposes of the theory, it is assumed, to start, that in the examples discussed below the cage has a uniform distribution of charge; this in turn implies that X in $X@C_{60}$ resides at the centre of the cage, which is not always necessarily the case.[107–109, 116–118, 129–132]

5.4 Stability of Structures as a Function of Charge Ratio

In principle each AB pair should experience three separate electrostatic interactions, which are: i) the charged core of A interacting with the charged core of B; ii) an interaction between the charged cores and the charged cages; and iii) an interaction between the charged cage of A and the charged cage of B as can be seen in Figure 5.3. However, a range of experimental and theoretical studies have shown that fullerene molecules act as Faraday cages,[147–154] which means that entities (other cores and cages) external to a given cage are shielded from any charge contained within the cage, i.e. the metal or halogen

core. Therefore, electrostatic interactions in AB and AB_2 systems will be dominated by iii, namely interactions between the charges on each A and B cage. Thus, each lattice with, for example, an AB pair in the form of $A@C_{60}^{q+}.B@C_{60}^{q-}$, is treated as a collection of charged, dielectric spheres, for which theory is very well established.[24, 34]

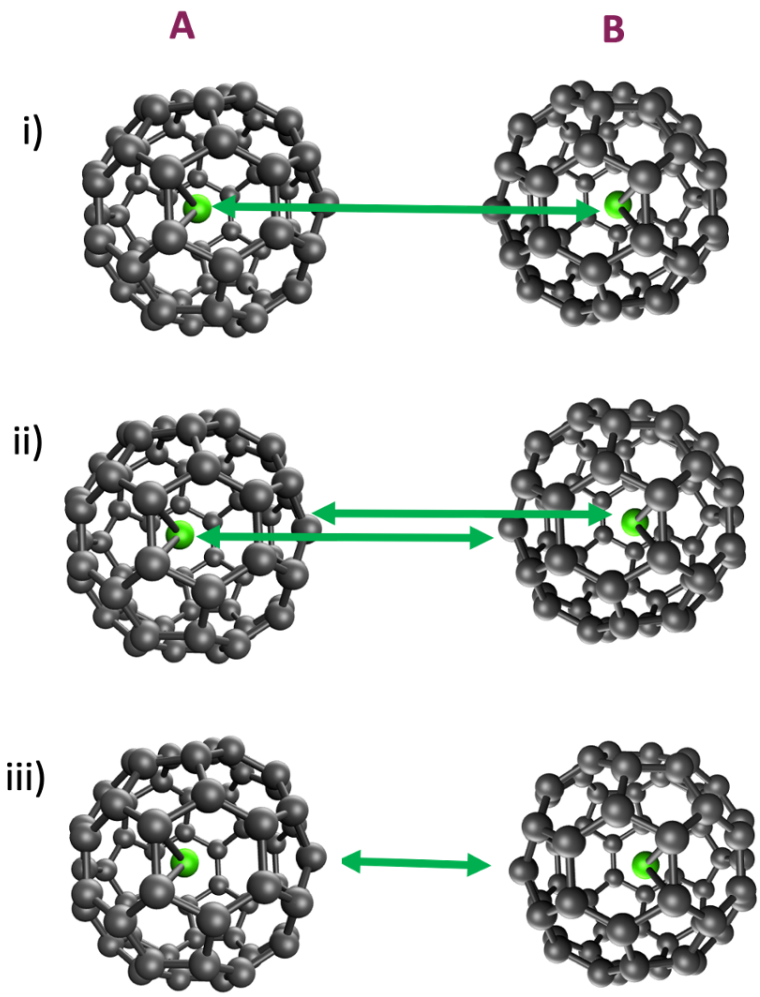

Figure 5.3: *Three possible interactions between endohedral fullerenes i) the charged core of A interacting with the charged core of B; ii) an interaction between the charged cores and the charged cages; and iii) an interaction between the charged cage of A and the charged cage of B. Figures from publication by Halstead[8].*

Two lattice stoichiometries have been the subject of this study, and these are AB and AB_2. For AB systems the calculations discussed below have focussed on nominal charges of q_A = -1 e and q_B = +1 e on the cage, but with the negative charge allowed to vary by ± 0.5 e; thus, reflecting the fact that an exact equal and opposite match of charge on the cages will probably not be

possible. For AB_2 systems the nominal charges are q_A = -2 e and q_B = +1 e, but with a negative charge variation of ± 1.0 e. For AB combinations where the absolute charge on each cage is different to what is considered here, the Coulomb energies quoted below can be scaled using the product $q_A q_B$.[155] It should again be emphasised that each $X@C_{60}$ and each final nanolattice remains charge neutral. An example of a potential lattice would be an AB structure consisting of unit cells containing $Li@C_{60}$ paired with $Cl@C_{60}$.

Lattice stabilities have been calculated as a function of the charge ratios q_A/q_B and $q_A/2q_B$, respectively. The intention here is to explore a range of lattice types to see which might be best suited to form a stable crystalline structure. For AB structures, initial calculations were undertaken on the rock salt cubic lattice, which experiment has identified as stable for both pure C_{60} above 249K[156] and for endohedral fullerenes of the form $Li^+@C_{60}(Y)$, where Y is PF_6^- or ClO_4^- [116–118] (although Table 5.2 shows the cage in $Li@C_{60}$ is calculated to be negatively charged,[129–131] the cage in $Li^+@C_{60}$ is predicted to carry a charge of +0.1e[130]).

5.4.1 AB Stoichiometries

Figure 5.4(a) shows the results of calculations on a lattice composed of negatively and positively charged C_{60} cages arranged in the form of an NaCl face-centered cubic (FCC) crystal. What is immediately obvious from the calculated total energy is that this lattice is very stable over a wide range in the charge ratio, with each of the separate interactions making a contribution to overall stability. For this example, the dominant interactions are Coulomb and van der Waals, with the latter remaining constant across the charge ratio range as it is not sensitive to charge. Where the vdW interaction becomes particularly significant for stabilising the lattice is at those charge ratios where the Coulomb energy becomes positive; also, at these ratios, the contribution

from charge-induced interactions, which although small, is always negative and therefore helps to extend the range of charge over which the lattice remains stable.

Figure 5.4(b) shows the result of calculations on an CsCl body-centered cubic lattice composed of $X@C_{60}$ molecules. Across the charge ratio shown, the lattice is almost as stable as that seen for the FCC lattice; however, in contrast to the FCC lattice, the Coulomb contribution is comparatively small and it is the van der Waals and charge-induced interactions that make significant contributions to overall stability. What is significant for both lattice types is that stability is not restricted to charge ratios close to one; thus, allowing mismatches of the type seen in Table 5.2 to still result in a stable lattice. Finally, for the AB lattices, Figure 5.4(c) shows results for a ZnS lattice, which at charge ratios close to 1, has dominant contributions from Coulomb and vdW interactions, but is less stable than the other two lattice types.

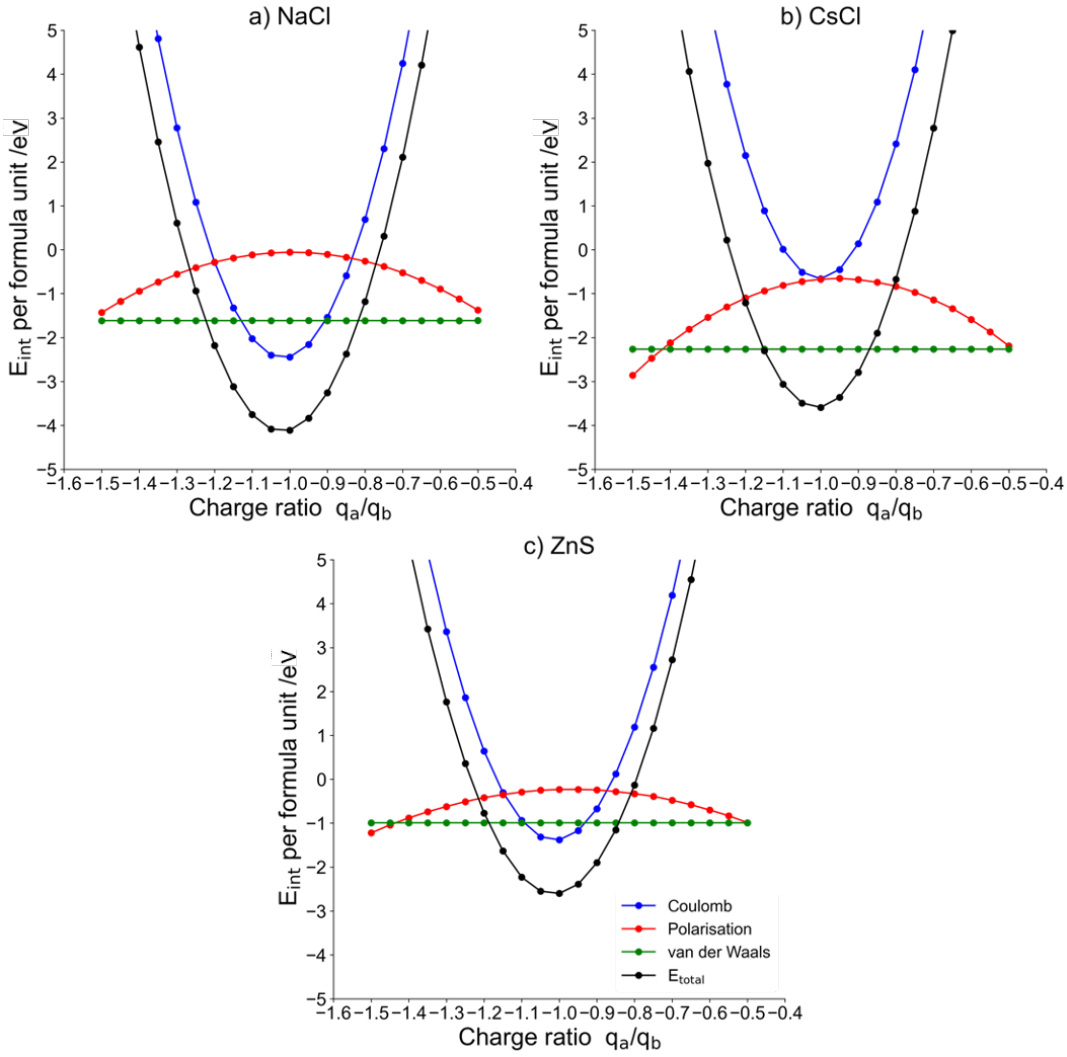

Figure 5.4: *Individual contributions to the total energy per formula unit for lattice structures of the type a) NaCl; b) CsCl; and c) ZnS, each consisting of equal numbers of positively and negatively charged $X@C_{60}$ fullerene cages*

5.4.2 AB_2 Stoichiometries

Figure 5.5 show the results of calculations on three AB_2 lattice types, namely, AlB_2 $MgZn_2$ and Ag_2Se. For the AlB_2 lattice, there is very little stability to be gained from Coulomb interactions away from $q_A/q_{2B} \sim 1$, and it is only the presence of vdW and polarisation interactions that extend stability over what is still a narrow range of charge ratios. In contrast, the stabilities of both the $MgZn_2$ and Ag_2Se fullerene lattices rely almost entirely on Coulomb interactions, which, again, over a very narrow charge ratio, renders both lattices to be far more stable than any of those examined thus far.

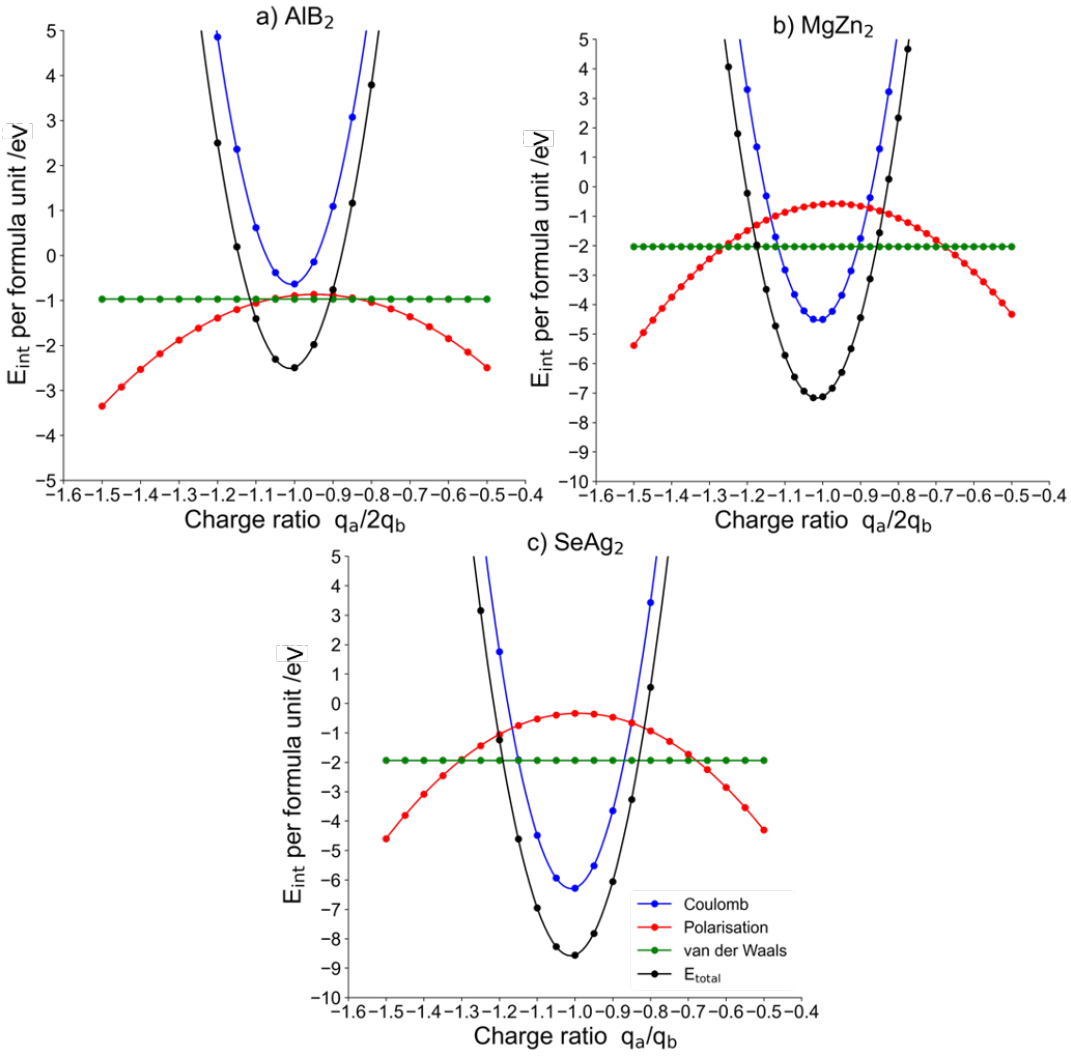

Figure 5.5: *Energy per formula unit for lattice structures of the type a) AlB_2; b) $MgZn_2$; and c) $SeAg_2$, each consisting of two positively and one negatively charged $X@C_{60}$ fullerene cage*

Table 5.3 summarises data on the charge range over which each of the lattice types is calculated to be stable, which given that exact equal and opposite charges on the $X@C_{60}$ constituents of a lattice may not be possible, increases the opportunity to form a stable structure. Taking as a guide to stability, existing data on the neutral C_{60} FCC lattice, where just vdW interactions are present, then a CsCl lattice could be 1.5 to 2 times more stable than its neutral counterpart. However, if it becomes possible to closely match the positively and negatively charged components, then a $SeAg_2$-type lattice looks to be extremely stable.

Table 5.3: Total interaction energies (in eV per unit formula) for endohedral fullerenes arranged in the lattice types NaCl, CsCl, ZnS, AlB_2, $MgZn_2$, $SeAg_2$ at charge ratios between -0.5 and -1.5. Negative interaction energies are shown in bold to highlight the stable structures

q_A/q_B	-1.5	-1.4	-1.3	-1.2	-1.1	-1.0	-0.9	-0.8	-0.7	-0.6	-0.5
System	**Interaction Energies in eV per Formula Unit**										
NaCl	9.83	4.61	0.61	**-2.18**	**-3.75**	**-4.11**	**-3.25**	**-1.18**	2.11	6.11	12.33
CsCl	12.30	6.47	1.97	**-1.21**	**-3.06**	**-3.59**	**-2.79**	**-0.67**	2.77	7.54	13.63
ZnS	10.04	5.36	1.76	**-0.77**	**-2.23**	**-2.60**	**-1.90**	**-0.13**	2.72	6.65	12.54
AlB_2	31.15	18.78	9.23	2.50	**-1.41**	**-2.49**	**-0.76**	3.79	11.17	21.37	34.38
$MgZn_2$	40.83	23.06	9.37	**-0.22**	**-5.72**	**-7.12**	**-4.44**	2.34	13.21	28.17	47.22
$SeAg_2$	40.77	22.68	8.71	**-1.16**	**-6.91**	**-8.55**	**-6.08**	0.50	11.19	25.99	44.90

Figure 5.6 summarises the contribution the three separate interactions, Coulomb, charge-induced, and vdW make to the overall stability of each lattice type when the charge ratio, q_A/q_B, is one. There does not appear to be a unique prescription for creating a lattice that is both strongly bound and stable across a wide charge ratio. In three examples, a large Coulomb contribution gives a lattice that, within its class, is strongly bound, but at the same time, vdW and charge-induced interactions could have a significant role in the fabrication of a stable endohedral fullerene lattice. The total energies calculated for all the AB and AB_2 structures are very clearly >> kT, which means that they should remain stable at room temperature and most likely under the operating conditions of any application.

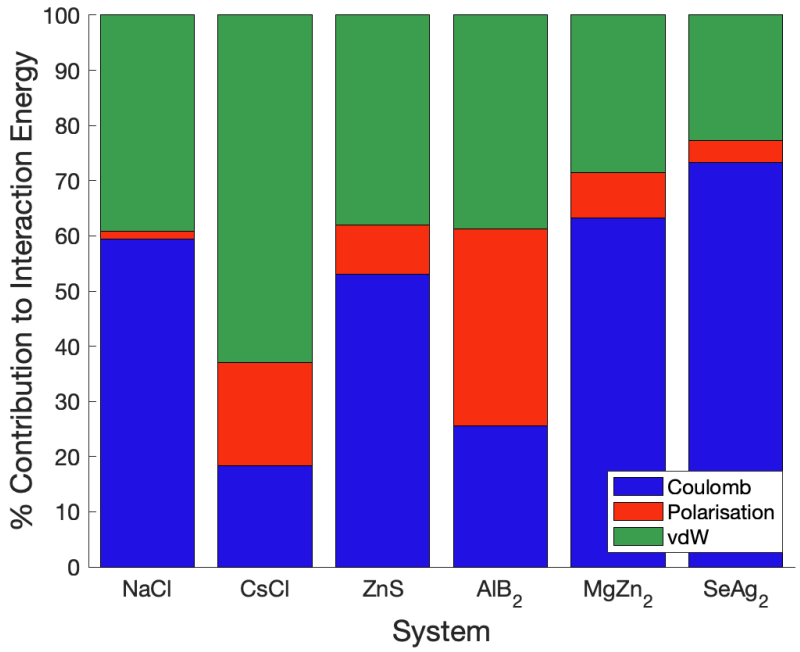

Figure 5.6: *For each AB and AB_2 lattice type where the charge ratio is one, the percentage contribution to the total energy is shown for each of the following interactions: Coulombic (blue); charge-induced (red); and vdW (green)*

Since there is the potential for generating endohedral fullerenes with charges outside the range considered above for AB structures, two further calculations have been undertaken. Figure 5.7 examines how, for the situation where q_a=-q_b in X@C_{60}, the stability of NaCl and CsCl lattices varies as the charge q on each cage increase from 0 to 2. As can be seen, the stability of both lattice

types increases significantly beyond q = 1.0; however, there is also an interesting switch in stability at q ∼ 0.7 between the FCC lattice of NaCl and the cubic lattice of CsCl, which clearly arises when the large contribution from van der Waals and charge-induced interactions to the stability of the CsCl lattice is superseded by the higher Coulomb contribution to the NaCl lattice that varies as q^2 and can be seen in Figures 5.4(a) and 5.6. The fact that fractional charges, less than 1 e, on a pair of endohedral fullerenes in an AB structure will form a stable lattice, could help to reduce the possibility of reactivity.[109]

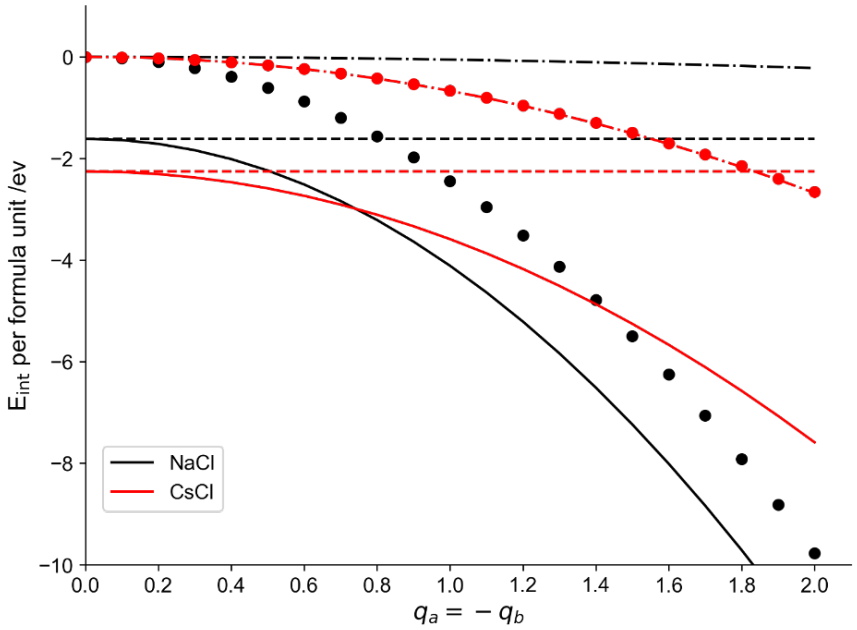

Figure 5.7: *Variation in the stability of NaCl and CsCl lattice types for the situation where $q_a = q_b$, and the charge q on each cage is increased from 0 to 2. The various interactions are shown as follows: van der Waals - dashed lines; polarisation - dot-dashed lines; Coulomb – dotted lines; total energy – solid lines. For CsCl the contributions from Coulomb and polarisation interactions are almost identical*

The calculated results given in Figure 5.7 predict that at zero charge on the particles, the CsCl BCC lattice structure should be more stable than that of the NaCl FCC lattice. If the BCC lattice could be viewed as two interlocking simple cubic lattices, then this result would be consistent with the simple cubic structure observed for pure C_{60} at low temperatures[156].

5.5 Charged Structures with Neutral Layers

Experiments on multiply-charged clusters, $(C_{60})_n^{q+}$[3], would suggest that a single-component X@C_{60} nanolattice, where each endohedral fullerene cage carries a charge of the same sign will not be stable, but that a lattice of the form $(X@C_{60})_n(C_{60})_m$ which is interspersed with non-endohedral fullerenes with m > n might be. Some examples of the superlattice structures investigated above were taken and explored with alternating layers of charged endohedral fullerenes and neutral, hollow C_{60} molecules. The interaction energy of different system sizes was explored as a function of the magnitude of the charge on the X@C_{60}.

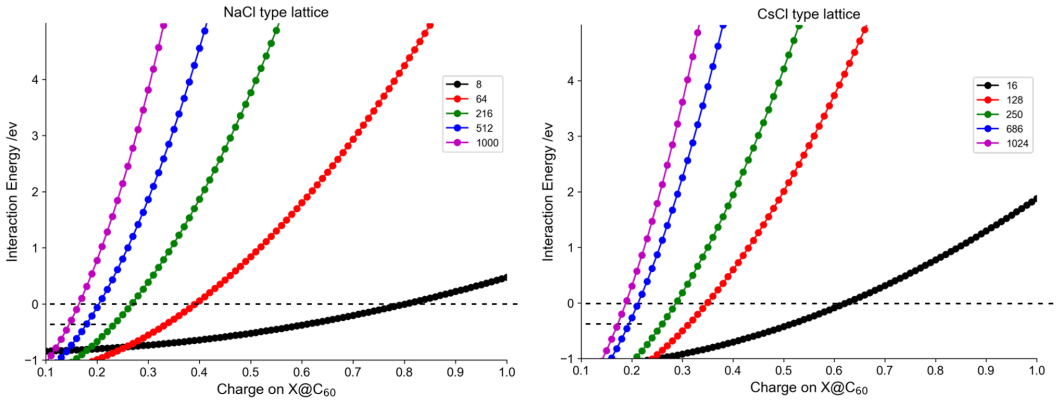

(a) **(b)**

Figure 5.8: *$X@(C_{60})_n(C_{60})_m$ BNSL structures as a function of charge on the $X@C_{60}$ for (a) NaCl-type lattice and (b) CsCl-type lattice. The dashed line is where the interaction energy is 0 eV.*

In the AB systems seen in Figure 5.8 there is one neutral C_{60} to each positively charged X@C_{60}. Thus far, NaCl has been seen to be a highly stable structure and this remains the case here where we can see that in a single unit cell, as shown by the black line on Figure 5.8(a), each endohedral cage can have a charge of almost +1 with the cell remaining stable. We see this trend regress with respect to size of the structure as with an increasing number of endohedral fullerene cages being charged, significant uncompensated charge is added

to the lattice overall. The interaction energy profile for an 16 particle CsCl has a much steeper gradient yet can still hold a charge of ~ 0.8 eV in each charged particle whilst remaining net stable. For the 1000 particle lattices, at least a charge of ~ 0.15 eV can be added to each endohedral fullerene cage and the system will remain stable. This presents the prospect that either Mg or Au could be suitable encapsulated metals in such $X@(C_{60})_n(C_{60})_m$ structures as Table 5.2 shows that these both induce a charge of -0.1 eV on the fullerene cage.

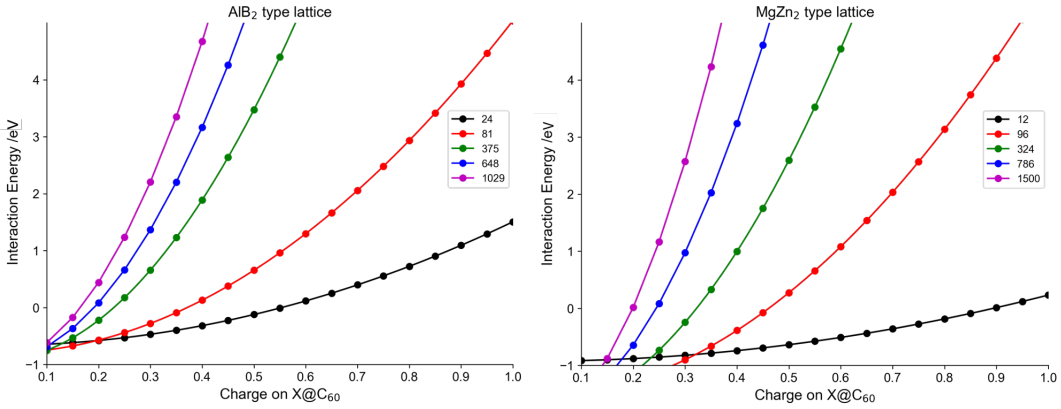

(a) **(b)**

Figure 5.9: *$X@C_{60})_n(C_{60})_m$ BNSL structures as a function of charge on the $X@C_{60}$ for (a) AlB_2-type lattice and (b) $MgZn_2$-type lattice.*

AlB_2 and $MgZn_2$ lattices would be expected to stabilise a higher amount of charge on each $X@C_{60}$ as for each charge there will be two neutral fullerenes. Although we can see in Figure 5.9 that it isn't by much - a 1029 particle AlB_2 seems to be able to hold as much charge as both NaCl and CsCl - this is because although charges are further separated when placed on A in AB_2 this is met with diminishing attractive polarisation contributions. Of the two AB_2 systems in Figure 5.9, $MgZn_2$ is the most stable allowing 0.2 eV per $X@C_{60}$ in its 5x5x5 unit cell structure. This however consists of 1500 particles and so larger than the other three systems discussed, meaning it cannot be directly compared and only discussed in isolation. Its 12 particle unit cell can hold a singular charge on each charged particle implying that for this small

structure any of the metals in Table 5.2 could be encapsulated and a stable $(X@C_{60})_n(C_{60})_m$ could then be produced.

Table 5.4: Maximum charge held per cage and percentage of charged cages on the surface of the different size structures seen in the NaCl and CsCl-type lattices seen in Figure 5.8.

Lattice Type	**No. of Particles**	**Percentage of Charged Particles on the Surface**	**Max Charge per Charged Particle**
NaCl	8	100	0.80
	64	87.50	0.39
	216	70.37	0.26
	512	57.81	0.20
	1000	49.80	0.16
CsCl	16	87.50	0.62
	128	57.81	0.34
	250	49.8	0.28
	686	37.03	0.21
	1024	33.01	0.18

The distance between two fullerene cages in bulk is recorded as being 10.08Å [157], this represents surface-to-surface separation of 0 in calculations where the diameter used for the cage is 10.0511Å. The lattice constant for fullerite is recorded as 14.17Å[158], I record 14.2143.Å for the NaCl type lattice. My lattice constant for CsCl is 11.6060 Å, very comparable to what is expected from the equation:

$$4 \times \frac{5.025\mathring{A}}{3^{0.5}} = 11.6047 \tag{5.1}$$

Figure 5.10 and 5.11 show how many like and opposite charges are present in a 3x3x3 NaCl lattice and a CsCl lattice with 250 particles, respectively. It shows trends expected from a FCC and BCC packing comparison comparison with nearest like charge closer together in a CsCl-type lattice due to its more closely packed structure.

This is likely the reason we see that a CsCl-type lattice can hold less charge per endohedral fullerene than a NaCl-type lattice as Table 5.4 shows that they can hold 0.62 and 0.8 eV, respectively. The closer packing of the BCC structure leads to a sharper increase in repulsion between the charges.

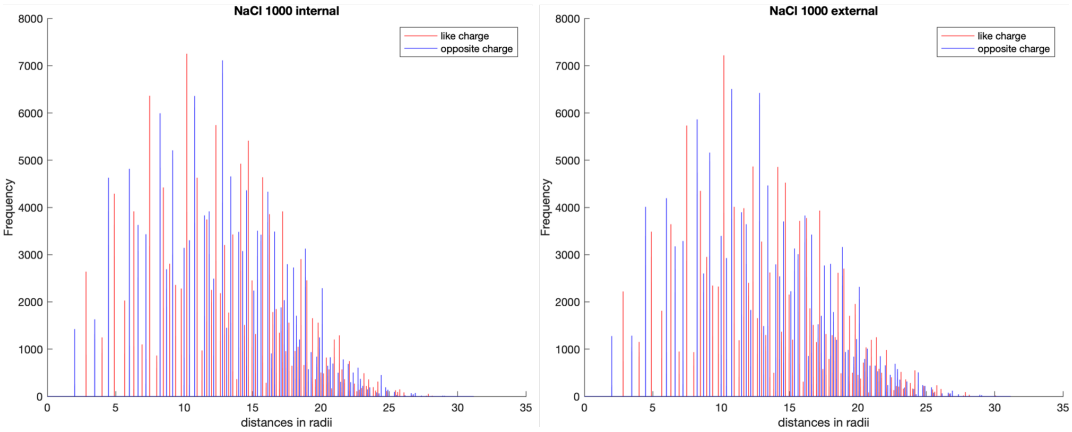

(a) **(b)**

Figure 5.10: *Distances to like and opposite charges in a 216 particle FCC NaCl lattice for (a) fullerenes in the centre of the lattice and (b) fullerenes on the surface.*

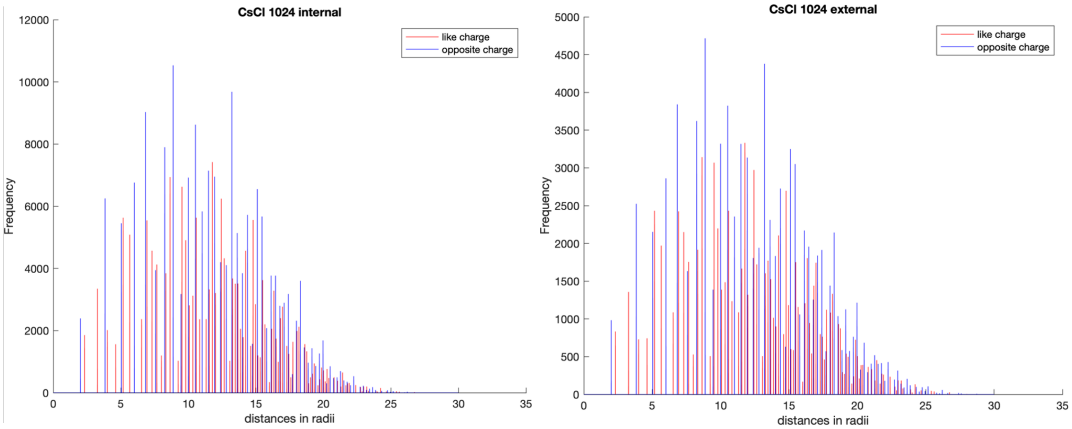

(a) **(b)**

Figure 5.11: *Distances to like and opposite charges in a 250 particle BCC CsCl lattice for (a) fullerenes in the centre of the lattice and (b) fullerenes on the surface.*

5.6 Stability of C_{84} Endohedral Fullerene Superlattice Structures

The availability of a suitable van der Waals potential for C_{84} has made it possible to extend the above calculations to explore the consequences of utilising larger fullerenes, which would then allow the accommodation of many of the more complex species discussed previously. However, there is the possibility that the inclusion of species other than atoms may change the shape of the fullerene cage.[144] For the purposes of these calculations on C_{84}, the van der Waals potential constructed by Girifalco[9] has been used together with the many-body electrostatic theory discussed above. There are a number of parameter sets available for the C_{84} Girifalco potential,[6] and those chosen for these calculations are given in Table 5.1. In addition, the dielectric constant has been increased from 3.46 used for C_{60} to 4.24[159].

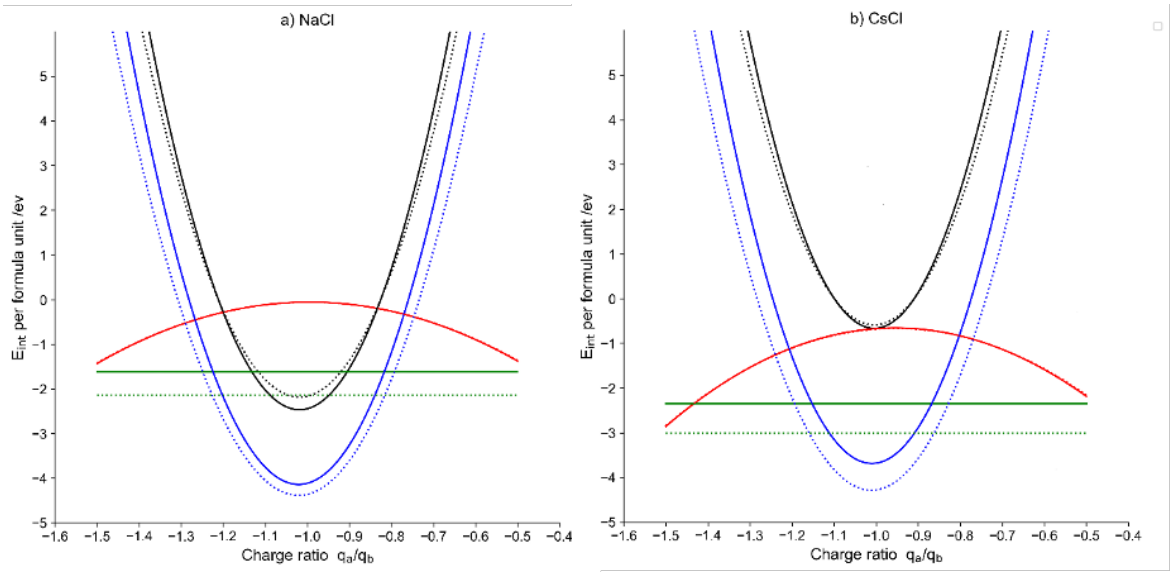

Figure 5.12: *Comparison between the stabilities of lattice structures composed of $X@C_{60}$ and $X@C_{84}$ fullerene cages. Individual contributions to the total energy per formula unit for lattice structures of the type: (a) NaCl and (b) CsCl, each consisting of equal numbers of positively and negatively charged X@Cn fullerene cages. The solid lines are for C_{60} and the dashed lines C_{84}. Coulomb interactions are shown in black, many-body polarisation interactions in red, and vdW interactions in green. The total interaction energies are shown as blue. For C_{60} the vdW contribution has been calculated using the PPR potential[5], and for C_{84} the Girifalco potential has been used[6, 9]*

Figure 5.12 shows the results, where the individual contributions to total lattice stability are compared for X@C_{60} and X@C_{84}. For the individual lattice types, NaCl and CsCl, there are competing contributions to the relative stability. The slightly larger size of C_{84} will lower surface charge density, which, in turn, will reduce both the Coulomb (most noticeable for the NaCl lattice) and polarisation interactions; however, the larger sphere will also be more polarisable. As can be seen from Figure 5.12, changes to the electrostatic interactions are marginal, with X@C_{60} appearing as the more stable; however, it is mainly through the van der Waals interaction that X@C_{84} acquires additional stability and for a CsCl lattice type this amounts to ~ 0.5 eV per formula unit.

5.7 Stability of C_{60}-C_{84} Endohedral Fullerene Superlattice Structures

While there has been a lot of work done on homogeneous fullerene interactions, there has been a lot less work done on non homogeneous interactions. Although binary clusters, which include two types of particles, have received some attention[160], still the general level of understanding remains far behind that of homogeneous clusters due to the huge parameter space. Bubnis *et al.*[161] investigated these clusters of composition $(C_{60})_n(C_{84})_{N-n}$ up to N$\leq$ 24 using the Girifalco potential and a basin-hopping method and concluded that their results suggest that further studies of larger clusters, and perhaps other fullerene species, could be fruitful in exploring how noncovalent interactions between fullerenes can control the self-assembly of supramolecular structures containing fullerene derivatives. However, because fullerenes come in a wide range of sizes, there appears to be a natural region in which mixed clusters with components of various sizes might be studied experimentally. There has been interest displayed in investigating mixtures of the fullerites[162, 163].

For the theoretical study of their thermodynamic properties, it is important to know the intermolecular forces acting between molecules of different fullerenes. Similarly to Girifalco[9], averaging the atom-atom interactions (Chapter 2) of the two C_m and C_n molecules with effective radii a_m and a_n over all their orientations, we obtain the intermolecular potential:

$$\begin{aligned} V &= -\frac{\alpha}{s}\Big(\frac{1}{s(s-1)^3}+\frac{1}{s(s+1)^3}-\frac{1}{s(s-\sigma)^3}+\frac{1}{s(s+\sigma)^3}\Big) \\ &= \frac{\beta}{s}\Big(\frac{1}{s(s-1)^9}-\frac{1}{s(s+1)^9}-\frac{1}{s(s-\sigma)^9}-\frac{1}{s(s+\sigma)^9}\Big) \end{aligned} \tag{5.2}$$

Here s= $\frac{r}{D_{mn}}$ where $D_{mn} = (a_m + a_n)$ and a_m and a_n are the effective radii $\sigma = \frac{(a_m - a_n)}{(a_m + A_n}$) and the coefficients α and β are defined by the formulae:

$$\alpha = \frac{mnA}{48a_m a_n (a_m a_n)^4}, \tag{5.3}$$

$$\beta = \frac{mnB}{360a_m a_n (a_m a_n)^{10}} \tag{5.4}$$

Therefore we can note that when m=n, the potential in Equation 5.2 transforms to the Girifalco potential for two C_n molecules. The coefficients for α and β are known for C_{60} molecules interacting with both smaller fullerenes[164] such as C_{36} and larger ones including C_{84} which we have looked into already using the Girifalco potential.

Table 5.5: Parameters used to describe van der Waals interactions using the Girifalco Potential[6] between C_{60}-C_{84}.

C_{60}-C_{84} Parameters	
d	0.7750 nm
α	6.245 $\times 10^{-}14$ erg
β	6.695 $\times 10^{-}17$ erg
R_0	1.0705 nm
$-\varepsilon/K_B$	3616 K

Table 5.5 lists the parameters needed for implementing the Girifalco potential alongside many-body theory to investigate the stabilities of C_{60}-C_{84} lattice structures. The same six lattice-types that were modelled for purely C_{60} structures were investigated, again as a function of charge as displayed in Figure 5.13 at their size ratio corresponding to a minimum in electrostatic energy, and so a maximum packing fraction.

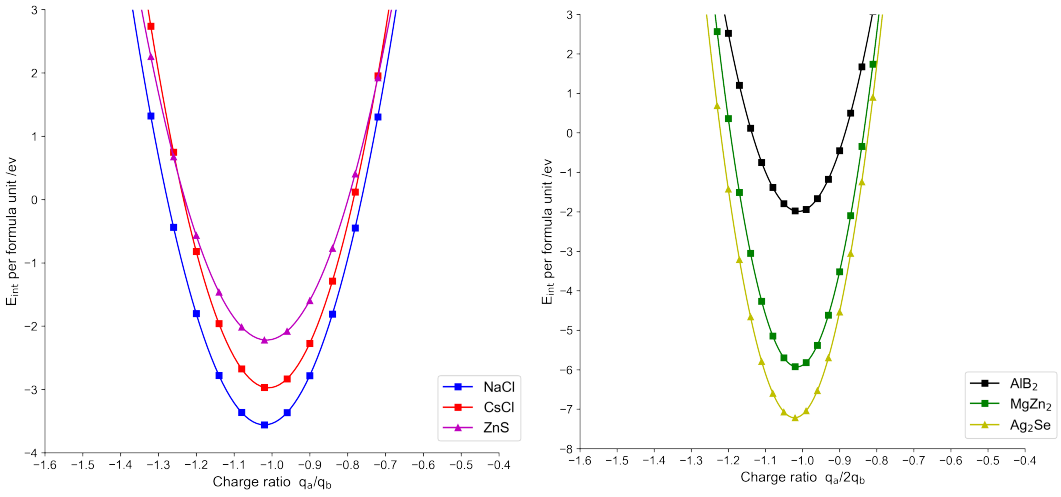

(a) *AB systems* **(b)** *AB_2 systems*

Figure 5.13: *1000 particle superlattice structures comprised of C_{60} and C_{84} fullerenes. For AB stoichiometries (a) and AB_2 stoichiometries where A is C_{60} and B is C_{84}.*

It is clear that just like in the singular fullerene superlattices investigated previously, these binary arrays are also highly stable over a wide range of charges. We can see in Figure 5.13 that their trends are comparable too with a NaCl-type structure being the lowest in interaction energy at $\sim$ -3.5 eV, followed by CsCl and ZnS, respectively. The actual energy is slightly less than in the homogeneous C_{60} systems as the larger A, C_{84} particle will distort packing and reduce Coulomb interactions. Hence, this is why we see the biggest reduction in energy in those systems that were found to have the least stabilisation due to polarisation such as NaCl and $MgZn_2$ whereas the change in those structures whose stability was due to a majority in multipolar interactions vary less, such as AlB_2.

5.8 Surface Charge Distributions of Non-Central Encapsulated Metal Atoms

In previous publications, an analytical solution for the distribution of charge on a dielectric sphere due to the presence of an external point charge has been presented. This describes how we see charge on the surface being polarised by an electric field into regions of positive and negative charge[165]. The solution assumes that the polarisable charge lies on the interface of the dielectric sphere and not inside the sphere and additionally, the outside of the sphere where the charge resides is in vacuum. This analytical solution was made in house by G. Raggi and was compared to partial atomic charges from quantum chemical calculations of C_{60} molecules using the same charge density assumptions. The results were published[165] as they found the analytical solution to be in good agreement with the DFT calculations. The assumption was made that it is possible to invert the model to account for an *'empty'* cavity with point charge moving inside and a dielectric medium meaning that the polarisable charge is on the interface between the dielectric and spherical empty cavity.

The majority of electrostatic solutions for a point charge and a particle on dielectrics, as well as conductors, are for situations where the point charge is outside the sphere, which is not the case in metallofullerenes. In addition to a previous theory handled by an infinite series of spherical harmonics and solved in terms of image line and point sources on a point charge placed inside and out, Sten *et al.*[166] offered one of only a few solutions for a particle inside a dielectric. This cannot be used as a direct comparison as we model the particles with their characteristic hollow centres.

There are a slew of additional scenarios in which being able to model charges inside the cage would be useful, ranging from biological structural research to physical applications[167]. Other physical uses of charge exisiting inside the

cage have been employed for molecular switching purposes such as $Ca@C_{60}$ and $Li@C_{60}$ endofullerenes based on charge-transfer excitation.

Until this point, the work in this Chapter has assumed a uniform distribution of charge across the surface of the fullerene cages - of equal magnitude and opposite sign to the encapsulated metal atom. This in turn implies that X in $X@C_{60}$ resides at the centre of the cage, which is not always necessarily the case[107–109, 116–118, 129–132]. An off-centre encapsulated atom would have the effect of redistributing the surface charge to facilitate a build-up of opposite charge on the portion of the cage that is nearest the atom. This now non-uniform surface charge on each cage would interact differently to the uniform cases investigated previously, affecting the stability of some of the lattice structures. Table 5.6 shows the equilibrium position of four atoms inside a C_{60} as calculated by DFT. It can be seen that chlorine is almost exactly central inside the cage and therefore would experience a uniform spread of surface charge on the cage after encapsulation. For calcium, lithium and fluorine, however, they are significantly closer to the side of the cage thus have a critical influence on the polarisation of the C_{60} cage.

The position of a trapped charge inside the cage is accompanied by large changes in electron density on the surrounding carbon cage, producing hemispheres of positive and negative charge with placements dependent on the position of the central charge.

Encapsulated atom	**Distance from the centre (Å)**
Ca	1.1886
Li	1.3551
Cl	0.0008
F	0.8875

Table 5.6: The distance from centre for four different atoms encapsulated inside a C_{60} in angstroms, as determined by DFT.

As chlorine is positioned centrally inside the fullerene, the cage would have energies comparable to those discussed previously with the uniform spread. Implying that, for the AB and AB_2 lattice types investigated, it is likely that their energies would be noted experimentally, with chlorine encapsulation providing positively charged C_{60} cages. It is important to note that the position of some metal atoms often remains unclear, even when the cage structure has been determined by single-crystal X-ray diffraction because there can be many possible metal positions with close energies and low barriers of interconversion. Many structures of endohedral metallofullerenes, especially those of mono- and dimetallofullerenes, remain unknown.[168]

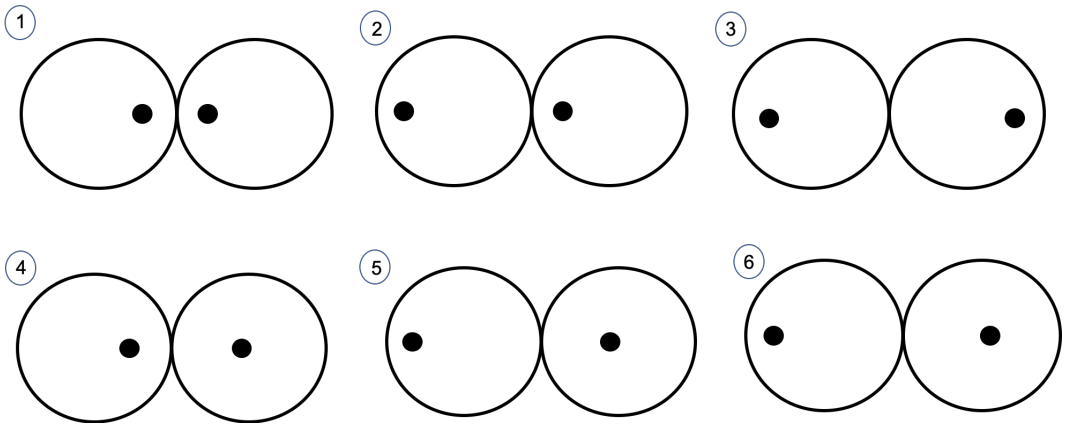

Figure 5.14: *Illustration of different orientations of off-centre atoms in C_{60} cages: (1) where the atoms are towards the side of the cages closest to one another, (2) when the atoms are both towards the same side of their respective cages, (3) atoms are towards opposite directions, (4) a more centrally positioned atom and a off-centre atom facing towards each other, (5) a centrally positioned atom and an off-centre atom positioned closest to each other, (6) a more centrally positioned atom and a off-centre atom facing opposite directions.*

Figure 5.14 shows three (1-3) orientations we could see in dimers with off-centre encapsulated atoms (Li, Ca or F for reference to Table 5.6) and three (4-6) ways we could find an off-centre encapsulated atom neighbouring a more centrally, uniformly distributed atom such as chlorine. In order to explore the effect that non-central encapsulation has on the stability of lattice structures, such as those previously investigated, we need to understand the multiple ways we could find dimers with non-uniform surface charge density. In a BNSL struc-

ture of ~ 1000 atoms, there is a multitude of ways that cages with non-uniform surface charge distributions will neighbour each other. Take a dimer of two $Ca@C_{60}$ in isolation for example. A less central position is accompanied by an electron transfer from calcium to the fullerene cage - inducing a concentrated area of negative charge on the cage at the point nearest the atom and a higher concentration of positive charge everywhere else. Energetically, it is favourable for the neighbouring $Ca@C_{60}$ to be a mirror image with the calcium off centre the same amount but in the opposite direction. This means that the induced charges on the cage contributed significantly to lowering the interaction energy. This is only the answer to the two-body problem. As soon as a third particle is introduced the equilibrium is redistributed as the iterative process happens across the whole structure meaning we are likely to see all different combinations of neighbours such as seen in Figure 5.14.

In order to model the non-uniform equilibrium surface charge distributions of $X@C_{60}$ cages where X is non-central (i.e. Ca, Li or F), partial charges were obtained using the density-derived electrostatic and chemical (DDEC) method, converted to a surface charge density function using Mathematica and finally, introduced in place of uniform charge spread in the electrostatic solution.

In Figure 5.15 we can see the difference this orientation of neighbouring charges can have on interaction energy. To start, the dielectric constant was set to unity to model the non-polarisable case. This can be seen in Figure 5.15(a) where the uniform surface charge density, represented by the magenta line, was -1.5976 eV. This was used to obtain trends in different encapsulated atoms and their positions before the dielectric constant was changed to 3.46, that of a fullerene cage and compared to the non-polarisable case. This was to ensure that we weren't seeing a significant change in the surface charge distributions from the central atom due to the neighbouring cage's charge. In the polarisable case of Figure 5.15(b), we see that the interaction energy for a uniform

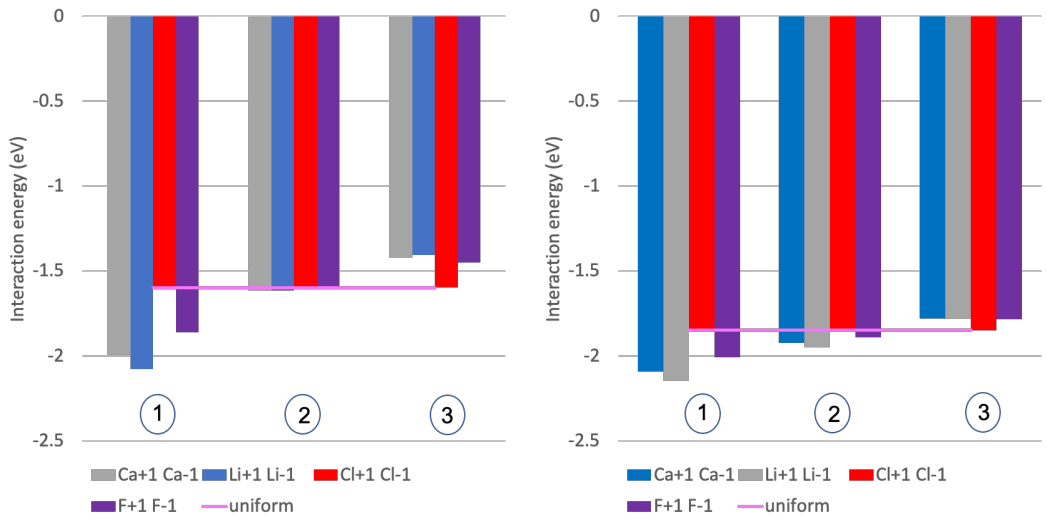

Figure 5.15: *Interaction energy for a (a) non-polarisable and (b) polarisable $X@C_{60}X@C_{60}$ dimer where X=Ca, Li, Cl or F, for orientations 1-3 in Figure 5.14of the encapsulated atom and a dielectric constant of 3.46.*

cage is now -1.850 eV and the $Cl@C_{60}$.$Cl@C_{60}$ dimer doesn't vary much from this value, due to its equilibrium position in the middle. For cases (1) and (2), we see increased stabilisation compared to the uniform case with (1) being the most stable. In this case, the atoms are closest to one another leading to significant stabilisation due to the polarisation of surface charge on the cages. (2) only comes with a minor change to interaction energy, unsurprising as the separation of the middle atoms in this placement isn't much different from the uniform case. Case (3) leads to a decline in the stability of all bar the chlorine dimers due to increase distance between the charges and therefore lowering their effect on one another.

The cases discussed above involved dimers with the same encapsulated metal in both C_{60} cages. This is less applicable to the work done in this study of endohedral fullerene superlattices where we see cages of alternating charges. Figure 5.16 show dimers composed of one fullerene cage with a centrally positioned encapsulated atom and a fullerene cage with an off-centre internal atom. The chlorine doesn't sit perfectly (but very nearly) symmetrical and so

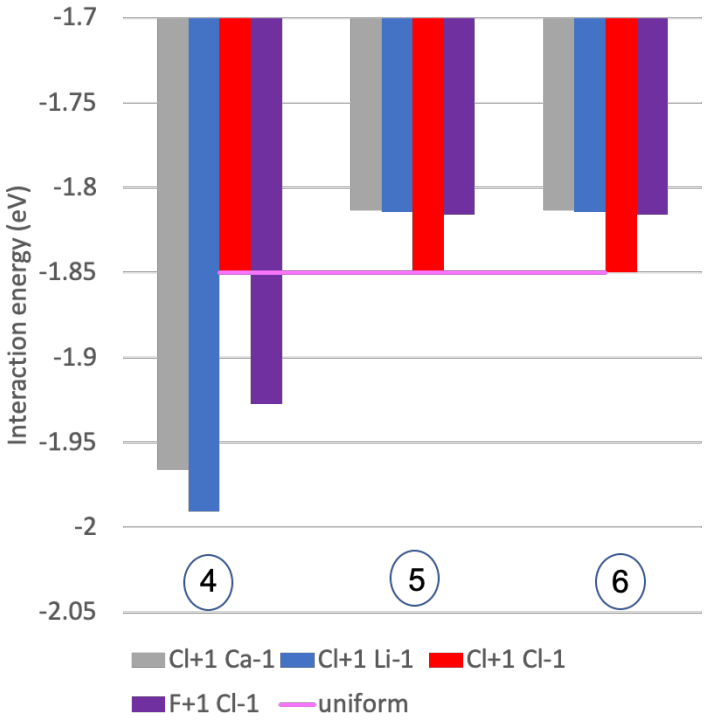

Figure 5.16: *Interaction energy for a polarisable $X@C_{60}Cl@C_{60}$ dimer where X=Ca, Li, Cl or F, for orientations 4-6 in Figure 5.14 of the encapsulated atom and a dielectric constant of 3.46.*

the side of the cage that it lies nearer to will see increase interactions due to a redistribution of surface charge. Figure 5.16 shows the interaction between a dimer where one has a centrally encapsulated atom, chlorine, and the other ranges in position within the cavity (Li, Ca, Cl and F).

The dielectric constant used here for the medium was 3.46, that corresponding to bulk C_{60}[4]. However, as we are keeping the cage empty (aka vacuum, k=1) this value no longer holds its specific significance. The dielectric constant of fullerene, as determined by the Clausius-Mossotti equation, is for the molecule as a whole. This includes the carbon cage and the cavity. In fact, as the dielectric doesn't begin until the cage in this model we propose that the value of k should match that of graphene more closely than buckminsterfullerene. Therefore the same polarisable calculations as discussed in Figure 5.15 and Figure 5.16 have been repeated with a dielectric constant of 6.9 for the medium.

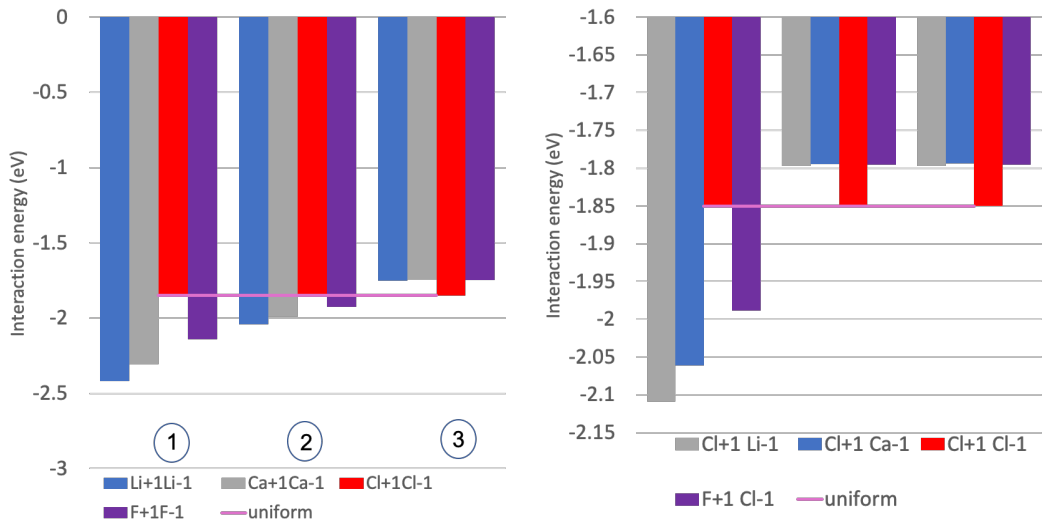

(a) **(b)**

Figure 5.17: *Interaction energy for a polarisable (a)$X@C_{60}X@C_{60}$ dimer and (b) $X@C_{60}Cl@C_{60}$ dimer where X=Ca, Li, Cl or F, for orientations 1-3 in Figure 5.14of the encapsulated atom and a dielectric constant of 6.90.*

A higher dielectric constant is a description of a material that is more highly polarisable. That is why, although we see the same trends for the binary dimer in Figure 5.17(a) and Figure 5.15(b), the magnitude of the interaction has increased. When k=3.46, we can see that the interaction energy between two cages with encapsulated Li was just over 2 eV. This has increased by nearly 25% to $\sim$ -2.5 eV when the cage is modelled as having a polarisbaility of graphene. The same trends are witnessed between Figure 5.17(b) and Figure 5.16 where in charge facing orientations the interaction is stronger whilst central sitting chlorine means that the cage remains comparable to uniform distribution.

This finding is integral to gaining a better understanding of the intermolecular forces responsible for stabilisation between endohedral fullerene cages. If we wish to test the robustness of our findings for stable superlattice structures, made of only uniform charge distributions over the fullerene cages, we need to be able to successfully model the disruption to surface charge that an off-centre encapsulated metal atom will have. The work discussed here begins the de-

scription of how charge on the surface of the sphere is polarised into regions of positive and negative charge density when the separation between the sphere and the point charge varies. This classical electrostatic analysis of charge for a sphere and internal, and an external, point charge have been validated against quantum chemical calculations based on DFT by Raggi *et al.*[165].

The polarisation effect due through the motion of the trapped charge inside the cavity could show potential as a polarisable nanoswtich. However, analysing the point charge inside a fullerene just by polarisation is not practical as it is predicted that the motion of a charge inside a cage would be accompanied by a large change in the electron density on the surrounding cage. Previous calculations have found that in $Ca@C_{60}$, the valence 4s electrons of the encapsulated Ca atom are energetically close to the LUMO of C_{60}, thus allowing for the prospect that none, one or both of the 4s electrons could be transferred to the C_{60} shell[169]. Although the C_{60} can officially accept one or two electrons donated from encapsulated electropositive atoms, the true amount of charged transferred is usually less.

In their minimum energy configurations, Ca, Li and F assume an off-centre position and the $X@C_{60}$ complex is stabilised by polarisation of the cage. Nonetheless, this gain in stabilisation from polarisation energy is partially offset by a simultaneous rise in repulsive interactions between the encapsulated charge and the wall of the dielectric cage[170]. That being said, the polarity of the embedded atom could be manipulated in order to control its position and therefore manipulate the magnetic moment - allowing for the use of a magnetoelectric nanoswitch.

5.9 Conclusions on Stable Structures

The proposal is that nanoparticle structures could be fabricated from combinations of appropriate endohedral fullerenes that are capable of forming stable lattices. From the results of calculations present here, it has been shown that stability is derived, in part, from electrostatic interactions between fullerenes, where the presence of certain endohedral atoms can induce either a negative or positive charge to reside on the cage. For AB and AB_2 structures, varying combinations of Coulomb, charge-induced and van der Waals interactions contribute to overall stability, and because the latter two interactions always enhance stability, their presence has been shown to extend the range of charges over which lattices are stable.

The proposed lattice structures differ from those previously identified by experiment for $Li@C_{60}$, in that their formation does not require electron transfer to a counter anion[116–118]. In addition to applications in the form of devices, recent calculations have also shown that arrays of $M@C_{60}$ (M = Na, K, Rb, Cs, Sc, Ti, Mn, Fe) could act as catalysts for the activation of hydrogen,[171] and that embedded metal clusters in the form $M_n@C_{60}$ (M = Mn, Co, Ni, Cu; n = 2–5) could stimulate the oxygen reduction reaction[172]. Both these processes are promoted by the presence of a negative charge on the fullerene cage, and since arrays of these materials alone might not be stable, the results presented above may offer a route to their fabrication.

Chapter 6

Conclusions and Future Work

6.1 Conclusions

The work in this thesis has evaluated the strength and demonstrated the versatility of the many-body polarisable electrostatic solution proposed by Lindgren *et al.*[34] in 2018, and in addition, included an accurate description of dispersion effects. This allows a complete understanding of fullerene clusters and BNSLs with the goal of computationally designing electrostatically stable endohedral fullerene superlattices.

Chapter 3 investigates the nature of fullerene cluster stability via Coulomb fragmentation. The preceding two-body model had already been used to conduct similar research[27], modelling clusters by a large sphere (representing multiple fullerenes) and a fragment; producing results similar to, but not in exact concurrence with, experiment and other theoretical models. With the many-body consideration we are able to build a more accurate view of the processes occurring and so provide results that are more closely matched to experimental results. However, it presented the extra consideration of dispersion forces. Cluster stabilities were assessed by the emission of a single, charged fullerene from a parent cluster and the interaction energies, a sum of the Coulomb, polarisation and vdW contributions, before and after frag-

mentation were compared. A lower interaction energy before fragmentation implies a stable cluster. However, if the energy is lower at large separations then the parent cluster can be said to be unstable or metastable. For clusters with charges $2 \leq q \geq 5$, minimum stable sizes were found to much more closely match those found in experiment compared to work using Bichoutskaia's two-body theory. The dispersion effects discussed and implemented in this work are adaptations of Hamaker's vdW equation, PPR and Girifalco.

Chapter 4 focuses on the flexibility of superlattice composition which suggests that controlled nanocrystal self-assembly could be an important enabler in next generation material design. The many-body electrostatic theory has been employed to investigate the significance of Coulombic and multipolar contributions to structural stability in novel AB and AB_2 binary nanoparticle superlattice structures. The calculations found that, in some lattice structures, 60% of the electrostatic energy comes from many-body polarisation effects, highlighting the importance in the consideration of the additive nature of polarisation rather than the use of pair-wise interactions. Without this many-body consideration the characterisation of true and local minima could be blurred. The atomic environment of a crystal structure was found to be significant with all AB structures having different contributions from Coulombic and multipolar effects. The constituent particles in a crystal having different atomic environments produced significantly different electrostatic stabilisation as was found by plotting lattice energy as functions of both AB(1) and A(1)B where (1) indicates the particle which is varying in size.

Chapter 5 marries these findings together. The proposal is that nanoparticle structures could be fabricated from combinations of appropriate endohedral fullerenes that are capable of forming stable lattices. From the results of calculations present here, it has been shown that stability is derived, in part, from electrostatic interactions between fullerenes, where the presence of cer-

tain endohedral atoms can induce either a negative or positive charge to reside on the cage. For AB and AB_2 structures, varying combinations of Coulomb, charge-induced and van der Waals interactions contribute to overall stability, and because the latter two interactions always enhance stability, their presence has been shown to extend the range of charges over which lattices are stable. The proposed lattice structures differ from those previously identified by experiment for $Li@C_{60}$, in that their formation does not require electron transfer to a counter anion[116–118]. In addition to applications in the form of devices, recent calculations have also shown that arrays of $M@C_{60}$ (M = Na, K, Rb, Cs, Sc, Ti, Mn, Fe) could act as catalysts for the activation of hydrogen,[171] and that embedded metal clusters in the form $M_n@C_{60}$ (M = Mn, Co, Ni, Cu; n = 2–5) could stimulate the oxygen reduction reaction[172]. Both these processes are promoted by the presence of a negative charge on the fullerene cage, and since arrays of these materials alone might not be stable, the results presented above may offer a route to their fabrication.

6.2 Limitations and Suggestions for Further Improvements

The work in Chapter 3 can be extended to include predictions for minimum stable cluster size, charge placements and fragmentation energies for clusters with charges of +6 and +7, if not higher. Further enhancement of the FMM is currently in progress[72], meaning that in the near future it will be achievable to produce a quantitative answer for clusters with these charges.

In order to have confidence in the prediction of the existence of the superlattices discussed in Chapter 4 going forward, energy minimisation will be implemented. This will inform if the electrostatic contribution to some space groups is sufficient orif all AB structures collapse down to the cubic NaCl

type lattice; ultimately providing a better data set to be able to compare to published hard-sphere theory. As mentioned, in order to definitively conclude that BNSL structures are stable, it is pertinent to conduct energy minimisation calculations. In order to continue with theory development, current work is focused on implementing a free energy minimisation function in MATLAB. Such an addition would also be of great use to other projects within the group, including the work on fullerene clusters.

As we are aware that most encapsulated metal atoms do not sit centrally in the fullerene cage, and as we have now quantifiably defined that this is likely to increase interaction between cages, it would therefore be very useful to be able to implement each cage in the superlattice structures to have non-uniform surface charge distributions. This would require implementation of the dynamics code as discussed[35]. Many-body theory tells us that the redistribution of the surface charge between a pair of endohedral C_{60} cages to their new equilibrium configuration, is not the same when they are in the presence of another charged cage. This is what makes modelling the large lattices structures using static, single-point calculations complicated. Using dynamics we can observe the redistribution of surface charge on each cage in the lattice in real time until they settle to their equilibrium orientation of surface charge, based on the position of neighbouring cages. This would ultimately allow us to calculate the interaction energy of these structures and draw conclusions on their stability for a wider range of encapsulated atoms, not just those that sit more centrally inside the cage.

Bibliography

[1] E. Bichoutskaia, A.L. Boatwright, A. Khachatourian, and A.J. Stace. Electrostatic analysis of the interactions between charged particles of dielectric materials. *The Journal of Chemical Physics*, 133(2):024105, 2010. doi: 10.1063/1.3457157.

[2] B. Manil, L. Maunoury, B.A. Huber, J. Jensen, H.T. Schmidt, H. Zettergren, H. Cederquist, S. Tomita, and P. Hvelplund. Highly charged clusters of fullerenes: Charge mobility and appearance sizes. *Phys. Rev. Lett.*, 91:215504, 2003. doi: 10.1103/PhysRevLett.91.215504.

[3] H. Zettergren, H.T. Schmidt, P. Reinhed, H. Cederquist, J. Jensen, P. Hvelplund, S. Tomita, B. Manil, J. Rangama, and B.A. Huber. Stabilities of multiply charged dimers and clusters of fullerenes. *The Journal of Chemical Physics*, 126(22):224303, 2007. doi: 10.1063/1.2743433.

[4] M. Nakamura and P. Hervieux. Stability and fragmentation of multiply charged clusters of fullerenes. 428:138–142, 2006. doi: 10.1016/j.cplett.2006.06.075.

[5] J. M. Pacheco and J. P. Prates Ramalho. First-principles determination of the dispersion interaction between fullerenes and their intermolecular potential. *Phys. Rev. Lett.*, 79:3873–3876, 1997. doi: 10.1103/PhysRevLett.79.3873.

[6] F. Micali, M.C. Abramo, and C. Caccamo. Bulk properties of c_{76} and c_{84} fullerites studied by md simulation based on a central two body intermolecular potential. *Journal of Physics and Chemistry of Solids*, 64 (2):319–324, 2003. doi: https://doi.org/10.1016/S0022-3697(02)00307-4.

[7] D.I. Sharapa, J.T. Margraf, A. Hesselmann, and T. Clark. Accurate Intermolecular Potential for the C_{60} Dimer: The Performance of Different Levels of Quantum Theory. *Journal of Chemical Theory and Computation*, 13(1):274–285, 2017. doi: 10.1021/acs.jctc.6b00869.

[8] M. Halstead, E. Besly, and A.J. Stace. Predicting the polarisation properties of functionalised ca@c_{60} using density functional theory. *Journal of Chemical Physics*, In Preparation, 2022.

[9] L. A. Girifalco. Molecular properties of fullerene in the gas and solid phases. *The Journal of Physical Chemistry*, 96(2):858–861, 1992. doi: 10.1021/j100181a061.

[10] D.J. Griffiths. *Introduction to electrodynamics.* Pearson, 4 edition, 2013.

[11] K.S. Schmitz. *Chapter 1 - Philosophy of Science*. Elsevier, 2018.

[12] Yıldız Ilhami and Craig MacEachern. *Historical Aspects of Energy*. Elsevier, 2018.

[13] W. Gilbert. *De Magnete*. Dover Classics of Science and Mathematics. Dover Publications, 1958.

[14] A. Wolf. *History of Science, Technology, and Philosophy in the Eighteenth Century*. Dover Classics of Science and Mathematics. Macmillan, 1939.

[15] Roderick W. Home. Franklin's electrical atmospheres. *The British Journal for the History of Science*, 6(2):131–151, 1972. doi: 10.1017/S0007087400012255.

[16] J.N. Israelachvili. *Intermolecular and surface forces*. Academic Press, 2011.

[17] W. Thomson. Extrait d'une lettre de m. william thomson à m. liouville. *Journal de Mathématiques Pures et Appliquées*, page 364–367, 1845.

[18] W. Thomson. Extraits de deux lettres adressées à m. liouville. *Journal de Mathématiques Pures et Appliquées*, pages 256–264, 1847.

[19] M.H. Davis. Two Charged Spherical Conductors in a Uniform Electric Field : Forces and Field Strength. *The Quarterly Journal of Mechanics and Applied Mathematics*, 17(4):499–511, 1964. doi: 10.1093/qjmam/17.4.499.

[20] A.A. Sickafoose, J.E. Colwell, M. Horányi, and S. Robertson. Photoelectric Charging of Dust Particles in Vacuum. *Physical Review Letters*, 84 (26):6034–6037, 2000. doi: 10.1103/PhysRevLett.84.6034.

[21] E. Allahyarov, E. Zaccarelli, F. Sciortino, P. Tartaglia, and H. Löwen. Interaction between charged colloids in a low dielectric constant solvent. *Europhysics Letters (EPL)*, 78(3):38002, 2007. doi: 10.1209/0295-5075/78/38002.

[22] B.A. Tinsley. The global atmospheric electric circuit and its effects on cloud microphysics. *Reports on Progress in Physics*, 71(6):66801, 2008. doi: 10.1088/0034-4885/71/6/066801.

[23] A. Jaworek, A. Krupa, and T. Czech. Modern electrostatic devices and methods for exhaust gas cleaning: A brief review. *Journal of Electrostatics*, 65(3):133–155, 2007. doi: https://doi.org/10.1016/j.elstat.2006.07.012.

[24] E. Bichoutskaia, A.L. Boatwright, A. Khachatourian, and A.J. Stace. Electrostatic analysis of the interactions between charged particles of dielectric materials. *The Journal of Chemical Physics*, 133(2):024105, 2010. doi: 10.1063/1.3457157.

[25] T.A. Mather and R.G. Harrison. Electrification of volcanic plumes. *Surveys in Geophysics*, 27(4):387–432, 2006. doi: 10.1007/s10712-006-9007-2.

[26] Y. Liang, N. Hilal, P. Langston, and V. Starov. Interaction forces between colloidal particles in liquid: Theory and experiment. *Advances in Colloid and Interface Science*, 134-135:151–166, 2007. doi: https://doi.org/10.1016/j.cis.2007.04.003.

[27] A.J. Stace and E. Besley. Treating highly charged carbon and fullerene clusters as dielectric particles. *Physical chemistry chemical physics : PCCP*, 13:18339–46, 2011. doi: 10.1039/c1cp21573f.

[28] B.A. Grzybowski, A. Winkleman, J.A. Wiles, Y. Brumer, and G.M. Whitesides. Electrostatic self-assembly of macroscopic crystals using contact electrification. *Nature Materials*, 2(4):241–245, 2003. doi: 10.1038/nmat860.

[29] M. Brunner, J. Dobnikar, H. von Grunberg, and C. Bechinger. Direct measurement of three-body interactions amongst charged colloids. *Phys. Rev. Lett.*, 92:078301, 2004. doi: 10.1103/PhysRevLett.92.078301.

[30] L.S. McCarty, A. Winkleman, and G.M. Whitesides. Electrostatic self-assembly of polystyrene microspheres by using chemically directed contact electrification. *Angewandte Chemie International Edition*, 46(1-2):206–209, 2007. doi: https://doi.org/10.1002/anie.200602914.

[31] A. Miller, M. Halstead, E. Besley, and A.J. Stace. Designing stable binary endohedral fullerene lattices. *Phys. Chem. Chem. Phys.*, 24:10044–10052, 2022. doi: 10.1039/D2CP00196A.

[32] R. Messina. Image charges in spherical geometry: Application to colloidal systems. *The Journal of Chemical Physics*, 117(24):11062–11074, 2002. doi: 10.1063/1.1521935.

[33] Z. Xu. Electrostatic interaction in the presence of dielectric interfaces and polarization-induced like-charge attraction. *Physical Review E*, 87(1):13307, 2013. doi: 10.1103/PhysRevE.87.013307.

[34] E.B. Lindgren, A.J. Stace, E. Polack, Y. Maday, B. Stamm, and E. Besley. An integral equation approach to calculate electrostatic interactions in many-body dielectric systems. *Journal of Computational Physics*, 371:712–731, 2018. doi: https://doi.org/10.1016/j.jcp.2018.06.015.

[35] E.B. Lindgren, B. Stamm, Y. Maday, E. Besley, and A.J. Stace. Dynamic simulations of many-body electrostatic self-assembly. *Philosophical Transactions A: Mathematical, Physical and Engineering Sciences*, 2018. doi: 10.1098/rsta.2017.0143.

[36] J.D. Jackson. Classical Electrodynamics, 3rd ed. *American Journal of Physics*, 67(9):841–842, 1999. doi: 10.1119/1.19136.

[37] M. Hassan and B. Stamm. A linear scaling in accuracy numerical method for computing the electrostatic forces in the N-body dielectric spheres problem. *Commun. Comput. Phys.*, 29(2):319–356, 2021.

[38] E.B. Lindgren, E. Stamm, B.and Besly, and A.J. Stace. The significance of induced electrostatic interactions for the controlled fabrication and stability of binary nanoparticle superlattices. *In preparation*, 2022.

[39] E.B. Lindgren, I.N. Derbenev, A. Khachatourian, H.-K. Chan, A.J. Stace, and E. Besley. Electrostatic self-assembly: Understanding the significance of the solvent. *Journal of Chemical Theory and Computation*, 14:905–915, 2018.

[40] E.B. Lindgren, B. Stamm, H.-K. Chan, Y. Maday, A.J. Stace, and E. Besley. The effect of like-charge attraction on aerosol growth in the atmosphere of titan. *Icarus*, 291:245–253, 2017.

[41] J. Baptiste, C. Williamson, J. Fox, A. J. Stace, M. Hassan, S. Braun, B. Stamm, I. Mann, and E. Besley. The influence of surface charge on the coalescence of ice and dust particles in the mesosphere and lower thermosphere. *Atmospheric Chemistry and Physics*, 21(11):8735–8745, 2021. doi: 10.5194/acp-21-8735-2021.

[42] G. Mie. Zur kinetischen theorie der einatomigen körper. *Annalen der Physik*, 316(8):657–697, 1903. doi: https://doi.org/10.1002/andp.19033160802.

[43] H.C. Hamaker. The London—van der Waals attraction between spherical particles. *Physica*, 4(10):1058–1072, 1937. doi: https://doi.org/10.1016/S0031-8914(37)80203-7.

[44] S. E. Mason, P.H. Beton, and N.A. Besley. Airbed: A simplified density functional theory model for physisorption on surfaces. *Journal of Chemical Theory and Computation*, 15(10):5628–5634, 2019. doi: 10.1021/acs.jctc.9b00576.

[45] F. Calvayrac, P.-G. Reinhard, E. Suraud, and C.A. Ullrich. Nonlinear electron dynamics in metal clusters. *Physics Reports*, 337(6):493–578, 2000. doi: https://doi.org/10.1016/S0370-1573(00)00043-0.

[46] K. Sattler. *Handbook of Nanophysics, Clusters and Fullerenes*. 2010.

[47] M. C. Abramo and C. Caccamo. A molecular dynamics study of impurity desorption from solid clusters of rigid c_{60} molecules. *The Journal of Chemical Physics*, 106(15):6475–6482, 1997. doi: 10.1063/1.473613.

[48] A. Cheng, M.L. Klein, and C. Caccamo. Prediction of the phase diagram of rigid c_{60} molecules. *Phys. Rev. Lett.*, 71:1200–1203, 1993. doi: 10.1103/PhysRevLett.71.1200.

[49] Y. Saito, T. Yoshikawa, N. Fujimoto, and H. Shinohara. C_{84} thin films grown epitaxially on mica. *Phys. Rev. B*, 48:9182–9185, 1993. doi: 10.1103/PhysRevB.48.9182.

[50] Y. Saito, N. Fujimoto, K. Kikuchi, and Y. Achiba. C_{76} thin films grown on mica and nacl substrates. *Phys. Rev. B*, 49:14794–14797, 1994. doi: 10.1103/PhysRevB.49.14794.

[51] V.I. Zubov, N.P. Tretiakov, and I.V. Zubov. Molecular interactions in fullerenes and equilibrium of higher fullerites c_{76} and c_{84} with their vapors. *The European Physical Journal B - Condensed Matter and Complex Systems*, 17(4):629–633, 2000. doi: 10.1007/s100510070101.

[52] Y.B. Melnichenko, G.D. Wignall, R.N. Compton, and G. Bakale. Characterization of fullerenes and fullerene derivatives by small-angle neutron scattering and transmission measurements. *The Journal of Chemical Physics*, 111(10):4724–4728, 1999. doi: 10.1063/1.479234.

[53] H.W. Kroto, J.R. Heath, S.C. O'Brien, R.F. Curl, and R.E. Smalley. C_{60}: Buckminsterfullerene. *Nature*, 318(6042):162–163, 1985. doi: 10.1038/318162a0.

[54] T.A. Mamvura and G.S. Simate. Chapter 4 - the potential application of graphene nanotechnology for renewable energy systems. In Mohammad Jawaid, Akil Ahmad, and D. Lokhat, editors, *Graphene-Based Nanotechnologies for Energy and Environmental Applications*, Micro and Nano Technologies, pages 59–80. Elsevier, 2019. doi: https://doi.org/10.1016/B978-0-12-815811-1.00004-1.

[55] S.E. Huber, M. Gatchell, H. Zettergren, and A. Mauracher. A precedent of van-der-Waals interactions outmatching Coulomb explosion. *Carbon*, 109:843–850, 2016. doi: 10.1016/J.CARBON.2016.08.056.

[56] T. P. Martin, U. Näher, H. Schaber, and U. Zimmermann. Clusters of fullerene molecules. 70:3079–3082, 1993. doi: 10.4028/www.scientific.net/MSF.232.155.

[57] C. Rey, L.J. Gallego, and J.A. Alonso. Molecular-dynamics study of the structure, binding energy, and melting of small clusters of fullerene molecules using Girifalco's spherical model. *Physical Review B*, 49(12):8491–8494, 1994. doi: 10.1103/PhysRevB.49.8491.

[58] J.P.K. Doye, D.J. Wales, W. Branz, and F. Calvo. Modeling the structure of clusters of c_{60} molecules. *Phys. Rev. B*, 64:235409, 2001. doi: 10.1103/PhysRevB.64.235409.

[59] C. Rey, J. Garcia-Rodeja, and L. Gallego. Computer simulation study of the ground-state structures of singly ionized clusters of C_ {60} molecules. 69, 2004. doi: 10.1103/PhysRevB.69.073404.

[60] A. Piatek, A. Dawid, and Z. Gburski. The existence of a plastic phase and a solid–liquid dynamical bistability region in small fullerene cluster (csub60/sub)sub7/sub: molecular dynamics simulation. *Journal of Physics: Condensed Matter*, 18(37):8471–8480, 2006. doi: 10.1088/0953-8984/18/37/006.

[61] W. Branz, N. Malinowski, A. Enders, and T.P. Martin. Structural transition in C_{60} clusters. *Physical Review B*, 66(9):94107, 2002. doi: 10.1103/PhysRevB.66.094107.

[62] A.J. Stace and E. Bichoutskaia. Reply to the 'comment on "treating highly charged carbon and fullerene clusters as dielectric particles"' by h. zettergren and h. cederquist, phys. chem. chem. phys., 2012, 14, doi: 10.1039/c2cp42883k. *Phys. Chem. Chem. Phys.*, 14:16771–16772, 2012. doi: 10.1039/C2CP43407E.

[63] H. Zettergren, B.O Forsberg, and H. Cederquist. Are single c_{60} fullerenes dielectric or metallic? *Phys. Chem. Chem. Phys.*, 14:16360–16364, 2012. doi: 10.1039/C2CP42884A.

[64] X. Wang, C. Ding, and L. Wang. High resolution photoelectron spectroscopy of c_{60}^-. *The Journal of Chemical Physics*, 110(17):8217–8220, 1999. doi: 10.1063/1.478732.

[65] M.Y. Amusia and A.S. Baltenkov. On the possibility of considering the fullerene shell c_{60} as a conducting sphere. *Physics Letters A*, 360(2): 294–298, 2006. doi: https://doi.org/10.1016/j.physleta.2006.08.056.

[66] Patrick W Fowler and Tomaz Pisanski. Homo-lumo maps for chemical graphs. *MATCH Commun. Math. Comput. Chem*, 64(2):373–390, 2010.

[67] R Antoine, Ph. Dugourd, D Rayane, E Benichou, M Broyer, F Chandezon, and C Guet. Direct measurement of the electric polarizability of isolated C_{60} molecules. *The Journal of Chemical Physics*, 110(19): 9771–9772, 1999. doi: 10.1063/1.478944.

[68] S. Sami, P.A.B. Haase, R. Alessandri, R. Broer, and R.W.A. Havenith. Can the dielectric constant of fullerene derivatives be enhanced by side-chain manipulation? a predictive first-principles computational study. *The Journal of Physical Chemistry A*, 122(15):3919–3926, 2018. doi: 10.1021/acs.jpca.8b01348.

[69] J.P.K. Doye, D.J. Wales, W. Branz, and F. Calvo. Modeling the structure of clusters of c_{60} molecules. *Phys. Rev. B*, 64:235409, 2001. doi: 10.1103/PhysRevB.64.235409.

[70] D.J. Wales and J.P.K. Doye. Global optimization by basin-hopping and the lowest energy structures of lennard-jones clusters containing up to 110 atoms. *The Journal of Physical Chemistry A*, 101(28):5111–5116, 1997. doi: 10.1021/jp970984n.

[71] Z. Li and H.A. Scheraga. Monte carlo-minimization approach to the multiple-minima problem in protein folding. *Proceedings of the National Academy of Sciences*, 84(19):6611–6615, 1987. doi: 10.1073/pnas.84.19.6611.

[72] J. Baptiste S. Braun A.J. Stace E. Besley M. Hassan, C. Williamson and B.Stamm. Manipulating interactions between polarisable particles with

electric fields: A general electrostatic many-body framework. *Journal of Chemical Theory*, 2022. doi: inpress.

[73] E.V. Shevchenko, D.V. Talapin, N.A. Kotov, S. O'Brien, and C.B. Murray. Structural diversity in binary nanoparticle superlattices. *Nature*, 439(7072):55–59, 2006. doi: 10.1038/nature04414.

[74] J. Cheon, J. Park, J. Choi, Y. Jun, S. Kim, M.G. Kim, Y. Kim, and Y.J. Kim. Magnetic superlattices and their nanoscale phase transition effects. *Proceedings of the National Academy of Sciences*, 103(9):3023–3027, 2006. doi: 10.1073/pnas.0508877103.

[75] J. V. Sanders. Close-packed structures of spheres of two different sizes i. observations on natural opal. *Philosophical Magazine A*, 42(6):705–720, 1980. doi: 10.1080/01418618008239379.

[76] P.N. Pusey and W. van Megen. Phase behaviour of concentrated suspensions of nearly hard colloidal spheres. *Nature*, 320(6060):340–342, 1986. doi: 10.1038/320340a0.

[77] M.D. Eldridge, P.A. Madden, and D. Frenkel. Entropy-driven formation of a superlattice in a hard-sphere binary mixture. *Nature*, 365(6441): 35–37, 1993. doi: 10.1038/365035a0.

[78] P. G. Bolhuis, D. Frenkel, Siun-Choun Mau, and David A. Huse. Entropy difference between crystal phases. *Nature*, 388(6639):235–236, 1997. doi: 10.1038/40779.

[79] M.A. Boles, M. Engel, and D.V. Talapin. Self-assembly of colloidal nanocrystals: From intricate structures to functional materials. *Chemical Reviews*, 116(18):11220–11289, 2016. doi: 10.1021/acs.chemrev.6b00196.

[80] D.V. Talapin and C.B. Murray. Pbse nanocrystal solids for n- and p-channel thin film field-effect transistors. *Science*, 310(5745):86–89, 2005. doi: 10.1126/science.1116703.

[81] G. Konstantatos, I. Howard, A. Fischer, S. Hoogland, J. Clifford, E. Klem, L. Levina, and E.H. Sargent. Ultrasensitive solution-cast quantum dot photodetectors. *Nature*, 442(7099):180–183, 2006. doi: 10.1038/nature04855.

[82] S.G.E. Te Velthuis, J.S. Jiang, S.D. Bader, and G.P. Felcher. Spin flop transition in a finite antiferromagnetic superlattice: Evolution of the magnetic structure. *Physical Review Letters*, 89(12):127203–, 2002. doi: 10.1103/PhysRevLett.89.127203.

[83] T.C. Harman, P.J. Taylor, M.P. Walsh, and B.E. LaForge. Quantum dot superlattice thermoelectric materials and devices. *Science*, 297(5590): 2229–2232, 2002. doi: 10.1126/science.1072886.

[84] S.E.F. Kleijn, S.C.S. Lai, M.T. M. Koper, and P.R. Unwin. Electrochemistry of nanoparticles. *Angewandte Chemie International Edition*, 53(14):3558–3586, 2014. doi: 10.1002/anie.201306828.

[85] G.M. Whitesides and B.A. Grzybowski. Self-assembly at all scales. *Science*, 295:2418–2421, 3/29/02 2002.

[86] D.K. Smith, B. Goodfellow, Detlef-M. Smilgies, and B.A. Korgel. Self-assembled simple hexagonal ab2 binary nanocrystal superlattices: Sem, gisaxs, and defects. *Journal of the American Chemical Society*, 131(9): 3281–3290, 2009. doi: 10.1021/ja8085438.

[87] E. Pretti, H. Zerze, M. Song, Y. Ding, N.A. Mahynski, H.W. Hatch, V.K. Shen, and J. Mittal. Assembly of three-dimensional binary superlattices from multi-flavored particles. *Soft Matter*, 14:6303–6312, 2018. doi: 10.1039/C8SM00989A.

[88] K.J. Si, Y. Chen, Q. Shi, and W. Cheng. Nanoparticle superlattices: The roles of soft ligands. *Advanced Science*, 5(1):1700179, 2018. doi: https://doi.org/10.1002/advs.201700179.

[89] M.I. Bodnarchuk, M.V. Kovalenko, W. Heiss, and D.V. Talapin. Energetic and entropic contributions to self-assembly of binary nanocrystal superlattices: Temperature as the structure-directing factor. *Journal of the American Chemical Society*, 132(34):11967–11977, 2010. doi: 10.1021/ja103083q.

[90] E.V. Shevchenko, D.V. Talapin, C.B. Murray, and S. O'Brien. Structural characterization of self-assembled multifunctional binary nanoparticle superlattices. *Journal of the American Chemical Society*, 128(11): 3620–3637, 2006. doi: 10.1021/ja0564261.

[91] M.A. Boles and D.V. Talapin. Many-body effects in nanocrystal superlattices: Departure from sphere packing explains stability of binary phases. *Journal of the American Chemical Society*, 137(13):4494–4502, 2015. doi: 10.1021/jacs.5b00839.

[92] E. Trizac, M.D. Eldridge, and P.A. Madden. Stability of the ab crystal for asymmetric binary hard sphere mixtures. *Molecular Physics*, 90(4): 675–678, 1997. doi: 10.1080/002689797172408.

[93] D. Frenkel. Entropy-driven phase transitions. *Physica A: Statistical Mechanics and its Applications*, 263(1):26–38, 1999. doi: https://doi.org/10.1016/S0378-4371(98)00501-9.

[94] X. Ye, C. Zhu, P. Ercius, S.N. Raja, B. He, M.R. Jones, M.R. Hauwiller, Y. Liu, T. Xu, and A.P. Alivisatos. Structural diversity in binary superlattices self-assembled from polymer-grafted nanocrystals. *Nature Communications*, 6(1):10052, 2015. doi: 10.1038/ncomms10052.

[95] M. de Jong, W. Chen, T. Angsten, A. Jain, R. Notestine, A. Gamst, M. Sluiter, C. Krishna Ande, S. van der Zwaag, J.J. Plata, C. Toher, S. Curtarolo, G. Ceder, K.A. Persson, and M. Asta. Charting the complete elastic properties of inorganic crystalline compounds. *Scientific Data*, 2, 2015. doi: 10.1038/sdata.2015.9.

[96] A. Jain, S.P. Ong, G. Hautier, W. Chen, W.D. Richards, S. Dacek, S. Cholia, D. Gunter, D. Skinner, G. Ceder, and K.A. Persson. The Materials Project: A materials genome approach to accelerating materials innovation. *APL Materials*, 1(1):011002, 2013. doi: 10.1063/1.4812323.

[97] X. Ye, J. Chen, and C.B. Murray. Polymorphism in self-assembled ab6 binary nanocrystal superlattices. *Journal of the American Chemical Society*, 133(8):2613–2620, 2011. doi: 10.1021/ja108708v.

[98] P. Bartlett and A.I. Campbell. Three-dimensional binary superlattices of oppositely charged colloids. *Phys. Rev. Lett.*, 95:128302, 2005. doi: 10.1103/PhysRevLett.95.128302.

[99] A. Ben-Simon, H. Eshet, and E. Rabani. On the phase behavior of binary mixtures of nanoparticles. *ACS Nano*, 7(2):978–986, 2013. doi: 10.1021/nn302712h.

[100] L. Filion and M. Dijkstra. Prediction of binary hard-sphere crystal structures. *Physical review. E, Statistical, nonlinear, and soft matter physics*, 79(4 Pt 2):046714, 2009. doi: 10.1103/physreve.79.046714.

[101] J.K. Kummerfeld, T.S. Hudson, and P. Harrowell. The densest packing of ab binary hard-sphere homogeneous compounds across all size ratios. *The Journal of Physical Chemistry B*, 112(35):10773–10776, 2008. doi: 10.1021/jp804953r.

[102] M.E. Leunissen, C.G. Christova, A. Hynninen, C.P. Royall, A. I. Campbell, A. Imhof, M. Dijkstra, R. van Roij, and A. van Blaaderen. Ionic colloidal crystals of oppositely charged particles. *Nature*, 437(7056):235–240, 2005. doi: 10.1038/nature03946.

[103] V. Lee, S.R. Waitukaitis, M.Z. Miskin, and H.M. Jaeger. Direct observation of particle interactions and clustering in charged granular streams. *Nature Physics*, 11(9):733–737, 2015. doi: 10.1038/nphys3396.

[104] M. Boles, M. Engel, and D.V. Talapin. Self-assembly of colloidal nanocrystals: From intricate structures to functional materials. *Chemical Reviews*, 116(18):11220–11289, 2016. doi: 10.1021/acs.chemrev.6b00196. PMID: 27552640.

[105] R. Tan, H. Zhu, C. Cao, and O. Chen. Multi-component superstructures self-assembled from nanocrystal building blocks. *Nanoscale*, 8: 9944–9961, 2016. doi: 10.1039/C6NR01662F.

[106] A.M. Kalsin, M. Fialkowski, M. Paszewski, S.K. Smoukov, K.J.M. Bishop, and B.A. Grzybowski. Electrostatic self-assembly of binary nanoparticle crystals with a diamond-like lattice. *Science*, 312(5772): 420–424, 2006. doi: 10.1126/science.1125124.

[107] X. Lu, L. Feng, T. Akasaka, and S. Nagase. Current status and future developments of endohedral metallofullerenes. *Chem. Soc. Rev.*, 41:7723–7760, 2012. doi: 10.1039/C2CS35214A.

[108] A.A. Popov, S. Yang, and L. Dunsch. Endohedral fullerenes. *Chemical Reviews*, 113(8):5989–6113, 2013. doi: 10.1021/cr300297r. PMID: 23635015.

[109] H. Shinohara and N. Tagmatarchis. *Endohedral Metallofullerenes—Fullerenes with Metal Inside*. Wiley, 2015.

[110] K. Zhang, C. Wang, and M. *et al.* Zhang. A gd@c82 single-molecule electret. *Nature Nanotechnology*, 15(12):1019–1024, 2020.

[111] H.J. Chandler, M. Stefanou, E.B. Campbell, and R. Schaub. Li@c_{60} as a multi-state molecular switch. *Nature Communications*, 10(1):2283, 2019. doi: 10.1038/s41467-019-10300-2.

[112] R. Tellgmann, N. Krawez, S. H. Lin, I. V. Hertel, and E.B. Campbell. Endohedral fullerene production. *Nature*, 382(6590):407–408, 1996. doi: 10.1038/382407a0.

[113] G. Raggi, A. J. Stace, and E. Bichoutskaia. Polarisation charge switching through the motion of metal atoms trapped in fullerene cages. *Phys. Chem. Chem. Phys.*, 16:23869–23873, 2014. doi: 10.1039/C4CP02672A.

[114] Chad R. Snyder and Jack F. Douglas. Determination of the dielectric constant of nanoparticles. 1. dielectric measurements of buckminsterfullerene solutions. *The Journal of Physical Chemistry B*, 104(47): 11058–11065, 2000. doi: 10.1021/jp002024y.

[115] J.P.K. Doye and D.J. Wales. The structure of (c_{60})n clusters. *Chemical Physics Letters*, 262(1):167–174, 1996. doi: https://doi.org/10.1016/0009-2614(96)01039-1.

[116] S. Aoyagi, E. Nishibori, and H. *et al.* Sawa. A layered ionic crystal of polar li@c_{60} superatoms. *Nature Chemistry*, 2(8):678–683, 2010. doi: 10.1038/nchem.698.

[117] S. Aoyagi, Y. Sado, and E. Nishibori *et al.* Rock-salt-type crystal of thermally contracted c_{60} with encapsulated lithium cation. *Angewandte Chemie - International Edition*, 51(14):3377–3381, 2012. doi: 10.1002/anie.201108551. Copyright: Copyright 2012 Elsevier B.V., All rights reserved.

[118] S. Aoyagi, K. Miwa, H. Ueno, H. Okada, Y. Matsuo, and K. Kokubo. Structure of [60]fullerene with a mobile lithium cation inside. *Royal Society Open Science*, 5(7):180337, 2018. doi: 10.1098/rsos.180337.

[119] A. Nakagawa, M. Nishino, H. Niwa, and *et al.* Crystalline functionalized endohedral c_{60} metallofullerides. *Nature Communications*, 9(1): 3073, 2018. doi: 10.1038/s41467-018-05496-8.

[120] I.N. Derbenev, A.V. Filippov, A.J. Stace, and E. Besley. Electrostatic interactions between spheroidal dielectric particles. *The Journal of Chemical Physics*, 152(2):024121, 2020. doi: 10.1063/1.5129756.

[121] S. Yihan. *Molecular Physics*, 113(2):184–215, 2015. doi: 10.1080/00268976.2014.952696.

[122] T.A. Manz and N.G Limas. Introducing ddec6 atomic population analysis: Part 1. charge partitioning theory and methodology. *RSC Advances*, 6:47771– 47801, 2016.

[123] T.A. Manz and D.S. Sholl. Chemically meaningful atomic charges that reproduce the electrostatic potential in periodic and nonperiodic materials. *J. Chem. Theory Comput.*, 6:2455–2468, 2010.

[124] T.A. Manz and D.S. Sholl. Improved atoms-in-molecule charge partitioning functional for simultaneously reproducing the electrostatic potential and chemical states in periodic and nonperiodic materials. *J. Chem. Theory Comput.*, 8:2844–2867, 2012.

[125] F. L. Hirshfeld. Bonded-atom fragments for describing molecular charge densities. *Theor. Chim. Acta*, 44:129–138, 1977.

[126] R.J. Lillestolen, T.C.; Wheatley. Redefining the atom: Atomic charge densities produced by an iterative stockholder approach. *Chem. Commun.*, pages 5909–5911, 2008.

[127] C.A. Silvera Batista, R.G. Larson, and N.A. Kotov. Nonadditivity of nanoparticle interactions. *Science*, 350(6257):1242477, 2015. doi: 10.1126/science.1242477.

[128] A.J. Stace, A.L Boatwright, A. Khachatourian, and E. Bichoutskaia. Why like-charged particles of dielectric materials can be attracted to one another. *J Colloid Interface Sci*, 354(1):417–420, 2011. doi: 10.1016/j.jcis.2010.11.030.

[129] A.K. Srivastava, S.K. Pandey, A.K. Pandey, and N. Misra. C_{60} as electron acceptor and donor: A comparative dft study of li@c_{60} and f@c_{60}. *Australian Journal of Chemistry*, 71(12):953–956, 2018.

[130] E. Broclawik and A. Eilmes. Density functional study of endohedral complexes m@c_{60} (m=li, na, k, be, mg, ca, la, b, al): Electronic properties, ionization potentials, and electron affinities. *The Journal of Chemical Physics*, 108(9):3498–3503, 1998. doi: 10.1063/1.475783.

[131] A.K. Srivastava, S. Pandey, and N. Misra. Encapsulation of lawrencium into c_{60} fullerene: Lr@c_{60} versus li@c_{60}. *Materials Chemistry and Physics*, 177, 2016. doi: 10.1016/j.matchemphys.2016.04.050.

[132] C. Du, K. Jin, and X. Liu. Electronic and optical properties of gold-doped endohedral fullerenes. *Journal of Materials Science*, 55:12980–12994, 2020.

[133] H. Ueno, S. Aoyagi, Y. Yamazaki, K. Ohkubo, N. Ikuma, H. Okada, T. Kato, Y. Matsuo, S. Fukuzumi, and K. Kokubo. Electrochemical reduction of cationic li+@c_{60} to neutral li+@c_{60}˙−: isolation and characterisation of endohedral [60]fulleride. *Chem. Sci.*, 7:5770–5774, 2016. doi: 10.1039/C6SC01209D.

[134] H. Okada, H. Ueno, Y. Takabayashi, T. Nakagawa, M. Vrankić, J. Arvanitidis, T. Kusamoto, K. Prassides, and Y. Matsuo. Chemical reduction of li+@c_{60} by decamethylferrocene to produce neutral li+@c_{60}^{-}. *Carbon*, 153:467–471, 2019. doi: https://doi.org/10.1016/j.carbon.2019.07.028.

[135] S. Stevenson, G. Rice, T. Glass, K. Harich, F. Cromer, M. R. Jordan, J. Craft, E. Hadju, R. Bible, M. M. Olmstead, K. Maitra, A. J. Fisher, A. L. Balch, and H. C. Dorn. Small-bandgap endohedral metallofullerenes in high yield and purity. *Nature*, 401(6748):55–57, 1999. doi: 10.1038/43415.

[136] Debo Hao, Le Yang, Bo Li, Qinghua Hou, Lanlan Li, and Peng Jin. Discovery of a superatom inside the fullerene cage. *The Journal of Physical Chemistry A*, 124(13):2694–2699, 2020. doi: 10.1021/acs.jpca.0c01228.

[137] Celina Sikorska. When a nanoparticle meets a superhalogen: a case study with c_{60} fullerene. *Phys. Chem. Chem. Phys.*, 18:18739–18749, 2016. doi: 10.1039/C6CP00380J.

[138] Y. Shi, S. Bian, Y. Ma, Y. Wang, J. Ren, and X. Kong. Structures and superhalogen properties of pt_2cl_n ($2 \leq n \geq 10$) clusters. *The Journal of Physical Chemistry A*, 123(1):187–193, 2019. doi: 10.1021/acs.jpca.8b08349.

[139] C. Sikorska. Mg3f7: A superhalogen with potential for new nanomaterials design. *International Journal of Quantum Chemistry*, 118(21): e25728, 2018. doi: https://doi.org/10.1002/qua.25728.

[140] X. Wang and L. Wang. Experimental observation of a very high second electron affinity for zrf6 from photodetachment of gaseous zrf_6^{2-} doubly charged anions. *The Journal of Physical Chemistry A*, 104(19):4429–4432, 2000. doi: 10.1021/jp000362t.

[141] S. Giri, B.Z. Child, J. Zhou, and P. Jena. Unusual stability of multiply charged organo-metallic complexes. *RSC Adv.*, 5:44003–44008, 2015. doi: 10.1039/C5RA04344A.

[142] G. Chen, T. Zhao, Q. Wang, and P. Jena. Rational design of stable dianions and the concept of super-chalcogens. *The Journal of Physical Chemistry A*, 123(27):5753–5761, 2019. doi: 10.1021/acs.jpca.9b01519.

[143] P. Jena and Q. Sun. Super atomic clusters: Design rules and potential for building blocks of materials. *Chemical Reviews*, 118(11):5755–5870, 2018. doi: 10.1021/acs.chemrev.7b00524.

[144] M. Cerón, F. Li, and L. Echegoyen. Endohedral fullerenes: The importance of electronic, size and shape complementarity between the carbon cages and the corresponding encapsulated clusters. *Journal of Physical Organic Chemistry*, 27, 2014. doi: 10.1002/poc.3245.

[145] J. Biskupek, S.T. Skowron, C.T. Stoppiello, G.A. Rance, S. Alom, K.L.Y. Fung, R.J. Whitby, M.H. Levitt, Q.M. Ramasse, U. Kaiser, E. Besley,

and A.N. Khlobystov. Bond dissociation and reactivity of hf and h2o in a nano test tube. *ACS Nano*, 14(9):11178–11189, 2020. doi: 10.1021/acsnano.0c02661.

[146] M. Waiblinger, K. Lips, W. Harneit, A. Weidinger, E. Dietel, and A. Hirsch. Corrected article: Thermal stability of the endohedral fullerenes n@c_{60}, n@c_{70}, and p@c_{60} [phys. rev. b 63, 045421 (2001)]. *Phys. Rev. B*, 64:159901, 2001. doi: 10.1103/PhysRevB.64.159901.

[147] B. Pietzak, M. Waiblinger, Theo Almeida Murphy, Alois Weidinger, M. Höhne, E. Dietel, and A. Hirsch. Buckminsterfullerene c_{60}: A chemical faraday cage for atomic nitrogen. *Chemical Physics Letters*, 279: 259–263, 1997. doi: 10.1016/S0009-2614(97)01100-7.

[148] P. Delaney and J. C. Greer. C_{60}as a faraday cage. *Applied Physics Letters*, 84(3):431–433, 2004. doi: 10.1063/1.1640783.

[149] S. Lo, A.V. Korol, and A.V. Solov'yov. Dynamical screening of an atom confined within a finite-width fullerene. *Journal of Physics B: Atomic, Molecular and Optical Physics*, 40(19):3973–3981, 2007. doi: 10.1088/0953-4075/40/19/014.

[150] G. Gao and H.S. Kang. C_{60} as a chemical faraday cage for three ferromagnetic fe atoms. *Chemical Physics Letters*, 462(1):72–74, 2008. doi: https://doi.org/10.1016/j.cplett.2008.07.044.

[151] A.V. Marenich, C.J. Cramer, and D.G. Truhlar. Reduced and quenched polarizabilities of interior atoms in molecules. *Chem. Sci.*, 4:2349–2356, 2013. doi: 10.1039/C3SC50242B.

[152] R.R. Zope, S. Bhusal, L. Basurto, T. Baruah, and K. Jackson. Site specific atomic polarizabilities in endohedral fullerenes and carbon onions. *The Journal of Chemical Physics*, 143(8):084306, 2015. doi: 10.1063/1.4928079.

[153] S.M. Avdoshenko. Fullerene faraday cage keeps magnetic properties of inner cluster pristine. *J Comput Chem*, 39(21):1594–1598, 2018. doi: 10.1002/jcc.25231.

[154] J.A. Luque-Urrutia, A. Poater, and M. Solà. Do carbon nano-onions behave as nanoscopic faraday cages? a comparison of the reactivity of c_{60}, c_{240}, c_{60}@c_{240}, li+@c_{60}, li+@c_{240}, and li+@c_{60}@c_{240}. *Chemistry – A European Journal*, 26(4):804–808, 2020. doi: https://doi.org/10.1002/chem.201904650.

[155] E.B. Lindgren, H. Chan, A.J. Stace, and E. Besley. Progress in the theory of electrostatic interactions between charged particles. *Phys. Chem. Chem. Phys.*, 18:5883–5895, 2016. doi: 10.1039/C5CP07709E.

[156] William I. F. David, Richard M. Ibberson, J.C. Matthewman, K. Prassides, T.J.S. Dennis, J.P. Hare, H.W. Kroto, R. Taylor, and D.R.M. Walton. Crystal structure and bonding of ordered c_{60}. *Nature*, 353(6340): 147–149, 1991. doi: 10.1038/353147a0.

[157] R. M. Fleming, B. Hessen, T. Siegrist, A. R. Kortan, P. Marsh, R. Tycko, G. Dabbagh, and R. C. Haddon. *Crystalline Fullerenes*, chapter 2, pages 25–39. doi: 10.1021/bk-1992-0481.ch002.

[158] P.A. Heiney, J.E. Fischer, A.R. McGhie, W.J. Romanow, A.M. Denenstein, J.P. McCauley Jr., A.B. Smith, and D.E. Cox. Orientational ordering transition in solid c_{60}. *Phys. Rev. Lett.*, 66:2911–2914, 1991. doi: 10.1103/PhysRevLett.66.2911.

[159] J. Tao, J. Yang, and A.M. Rappe. Dynamical screening of van der waals interactions in nanostructured solids: Sublimation of fullerenes. *The Journal of Chemical Physics*, 142(16):164302, 2015. doi: 10.1063/1.4918761.

[160] R. Garcia, C. Rey, and L. J. Gallego. Stability of binary clusters of fullerene molecules. *The Journal of Chemical Physics*, 108(22):9199–9201, 1998. doi: 10.1063/1.476373.

[161] G. J. Bubnis and H. R. Mayne. Structures of binary $c_{60}-c_{84}$ fullerene clusters. *The Journal of Physical Chemistry A*, 113(16):4598–4603, 2009. doi: 10.1021/jp811290h.

[162] D. Havlik, W. Schranz, M. Haluška, H. Kuzmany, and P. Rogl. Thermal expansion measurements of $c_{60}c_{70}$ mixed crystals. *Solid State Communications*, 104(12):775–779, 1997. doi: https://doi.org/10.1016/S0038-1098(97)00384-0.

[163] W. Sekkal, H. Aourag, and M. Certier. The miscibility of $c_{60}xc(70(1-x)$ alloy at high temperature. *Physics Letters A*, 251(2):132–136, 1999. doi: https://doi.org/10.1016/S0375-9601(98)00879-2.

[164] V.I. Zubov. Interactions between the molecules of different fullerenes. *Fullerenes, Nanotubes and Carbon Nanostructures*, 12(1-2):499–504, 2005. doi: 10.1081/FST-120027213.

[165] G. Raggi, A.J. Stace, and E. Bichoutskaia. Surface-charge distribution on a dielectric sphere due to an external point charge: examples of c_{60} and c_{240} fullerenes. *Phys. Chem. Chem. Phys.*, 15:20115–20119, 2013. doi: 10.1039/C3CP53522C.

[166] I.V. Lindell. Electrostatic image theory for the dielectric sphere. *Opt. Tecnol. Lett.*, (5):597–602, 1992. doi: doi:10.1029/91rs02255.

[167] W. Cai, S. Deng, and D. Jacobs. Extending the fast multipole method to charges inside or outside a dielectric sphere. *Journal of Computational Physics*, 223(2):846–864, 2007. doi: https://doi.org/10.1016/j.jcp.2006.10.019.

[168] A.A. Popov, S. Yang, and L. Dunsch. Endohedral fullerenes. *Chemical Reviews*, 113(8):5989–6113, 2013. doi: 10.1021/cr300297r. PMID: 23635015.

[169] L.S. Wang, J.M. Alford, Y. Chai, M. Diener, J. Zhang, S.M. McClure, T. Guo, G.E. Scuseria, and R.E. Smalley. The electronic structure of ca@c_{60}. *Chemical Physics Letters*, 207(4):354–359, 1993. doi: https://doi.org/10.1016/0009-2614(93)89013-8.

[170] D. S. Bethune, R. D. Johnson, J. R. Salem, M. S. de Vries, and C. S. Yannoni. Atoms in carbon cages: the structure and properties of endohedral fullerenes. *Nature*, 366(6451):123–128, 1993. doi: 10.1038/366123a0.

[171] T. He, G. Gao, L. Kou, G. Will, and A. Du. Endohedral metallofullerenes (m@c_{60}) as efficient catalysts for highly active hydrogen evolution reaction. *Journal of Catalysis*, 354:231–235, 2017. doi: 10.1016/j.jcat.2017.08.025.

[172] X. Chen, H. Zhang, and N. Lai. Endohedral metallofullerenes mn@c_{60} (m = mn, co, ni, cu; n = 2–5) as electrocatalysts for oxygen reduction reaction: a first-principles study. *Journal of Materials Science*, 55, 2020. doi: 10.1007/s10853-020-04864-4.

Appendix A

Theory

A.1 Formulation of the Problem

To account for the point-charge contribution to the surface free charge, the free charge σ_f is split into two contributions

$$\sigma_f = \sigma_s + \sigma_p. \tag{A.1}$$

Here σ_s corresponds to the square-integrable part of the surface charge, whereas σ_p is the point-charge contribution to the free charge represented by a linear combination of n_p Dirac delta distributions δ per particle:

$$\sigma_p = \sum_{i=1}^{M} \sum_{j=1}^{n_{p,i}} q_{i,j} \delta_{\mathbf{z}_{i,j}}, \text{ where } \mathbf{z}_{i,j} \in \Gamma_i \text{ and for all } j = 1, \ldots, n_{p,i}. \tag{A.2}$$

Next, we define an external potential Φ_{ext} with associated external electric field $\mathbf{E}_{\mathsf{ext}} := -\nabla\Phi_{\mathsf{ext}}$, and we do not impose the constraint that $\Phi_{\mathsf{ext}}(\mathbf{x}) \to 0$ as $|\mathbf{x}| \to \infty$. We consider the external potential to be harmonic, i.e. $\Delta\Phi_{\mathsf{ext}} = 0$, so that we do not describe the charges creating the external field within the considered system but we do not restrict the external electric field $\mathbf{E}_{\mathsf{ext}}$ to be uniform. Finally, we assume that the system of dielectric particles does not affect the external field $\mathbf{E}_{\mathsf{ext}}$, for instance, through polarisation, which justifies

the use of our terminology external.

Our aim is to now to determine the net surface charge on each dielectric particle after taking into account both the free charge σ_f as well as the bound charges resulting from polarisation effects due to the presence of charged neighbouring particles and the effect of the external electric field. Using the net surface charge, we will be able to deduce the other physical quantities of interest, namely, the electrostatic forces and energy resulting from the interaction of the M charged dielectric spheres both with each other and with the external electric field.

In order to determine the net surface charge, we will first derive governing equations for the net electrostatic potential. As we shall see, the net electrostatic potential can be used to deduce the required net surface charge as well as the subsequent physical quantities of interest. The main challenges in achieving our aim are to work with the singular nature of the point-charges σ_p and the external potential Φ_{ext} which does not necessarily decay to zero at infinity.

A.1.1 Formulation of the many-body problem based on a partial differential equation (PDE)

The problem of electrostatic interaction between M charged dielectric spheres can be described by a PDE-based transmission problem. Here, we define the total potential $\Phi_{\mathsf{tot}} = \Phi_{\mathsf{ext}} + \Phi$ and the corresponding total electric field $\mathbf{E}_{\mathsf{tot}} := \mathbf{E}_{\mathsf{ext}} + \mathbf{E}$, where $\mathbf{E}$ is the perturbation of $\mathbf{E}_{\mathsf{ext}}$ due to the presence of the dielectric charged spheres, and Φ is the corresponding perturbation potential so that $\mathbf{E} = -\nabla\Phi$. Standard arguments from the theory of electrostatics in dielectric media imply that the total potential Φ_{tot} satisfies the following conditions:

$$\Delta\Phi_{\mathsf{tot}} = 0 \qquad \text{in each } \Omega_i, \tag{A.3}$$

$$\Phi_{\mathsf{tot}} = 0 \qquad \text{on } \Gamma_0, \tag{A.4}$$

$$k\nabla\Phi_{\mathsf{tot}} = \sigma_f \qquad \text{on } \Gamma_0. \tag{A.5}$$

Here, Ω^+ denotes the space outside the particles, k is the dielectric function which takes value k_i on the ball $\overline{\Omega}_i$ and value k_0 on Ω^+, and Φ_{tot} and $k\nabla\Phi_{\mathsf{tot}}$ are jump discontinuities defined by

$$\Phi_{\mathsf{tot}}|_{\Gamma_i}(\mathbf{z}) := \Phi_{\mathsf{tot}}(\mathbf{z})|_{\Omega_i}\eta(\mathbf{z}) - \Phi_{\mathsf{tot}}(\mathbf{z})|_{\Omega^+}\eta(\mathbf{z}), \tag{A.6}$$

$$k\nabla\Phi_{\mathsf{tot}}|_{\Omega_i}(\mathbf{z}) := k_i\nabla\Phi_{\mathsf{tot}}(\mathbf{z})|_{\Omega_i}\cdot\eta(\mathbf{z}) - k_0\nabla\Phi_{\mathsf{tot}}(\mathbf{z})|_{\Omega^+}\cdot\eta(\mathbf{z}), \tag{A.7}$$

where $\eta(\mathbf{z})$ is the normal unit vector at $\mathbf{z} \in \Gamma_0$ pointing towards the exterior of the particles.

In general, Equations (A.3)-(A.5) are ill-posed as can be seen, for instance, by observing that if $\sigma_f \equiv 0$, then any constant function Φ_{tot} will satisfy this equation. In order to obtain the correct total potential Φ_{tot}, we make use of the relation $\Phi_{\mathsf{tot}} = \Phi_{\mathsf{ext}} + \Phi$ and first derive a well-posed equation for the electrostatic potential Φ. Using decomposition (A.1), elementary algebra yields Φ that satisfies the following transmission problem

$$\Delta\Phi = 0 \qquad \text{in each } \Omega_i, \tag{A.8}$$

$$\Phi = 0 \qquad \text{on } \Gamma_0, \tag{A.9}$$

$$k\nabla\Phi = \sigma_s + \sigma_p - (k - k_0)\partial_n\Phi_{\mathsf{ext}} \qquad \text{on } \Gamma_0, \tag{A.10}$$

$$|\Phi| \to 0 \qquad \text{as } |\mathbf{x}| \to \infty, \tag{A.11}$$

where $\partial_n\Phi_{\mathsf{ext}}$ denotes the normal derivative of Φ_{ext} on the boundary Γ_0. PDEs similar to the transmission problem (A.8)-(A.11) have been previously con-

sidered in the literature (see, e.g., [34, 37]), however the key novelty of Equations (A.8)-(A.11) is in the addition of contributions due to the external electric field and the presence of point-charges on the surface of the dielectric particles. These additional terms require a significant modification of the earlier definitions [37] of the electrostatic forces and interaction energy for the M-body charged dielectric spheres, and they present additional challenges in the efficient numerical implementation.

In addition to the presence of the highly non-regular point-charge term σ_p, another difficulty in solving the transmission problem (A.8)-(A.11) is the fact that the equation is posed on the entire space $\mathbb{R}^3$. Indeed, since the potential Φ a priori decays only as $|\mathbf{x}|^{-1}$, a naive truncation of the computational domain in an effort to use classical algorithms such as the finite element method leads to significant errors. The usual approach to circumventing this problem is to appeal to the theory of integral equations and reformulate the transmission problem (A.8)-(A.11) as a so-called boundary integral equation (BIE) posed on the interface Γ_0. This is the subject of the next subsection.

A.1.2 Based on an integral equation

In order to describe the integral equation-based approach to the problem of electrostatic interaction between M charged dielectric spheres we require some additional notions. First, we define the single layer potential of σ, denoted $\mathcal{S}\sigma$, as the mapping with the property that

$$(\mathcal{S}\sigma)(\mathbf{x}) := \int_{\Gamma} \frac{\sigma(\mathbf{y})}{4\pi|\mathbf{x}-\mathbf{y}|}\, d\mathbf{y}, \qquad \forall\, \mathbf{x} \in \Omega_0 \wedge \mathbf{x} \neq \mathbf{y}, \tag{A.12}$$

which also satisfies the following conditions

$$\mathcal{S}\sigma = 0; \qquad \nabla\mathcal{S}\sigma = \sigma.$$

As a consequence, it is possible to consider the restriction of the single layer potential defined through Equation (A.12) on the boundary Γ and thereby define the so-called single layer boundary operator, denoted $\mathcal{V}$ as the improper integral

$$(\mathcal{V}\sigma)(\mathbf{z}) := \int_{\Gamma} \frac{\sigma(\mathbf{z}')}{4\pi|\mathbf{z}-\mathbf{z}'|}\, d\mathbf{z}', \qquad \forall\, \mathbf{z} \in \Gamma_0 \wedge \mathbf{z} \neq \mathbf{z}'.$$

Note, that occasionally it will be necessary to consider the "local" single layer potential and boundary operators defined on an individual sphere Ω_i. We will denote these as $\mathcal{S}_i$ and $\mathcal{V}_i$ respectively.

The surface electrostatic potential λ is now described by the following boundary integral equation:

$$\lambda - \mathcal{V}\left(\frac{k_0 - k}{k_0}\mathrm{DtN}\lambda\right) = \frac{1}{k_0}\mathcal{V}(\sigma_s + \sigma_p) + \frac{k_0 - k}{k_0}\mathcal{V}(\partial_n \Phi_{\mathsf{ext}}). \tag{A.13}$$

Here, the notation DtN is used to denote the local Dirichlet-to-Neumann (DtN) map on the surface Γ (see Appendix A.1.1 for further details).

An equivalent reformulation of the BIE (A.13) for the induced surface charge can be achieved by applying $\mathcal{V}^{-1}$ to both sides of the equation, and defining $\sigma := \mathcal{V}^{-1}\lambda$ which yields the following BIE

$$\sigma - \frac{k_0 - k}{k_0}\mathrm{DtN}\mathcal{V}\sigma = \frac{1}{k_0}(\sigma_s + \sigma_p) + \frac{k_0 - k}{k_0}(\partial_n \Phi_{\mathsf{ext}}). \tag{A.14}$$

In Equation (A.14), the quantity of interest σ, which we often call the induced surface charge, represents (up to a scaling factor) the total surface charge on each dielectric particle after taking into account both the free charge σ_f as well as the bound charges resulting from polarisation effects due to the presence of charged neighbouring particles and the effect of the external electric field.

More precisely,

- σ_f represents the free charge on each particle;
- $\sigma_b := (k_0 - k)(\mathrm{DtN}\mathcal{V}\sigma + \partial_n \Phi_{\mathsf{ext}})$ represents the bound charge on each particle;
- $k_0\sigma = \sigma_f + \sigma_b$ represents the total charge on each particle.

A simple manipulation of Equation (A.14) yields the following relation between the surface charge σ and the surface electrostatic potential λ:

$$\sigma = \frac{k_0 - k}{k_0}\mathrm{DtN}\lambda + \frac{1}{k_0}(\sigma_s + \sigma_p) + \frac{k_0 - k}{k_0}(\partial_n \Phi_{\mathsf{ext}}). \tag{A.15}$$

Equation (A.15) implies that once λ is known, the charge distribution σ can be computed using the purely local DtN map.

We also remark here that the relation between the PDE (A.8)-(A.11) and the BIE (A.13) representations of the electrostatic potential can be clearly established since λ is simply the restriction (more precisely the Dirichlet trace) of the electrostatic potential Φ on the boundary Γ. Thus, for any point $\mathbf{x} \in \Omega$, we have $\Phi(\mathbf{x}) = (\mathcal{S}\mathcal{V}^{-1}\lambda)(\mathbf{x}) = (\mathcal{S}\sigma)(\mathbf{x})$, and we therefore also have $\Phi_{\mathsf{tot}}(\mathbf{x}) = \Phi_{\mathsf{ext}}(\mathbf{x}) + (\mathcal{S}\sigma)(\mathbf{x})$.

As emphasised above, an important technical difficulty in the analysis of Equation (A.13) is the presence of the low-regularity point-charge term σ_p, which requires special treatment in the design of efficient numerical methods. Previously, the BIE (A.13) has been the subject of extensive analysis in the much simpler case when both point-charges and the external field are absent, i.e., when $\sigma_p \equiv 0$ and $\Phi_{\mathsf{ext}} \equiv 0$. We first briefly summarise the existing methodology and explain how the BIE (A.13) can be solved in this simple case before turning attention to the more complex problem of describing surface point-charges and an external electric field.